

Sondre Bryn Høgheim

# Numerical Simulations and Operational Assessment of Installation of Anchors for Floating Wind turbines

Master's thesis in Marine Subsea Technology

Supervisor: Kjell Larsen

June 2020

**NTNU**  
Norwegian University of Science and Technology  
Faculty of Engineering  
Department of Marine Technology



# Numerical Simulations and Operational Assessment of Installation of Anchors for Floating Wind Turbines

Sondre Bryn Høgheim

June 10, 2020



## MASTER THESIS SPRING 2020

for

**Stud. tech. Sondre Bryn Høgheim**

### **Numerical Simulations and Operational Assessment of Installation of Anchors for Floating Wind Turbines**

*Numeriske beregninger og operabilitetsvurderinger av installasjon av anker for flytende vindturbiner*

#### Background

In order to be able to design, install and operate floating wind turbines and, in the future, large floating wind parks, cost-effective and safe marine operations are crucial. Capital expenditure of the marine operations for a floating wind park is large part of the total investment cost. An important building block for a floating wind turbine is the mooring system and installation of the anchors.

A key activity to successful subsea installation operations is the planning process. Lifting of subsea equipment, especially through the wave zone, is a weather critical activity. It is crucial that such operations are planned and understood properly and that effective equipment is used. This thesis shall specifically consider installation of anchor concepts for the, mooring system of floating wind turbines. Numerical simulations are an important part of the decision basis. The thesis shall use the tools available in the SIMA/SIMO program suite.

The main challenge of installation of the mooring system is the crane operation of the anchors. The state-of-art concept is the suction anchor. An alternative anchor concept is the Deep Penetrating Anchor (DPA) or the “torpedo” anchor. The thesis shall have a special focus on comparison of these anchor types.

#### Scope of Work

- 1) Review relevant literature and describe the main steps in the planning process of a marine operation in general. Describe briefly state-of-art subsea installation methods by use of crane vessels. For weather restricted operations, an overview of the planning process shall be described; the “alpha factor”-concept and how operability and weather windows can be optimized shall be described in detail.
- 2) Describe possible mooring systems for floating wind turbines. Focus on station keeping principles and main anchor concepts. Include an overview of the different anchor concepts available for the industry. A special comparison shall be given for the suction anchor and the torpedo anchor concepts.
- 3) Familiarize with the numerical simulation suite SIMA/SIMO and describe the theory that is relevant for subsea lifting and installation of anchors.
- 4) Review and improve numerical simulation models in SIMA for a suction anchor and a torpedo anchor. In particular, describe how important parameters like added mass, drag forces

and slamming forces are defined in the simulation models. Propose parameters that may determine the design operational limit and estimate limits based on simulation results. The variability of the design responses shall be assessed. Information on anchor concepts and simulation cases to be defined and discussed together with the supervisor.

5) Operability investigation. Based on simulation results from task 4) and weather data for specific locations, typical operability figures shall be calculated. Use the data and available tools. Consider to use Ocean4cast.com. Cases to be discussed and agreed with supervisor.

6) Conclusions and recommendations for further work.

#### General information

The work scope may change or prove to be larger than initially anticipated. Subject to approval from the supervisor, topics may be changed or reduced in extent.

In the project the candidate shall present his personal contribution to the resolution of problems within the scope of work.

Theories and conclusions should be based on mathematical derivations and/or logic reasoning identifying the various steps in the deduction.

The candidates should utilise the existing possibilities for obtaining relevant literature.

#### Report/Delivery

The thesis report should be organised in a rational manner to give a clear exposition of results, assessments, and conclusions. The text should be brief and to the point, with a clear language. Telegraphic language should be avoided.

The report shall be written in English and edited as a research report including literature survey, description of relevant mathematical models together with numerical simulation results, discussion, conclusions and proposal for further work. List of symbols and acronyms, references and (optional) appendices shall also be included. All figures, tables and equations shall be numerated.

The original contribution of the candidate and material taken from other sources shall be clearly defined. Work from other sources shall be properly referenced using an acknowledged referencing system.

The report shall be submitted in Inspira, as specified by the department of Marine Technology. In addition, an electronic copy (pdf) to be sent to the supervisor.

#### Ownership

NTNU has according to the present rules the ownership of the project results. Any use of the project results has to be approved by NTNU (or external partner when this applies). The department has the right to use the results as if the work was carried out by a NTNU employee, if nothing else has been agreed in advance.

#### Thesis supervisor:

Prof. II Kjell Larsen, NTNU/Equinor

**Deadline: June 10th, 2020**      Trondheim, January 20th, 2020

Kjell Larsen (sign.)

Sondre Bryn Høgheim (sign.)



# Preface

This Master Thesis represents the final part of my Master of Science degree in Marine Subsea Engineering at the department of Marine Technology (IMT) at the Norwegian University of Science and Technology (NTNU).

The main topic of this thesis is subsea lifting operations. Numerical models of a suction anchor and a deep penetrating anchor crane operation is created in the establishment of operational limits. The simulations is performed using the simulation software SIMA developed by SINTEF Ocean. Statistical data from Ocean4cast is used in the operability assessment based on forecast data from the Tampen area in the North Sea.

The work is done in the spring of 2020 under guidance from supervisor Professor II Kjell Larsen in Trondheim, Norway. The workload corresponds to 30 ECTS.

Trondheim, June 10, 2020

*Sondre Bryn Høgheim*  
Sondre Bryn Høgheim





# Acknowledgement

I Would like to thank my supervisor Professor II Kjell Larsen. His expertise in subsea lifting operations and hydrodynamics has been very useful in the understanding of important issues. His enthusiasm during our weekly guidance hour has kept me motivated throughout the process of writing this thesis.

I would like to thank Frøydis Solaas for being very helpful with the numerical modelling in SIMA, and being responsive in our e mail correspondence throughout the Corona pandemic. Frøydis' knowledge in lifting operations has proven to be essential in the implementation of hydrodynamic coefficients in the suction anchor model.

I would also like to thank Geir Jørdre for providing information about suction anchor installations, and being available for any questions throughout my final year at NTNU.



# Abstract

One of the main challenges related to the mooring system of floating wind turbines is the installation of anchors and the associated crane operation. Two different anchors that can be used for the mooring system is the traditional suction anchor (SA) and the deep penetrating anchor (DPA). This thesis's main objective is to find and compare the operational limit for the crane operation that is needed for the anchor installation.

Waiting on weather during the marine operations should be minimized to reduce costs, making it an essential part of the planning phase. The lifting operation involving the anchors is a weather crucial operation that should be planned concerning weather windows and safe conditions. The lift consists of phases with different duration where the lift through the splash zone may be the most critical. The operational design limit may be decided due to limitations in equipment, or safe working conditions on deck. The alpha factor is used to consider uncertainties in the weather forecast, thus reducing the operational criterion.

The suction anchor is a steel cylinder closed at the top and open at the bottom, which results in high tension when lower through the splash zone. The DPA is a solid torpedo shaped steel construction that is less exposed to direct wave excitation forces. The DPA is lowered to a distance above the seabed before its dropped. The high velocity of the anchor mass results in the kinetic energy needed for seabed penetration. The operability of the two different anchors was investigated by creating two numerical models and locating operational limits based on crane wire tension.

SINTEF Ocean's non-linear time-domain simulation program SIMA was used for modeling the lifts through the splash zone. A model was given by supervisor containing a crane vessel and an environment described by a JONSWAP spectrum. The lifting system consisted of a crane tip, crane wire, crane hook, slings, and a winch. The SA model was modeled with three slender elements, where each element is used in the modeling of depth-dependent hydrodynamic parameters. The DPA model was modeled with two slender elements. The hydrodynamic properties of the anchor models were partly implemented from experimental results and manually estimated.

The wave conditions for the simulations were based on hindcast data from the Tampen area in the North Sea. A text file containing weather data from 1957-2019 was given by the supervisor and used to find the P5, mean and P95 probabilities for the determination of peak period per simulated significant wave height  $H_s$ . Current and wind forces were not implemented in the condition sets.

The simulations were run with the P5, mean, and P95 peak period from each  $H_s$  and five seeds each (15 seeds per  $H_s$ ). The seed number was determined from the seed convergence test with the  $\mu$  parameter (MPM) from the Gumbel distribution. The best vessel heading relative to the waves during the lifting operation with the SA model was unknown. Therefore, the SA model was simulated for vessel heading 180°, 160°, and 135° to compare the results from crane wire tension.

Extreme values from maximum and minimum crane wire tension were gathered and plotted using the Gumbel distribution. The maximum and minimum tension limits were decided by the crane wire design strength and the slack criterion, respectively. The maximum tension for a  $H_s$  was determined from the 90% fractile of the extreme maxima, and the minimum tension from the 10% fractile of the extreme minima. Neither of the 10% fractiles of the extreme minima tensions from the SA and DPA simulations violated the slack criterion. The highest operational criterion  $H_{SWF}$  for the SA was found from the 160° wave direction at 3.1m. The operational limit for the DPA could not be based on crane wire tension as neither of the tension criteria was violated. The  $H_{SWF}$  for the DPA was estimated to 3.74m based on assumptions of safe working conditions on deck.

$H_{SWF}$  were estimated using the alpha factor for a level B marine operation. The planned operation period was assumed to be 6 hours for both anchors, resulting in a reference period of 9 hours.

The assessment of operability and waiting on weather (WoW) was done using Ocean4cast. The operation reference period and design criterion in terms of  $H_s$  were used by the Ocean4cast algorithm to calculate probabilities of operation duration at the Tampen area. The algorithm calculated the probability of duration for each month during a year based on hindcast data from 1957-2019.

It was found that if the lifting operations are performed during the summer months, the SA operation can be performed with a 90% probability from June to August. The DPA can be installed in May with the same probability. The DPA operation offers less WoW throughout the year, especially during the spring and autumn.

# Samandrag

Ei av dei største utfordringane til forankringssystemet for flytande vindturbinar er installasjonen av ankera og den tilhøyrande kran-operasjonen. To forskjellige anker-konsept som kan brukast i forankringssystemet er det tradisjonelle sugeankeret (SA) og *deep penetrating anchor* (DPA). Hovedmålet med denne oppgåva er å finne og samanlikne operasjonsgrenser for kran-operasjonen til havs, som er nødvendig for anker-installasjonen for forankringssystemet.

Venting på vêr under den marine operasjonen bør minimerast for å redusere kostnadane og er dermed ein viktig del av planleggingsfasen. Løfteoperasjonen som involverer ankeret, er avhengig av bra vêr og bør planleggast med hensyn til tilgjengelege vêrvindu og sikkerheit. Løftet består av fasar med ulik varigheit, løftet i gjennom plaskesonen kan være den mest kritiske. Operasjonsgrenser kan bestemmast ut i frå begrensningar i utstyr, eller trygge arbeidsforhold på dekk. Alfafaktoren brukast til å vurdere usikkerheiter i vêrmeldinga og reduserer dermed operasjonsgrenser kvar bølgehøgde eller vindhastighet blir brukt.

Sugeankeret er ein stålsylinder som er lukka i toppen og open i botn, noko som resulterer i store krefter når ein senker ankeret i gjennom plaskesona. DPA er ein solid torpedoforma stålkonstruksjon som er mindre utsatt for bølgekrefter, og blir senka ned til ein distanse over havbotn, kvar den blir sluppen. Farten ankeret får i fritt fall gjev høg kinetisk energi, som resulterer i at ankeret penetrerar seg djupt inn i havbotn.

SINTEF Ocean's ikkje-lineære simuleringsprogram SIMA, blei brukt til å modellere løfta gjennom plaskesona. Ein modell blei gjeven av rettleiar, som inneheldt eit kranfartøy og eit sjø-miljø beskrive av eit JONSWAP-spekter. Løftesystemet bestod av ein krantopp, krane-vaier, krane-blokk, slings og ein vinsj. SA-modellen blei modellert med tre slanke-element (slender elements), der kvart element brukast i modelleringa av dybde-avhengige hydrodynamiske eigenskapar. DPA-modellen blei modellert med to slanke-element. Dei hydrodynamiske eigenskapane til modellane blei delvis implementert frå eksperimentelle forsøk og manuelle estimat. Eigen-perioden på krane-vaier blei undersøkt for å validere modellane og for å identifisere risiko for resonans under løfta.

Bølgefôrholda for simuleringane var basert på data frå Tampen-området i Nordsjøen.

Ei tekstfil som inneheld vêrdata frå 1957-2019 blei gjeven av rettleiar og brukt til å finne P5, middel og P95-sannsyn for å bestemme topperioden (peak period) per simulerte signifikante bølgehøgde  $H_s$ . Straum og vindkrefter blei ikkje implementert i simuleringane. Simuleringane blei kjørt med topperiode P5, middel og P95 for kvar simulerte  $H_s$  med fem frø kvar (15 frø per  $H_s$ ). Frønummeret blei bestemt frå konvergenstest av MPM-parameter frå Gumbel-distribusjonen. Den beste fartøy-retninga relativt til bølgjene under løfteoperasjonen med SA var ukjent. Derfor blei SA-modellen simulert med 180°, 160° og 135° fartøys-retning. Dette var for å samanlikne krefter i krane-vaier under operasjonen.

Ekstremverdiar frå maksimal- og minimal kraft i krane-vaier blei henta og plotta ved bruk av Gumbel-fordelinga. Dei maksimale og minimale strekk-grensene blei bestemt av henholdsvis krane-vaier designstyrke og slakk-kriterie. Maksimal spenning for ein  $H_s$  blei bestemt frå 90%-fraktilen til ekstrem-maksimum strekk, og minimum strekk blei bestemt frå 10%-fraktilen til ekstrem-minimum strekk. Ingen av 10%-fraktilane til dei ekstrem-minimum strekkene frå SA- og DPA-simuleringane, braut med slakk-kriteriet. Det høgste operasjons-kriterie for SA blei funnet frå 160°- fartøysretning på 3.1m. Operasjonsgrensa for DPA kunne ikkje baserast på strekk i kranevaier, sidan ingen av spenningskriteriene blei forbigått. Operasjonsgrensa for DPA blei estimert til 3.74m basert på antagelsar om trygge arbeidsforhold på dekk.

Operasjonsgrensene blei estimert ved å bruke alfafaktoren for ein level B marin operasjon. Den planlagde operasjons-perioden blei anteke til 6 timar for begge ankera. Noko som resulterte i ein referanseperiode på 9 timar.

Vurderinga av operabilitet og venting på vêr blei gjort ved bruk av Ocean4cast. Referanseperioden på operasjonen, og operasjonsgrenser i form av  $H_s$  blei brukt av Ocean4cast-algoritmen for å rekne ut sannsynet for operasjons-varigheit på Tampen-området. Algoritmen rekna ut sannsynet for varigheit for kvar månad i løpet av eit år basert på hindcast-data frå 1957-2019.

Det vart funne at om løfteoperasjonen vert utført i løpet av sumar-månadane, kan sug-eankeroperasjonen utførast med ein 90% sannsyn frå juni til august. DPA-ankeret kan installerast i mai med same sannsyn. DPA-operasjonen byr på mindre venting på vêr i løpet av året, spesielt om våren og hausten.

# Contents

<b>1</b>	<b>Introduction</b>	<b>1</b>
1.1	Background	1
1.2	Objectives	2
1.3	Thesis Outline	2
<b>2</b>	<b>Marine operations</b>	<b>5</b>
2.1	Weather Restricted Marine Operations	5
2.1.1	Alpha factor	7
2.1.2	Weather Windows	7
2.2	The Planning Process	9
<b>3</b>	<b>Mooring Systems</b>	<b>11</b>
3.1	Catenary System	12
3.2	Taut Leg System	12
3.3	Anchor concepts	13
3.3.1	Suction Anchor	13
3.3.2	Fluke Anchors	14
3.3.3	Deep Penetrating Anchors	15
3.3.4	Driven Pile Anchor	16
3.4	Mooring of Floating Wind Turbines	16
<b>4</b>	<b>Subsea Lifting and Installation</b>	<b>19</b>
4.1	Lifting Methods	20
4.1.1	Moonpool	20
4.1.2	Special Handling System	20
4.1.3	Over-the-side	21
4.2	Suction Anchor Installation	21
4.2.1	Phase 1: Lift-off	21
4.2.2	Phase 2: Object in Air	22
4.2.3	Phase 3: Object Crossing Splash Zone	23
4.2.4	Phase 4: Object submerged	24
4.2.5	Phase 5 and 6: Anchor Landing and Installation	25
4.3	Deep Penetrating Anchor Installation	27
<b>5</b>	<b>Hydrodynamics</b>	<b>31</b>
5.1	Linear Wave Theory	31

5.2	Irregular waves . . . . .	32
5.2.1	Wave Spectra . . . . .	32
5.2.2	Seed Waves . . . . .	35
5.3	Time Domain Analysis . . . . .	35
5.3.1	The Equation of Motion . . . . .	35
5.3.2	Static and Dynamic Equilibrium . . . . .	36
5.4	Hydrodynamic Forces . . . . .	38
5.4.1	Inertia Force . . . . .	38
5.4.2	Drag Force . . . . .	39
5.4.3	Slamming Force . . . . .	39
5.4.4	Buoyancy Force . . . . .	40
5.5	Crane Tip Motion . . . . .	40
5.6	Hydrodynamic Parameters . . . . .	41
5.6.1	Drag Coefficient . . . . .	41
5.6.2	Added Mass . . . . .	42
<b>6</b>	<b>Statistical Approach . . . . .</b>	<b>45</b>
6.1	Gumbel Extreme Value Distribution . . . . .	47
6.1.1	Probability Density Function . . . . .	47
6.1.2	Cumulative Distribution Function . . . . .	49
6.1.3	Gumbel Plot . . . . .	50
6.2	Exceedance Probabilities . . . . .	51
6.2.1	Design Criteria Based on Crane Wire Tension . . . . .	52
6.3	Weibull Distribution . . . . .	53
<b>7</b>	<b>Simulation Software . . . . .</b>	<b>55</b>
7.1	Time Domain Analysis . . . . .	56
7.2	Distributed element force . . . . .	56
7.3	Post processor application . . . . .	58
<b>8</b>	<b>The Simulation Model . . . . .</b>	<b>59</b>
8.1	Installation Vessel . . . . .	59
8.1.1	First Order Motion Transfer Functions . . . . .	61
8.2	Lifting Equipment . . . . .	63
8.2.1	Hook . . . . .	64
8.2.2	Crane wire and slings . . . . .	65
8.3	Suction Anchor Model . . . . .	66
8.3.1	Anchor top element . . . . .	67
8.3.2	Anchor Wall element . . . . .	68
8.3.3	Entrapped water element . . . . .	69
8.3.4	Vertical added mass and damping . . . . .	69
8.3.5	Horizontal added mass and damping . . . . .	71
8.4	Deep Penetrating Anchor Model . . . . .	72
8.4.1	Shaft element . . . . .	73



8.4.2	Fluke element . . . . .	73
8.4.3	Vertical added mass and damping . . . . .	74
8.4.4	Horizontal added mass and damping . . . . .	74
8.5	Anchor Kinetics . . . . .	75
8.6	Static analysis . . . . .	75
<b>9</b>	<b>Simulation Properties . . . . .</b>	<b>77</b>
9.1	Environmental Conditions . . . . .	77
9.1.1	Wave Conditions . . . . .	77
9.2	Simulation length . . . . .	79
9.3	Eigen Period of Crane Wire . . . . .	80
9.3.1	Eigen Period Validation of Simulation Model . . . . .	81
9.4	Maximum and Minimum Allowable Tension . . . . .	84
9.5	Seed Number . . . . .	84
9.6	Simulation Properties . . . . .	86
<b>10</b>	<b>Simulation Results . . . . .</b>	<b>87</b>
10.1	Crane Tip Motion . . . . .	87
10.2	Suction Anchor . . . . .	89
10.2.1	Tension in Crane Wire . . . . .	90
10.3	Deep Penetrating Anchor . . . . .	94
10.4	Gumbel Distributions . . . . .	95
10.4.1	Extreme Minimum Distributions . . . . .	96
10.4.2	Extreme Maximum Distributions . . . . .	98
10.5	Design Criteria . . . . .	101
<b>11</b>	<b>Operability and Assessment of Waiting on Weather . . . . .</b>	<b>103</b>
11.1	Ocean4cast . . . . .	104
11.2	Operability investigation . . . . .	106
11.2.1	Duration of Operations . . . . .	107
<b>12</b>	<b>Conclusion . . . . .</b>	<b>113</b>
12.1	Source of Errors . . . . .	114
12.2	Recommendations for Further Work . . . . .	115
	<b>Bibliography . . . . .</b>	<b>115</b>
<b>A</b>	<b>Vessel First Order Motion Transfer Functions . . . . .</b>	<b>121</b>
<b>B</b>	<b>Statistics . . . . .</b>	<b>123</b>
B.1	DPA Characteristic values . . . . .	126
B.2	MATLAB plot . . . . .	126



# List of Figures

2.1	Relation between $T_R$ , $T_{POP}$ and $T_C$ (DNV-GL (2016a)). . . . .	8
2.2	Varying significant wave height with associated working and waiting times. (Larsen (2019b)). . . . .	9
2.3	Recommended planning and design sequence (DNV-GL (2011a)). . . . .	10
3.1	Catenary mooring system (ABC-Moorings (2019)). . . . .	12
3.2	Taut leg mooring system (ABC-Moorings (2019)). . . . .	12
3.3	Suction anchor (Hansen (2013)). . . . .	13
3.4	Pad eye on an embedded suction anchor (Bai and Jin (2016)). . . . .	14
3.5	Drag embedded vs. vertical load anchor. . . . .	15
3.6	Deep penetrating anchors (Deepsea anchors (2019)). . . . .	15
3.7	Wind farm network ( DOF (2019)). . . . .	17
4.1	Moonpool (Bourbon Offshore (2020)). . . . .	20
4.2	Vessel main crane (Hansen (2013)). . . . .	21
4.3	Lift of from Skandi Skansen (DOF (2019)). . . . .	22
4.4	DAF as found in standard (DNV-GL (2014)). $t$ is the weight in tons. . . . .	23
4.5	Suction anchor lowered by Skandi Skansen through splash zone (DOF (2019)). . . . .	23
4.6	Anchor lowered by Skandi Skansen (DOF (2019)). . . . .	24
4.7	Anchor landed and fastened (DOF (2019)). . . . .	26
4.8	DPA installed from the stern of vessel (Hove (2001)). . . . .	27
4.9	DPA hoisted through the splash zone. . . . .	28
4.10	Mooring rope landed on the seabed. Vessel carefully moves to intended drop location. . . . .	28
4.11	DPA installed. Mooring rope lays on sea bed ready to be picked up. . . . .	29
5.1	Time domain and frequency domain in same illustration (Faltinsen (1990)).	33
5.2	Pierson-Moskowitz and JONSWAP spectra (Faltinsen (1990)). . . . .	34
5.3	Parameters that determine the vertical forces in the hoisting wire. . . . .	38
5.4	Slamming force proportional with change of added mass . . . . .	40
5.5	Drag coefficients from DNV-GL (2011b). . . . .	42
5.6	Change of vertical added mass for suction anchor (T.Næss et al. (2014)). . . . .	43

5.7	Added mass coefficients ( $C_A$ ) (DNV-GL (2011b)). . . . .	44
5.8	Added mass coefficients ( $C_A$ ) from DNV-GL (2011b). . . . .	44
6.1	Increased sample size yields increased accuracy in the statistical distribution.	45
6.2	Definition of peaks (maximums) and extremes of the statistical sample (Larsen (2020)). . . . .	46
6.3	Gumbel PDF created from extreme maximum values from multiple meas- urements. . . . .	48
6.4	Gumbel PDF created from extreme minimum values from multiple meas- urements. . . . .	48
6.5	Example of Gumbel cumulative distribution function. . . . .	49
6.6	Example of inverse cumulative distribution function. . . . .	50
6.7	Example of Gumbel plot from a extreme maximum sample. . . . .	51
6.8	Definition of P90, P50 and P10 probabilities. . . . .	52
6.9	10% fractile of minima must be above the slack criteria and 90% fractile of maxima must be below wire design strength. . . . .	53
6.10	Weibull probability plot for sample of measured $H_s$ . . . . .	54
7.1	Local strip coordinate system (SINTEF Ocean (2019a)) . . . . .	56
7.2	Extreme value taken from time window interval. . . . .	58
8.1	Skandi Acergy (Skipsrevyen (2018)) . . . . .	59
8.2	Global coordinate system, vessel centre of gravity and crane tip location. .	60
8.3	Vessel degrees of freedom (Larsen (2019a)). . . . .	61
8.4	Wave direction definitions, vessel seen from above. . . . .	61
8.5	Heave RAO: blue=90° red=135° green=180°. . . . .	62
8.6	Roll RAO: blue=90° red=135° green=158°. . . . .	62
8.7	Pitch RAO: blue=135° red=158° green=180°. . . . .	63
8.8	Lifting equipment for suction anchor (left) and deep penetration anchor (right). . . . .	64
8.9	Hook body points in SIMA . . . . .	65
8.10	Sling angle and length for suction anchor rigging. . . . .	66
8.11	Suction anchor with highlighted slender elements. . . . .	67
8.12	Depth dependent added mass for suction anchors (T.Næss et al. (2014)). .	68
8.13	Suction anchor wall element with strips. . . . .	69
8.14	Experimental results by Sandvik and Solaas (2017). . . . .	70
8.15	Slender element coordinate system. . . . .	71
8.16	DPA model with two slender elements. . . . .	73
9.1	Hywind Tampen (61°15, 995'N°16, 117'E) . . . . .	77
9.2	$H_s$ and $T_p$ in the period 1957-2019 Tampen area. . . . .	78
9.3	Vertical particle motion as a function of water depth. . . . .	80
9.4	Vertical resonance period for SA and DPA. . . . .	81

9.5	SA in initial conditions with winch start and stop. . . . .	81
9.6	Wire tension spectrum for SA model in initial conditions. . . . .	82
9.7	DPA in initial conditions with winch start and stop. . . . .	83
9.8	Wire tension spectrum for DPA model in initial conditions. . . . .	83
9.9	Convergence test for $H_s=1m$ . . . . .	85
9.10	Convergence test for $H_s=2m$ . . . . .	85
10.1	Vertical crane tip motion with increasing $H_s$ . . . . .	87
10.2	$H_s=1m$ $T_p=8.4s$ . . . . .	88
10.3	$H_s=6m$ $T_p=12.3s$ . . . . .	88
10.4	Visualization of SIMA SA lowering. . . . .	89
10.5	Tension in crane wire compared to tension in slings. . . . .	90
10.6	Crane wire tension through splash zone and lowering, $H_s = 1m$ . . . . .	90
10.7	Crane wire tension through splash zone and lowering, $H_s = 4m$ . . . . .	91
10.8	Wire tension spectrum for SA model in splash zone. . . . .	92
10.9	Tension spectrum for SA model. Same $H_s$ with two different wave periods. . . . .	92
10.10	Total crane wire tension with $T_p$ 14.5s. . . . .	93
10.11	DPA model in SIMA. . . . .	94
10.12	$H_s = 4m$ , $T_p = 10.8s$ . . . . .	94
10.13	$H_s = 6m$ , $T_p = 12.3s$ . . . . .	95
10.14	Suction anchor extreme minimum distribution wave direction $180^\circ$ . . . . .	96
10.15	Suction anchor extreme minimum distribution wave direction $160^\circ$ . . . . .	96
10.16	Suction anchor extreme minimum distribution wave direction $135^\circ$ . . . . .	97
10.17	Deep penetrating anchor extreme minimum distribution . . . . .	97
10.18	Suction anchor extreme maximum distribution wave direction $180^\circ$ . . . . .	98
10.19	Suction anchor extreme maximum distribution wave direction $160^\circ$ . . . . .	99
10.20	Suction anchor extreme maximum distribution wave directions $135^\circ$ . . . . .	99
10.21	Gumbel plot with $H_s=1m$ and $H_s=4m$ . Extreme values for all three wave directions plotted. . . . .	100
10.22	DPA extreme maximum distributions. . . . .	101
11.1	Estimation of operation duration. Total duration at start $t_1$ and $t_2$ is 9 hours and 19 hours respectively. . . . .	105
11.2	$H_s$ as a function of time Tampen area 1957-2019. . . . .	106
11.3	Weibull PDF and CDF for $H_s$ Tampen 1957-2019. . . . .	107
11.4	Monthly duration SA $135^\circ$ $T_R=9$ hours, $H_{sWF}=2.53$ . . . . .	108
11.5	Monthly duration SA $180^\circ$ $T_R=9$ hours, $H_{sWF}=2.90m$ . . . . .	109
11.6	Monthly duration SA $160^\circ$ $T_R=9$ hours, $H_{sWF}=3.10m$ . . . . .	109
11.7	Monthly duration DPA $T_R=9$ hours, $H_{sWF}=3.74m$ . . . . .	110
11.8	$T_R$ for total SA installation compared to DPA. . . . .	111
11.9	Monthly probabilities of WoW for Total SA (purple) and DPA (yellow) installation. . . . .	112

A.1	Vessel Surge RAO. Green=180°, red=158°, blue=135°. . . . .	121
A.2	Vessel Sway RAO. Green=158°, red=135°, blue=90°. . . . .	122
A.3	Vessel Yaw RAO. Green=158°, red=135°, blue=90°. . . . .	122
B.1	Gumbel plot for all wave directions. . . . .	123
B.2	Gumbel plot for all wave directions. . . . .	124
B.3	Gumbel plot for all wave directions. . . . .	124
B.4	CDF for all $H_s$ and wave directions with P5 peak periods. . . . .	125
B.5	CDF for all $H_s$ and wave directions with P95 peak periods. . . . .	125
B.6	CDF for all $H_s$ and wave directions with mean peak periods. . . . .	126

# List of Tables

2.1	Weather forecast levels (DNV-GL (2011a)) . . . . .	6
2.2	Alpha factors for level B weather forecast level (DNV-GL (2011a)). . . . .	7
8.1	Skandi Acergy vessel data . . . . .	60
8.2	Mass coefficients for vessel in SIMA . . . . .	60
8.3	Mass coefficients for hook in SIMA. . . . .	64
8.4	Wire characteristics. . . . .	65
8.5	Suction Anchor properties. . . . .	67
8.6	Suction anchor top plate element (SE 1) properties. . . . .	68
8.7	Anchor wall element properties. . . . .	69
8.8	Vertical linear drag for suction anchor elements. . . . .	70
8.9	Vertical Added mass for suction anchor elements. . . . .	71
8.10	Horizontal added mass for suction anchor elements. . . . .	72
8.11	Horizontal quadratic drag for suction anchor model. . . . .	72
8.12	Shaft element properties. . . . .	73
8.13	Fluke element properties. . . . .	74
8.14	Vertical Added mass and quadratic drag for DPA. . . . .	74
8.15	Horizontal added mass and quadratic drag for DPA. . . . .	74
8.16	Mass and moment of inertia properties for SA and DPA. . . . .	75
8.17	Initial and static position for SA model. . . . .	75
8.18	Initial and static position for DPA model. . . . .	75
9.1	Condition sets used in Simulation. . . . .	79
9.2	Maximum and minimum allowable crane wire tension for SA and DPA. . . . .	84
9.3	Simulation characteristics. . . . .	86
9.4	Selected $H_s$ conditions for SA and DPA simulation. . . . .	86
10.1	Most probable maxima $\mu$ and 90% fractile P90 from extreme maxima distributions for all wave directions for suction anchor model. . . . .	100
10.2	Wave direction 180°. . . . .	102
10.3	Wave direction 160°. . . . .	102
10.4	Wave direction 135°. . . . .	102
10.5	Suction anchor design criteria interpolated from Table 10.1. . . . .	102

11.1	Phases together with total $T_{pop}$ for SA and DPA. . . . .	103
11.2	Design criterion $H_{SLIM}$ , alpha factor $\alpha$ and Operational criterion $H_{SWF}$ for the crane operations. . . . .	104
11.3	Probability that measured $H_s$ is lower than the operational criteria. . . . .	107
11.4	Seasons and respective months. . . . .	108
11.5	Duration of operation at Tampen. All duration's given in hours. $T_R = 9$ hours. . . . .	111
B.1	Most probable maxima and 90% fractile P90 from extreme maxima dis- tributions for all wave directions for crane wire tension DPA model. . . . .	126



# Abbreviations

AHV	Anchor handling vessel
CDF	Cumulative Distribution function
CMS	Catenary mooring system
DAF	Dynamic amplification factor
DEA	Drag embedded anchor
DHL	Dynamic hook load
DNV GL	Det Norske Veritas og Germanischer Loyd
DPA	Deep penetrating anchor
DP	Dynamic positioning
DWT	Dead weight tonnes
ISSC	International ship and offshore structures congress
ITTC	International towing tank conference
JONSWAP	Joint North Sea wave project
LOA	Vessel length over all
MPM	Most probable maxima/minima
MW	Mega watt
OCV	Offshore construction vessel
PDF	Probability density function
PM	Pierson-Moskowitz
RAO	Response amplitude operator
ROV	Remote operated vehicle
RPN	Risk priority number
SA	Suction Anchor
SCS	Safety critical system
SE	Slender element
SF	Safe condition
SHL	Static hook load
SHS	Special handling system
TLS	Tau leg mooring system
VLA	Vertical load anchor
WoW	Waiting on Weather



# Nomenclature

$\alpha$	Alpha Factor
$\beta$	Gumbel scale Parameter
$\gamma$	Peakedness Parameter JONSWAP
$\gamma$	Euler-Mascheroni constant
$\epsilon$	Random phase angle
$\zeta$	Wave Elevation
$\zeta_a$	Wave Amplitude
$\dot{\zeta}$	Vertical Wave Velocity
$\eta$	Vertical Object Motion
$\dot{\eta}$	Vertical Object Velocity
$\ddot{\eta}$	Vertical Object Acceleration
$\eta_{ct}$	Vertical Crane tip Motion
$\mu$	Gumbel location Parameter
$\tau_c$	Duration of Calms
$\phi$	Velocity Potential
$\omega$	Wave Frequency
$\omega_p$	Peak Frequency
$\rho$	Sea water density
$\omega$	Wave frequency
$\omega_0$	Natural frequency
$\omega_p$	Peak frequency
$A$	Added mass
$A_{33}$	Vertical Added mass
$A_m$	Moonpool area
$A_p$	Projected area
$A_w$	Waterplane area

$g$	Gravity acceleration
$C$	Damping coefficient
$C_A$	Added mass coefficient
$C_D$	Drag coefficient
$C_S$	Slamming coefficient
$D$	Anchor diameter
$D_m$	Moonpool diameter
$F_B$	Buoyancy force
$F_D$	Drag force
$F_I$	Inertia force
$F_S$	Slamming force
$H$	Anchor height
$H_s$	Significant wave height
$H_{SLIM}$	Significant wave height design criterion
$H_{SWF}$	Significant wave height operational criterion
$K$	Elastic stiffness hoisting wire
$K$	Stiffness coefficient
$k$	Wave number
$M$	Anchor mass
$m_w$	Hoisting wire weight per meter
$L$	Hoisting wire length
$OP_{LIM}$	Design criterion
$OP_{WF}$	Operational criterion
$T$	Wave period
$T_C$	Contingency time
$T_p$	Peak period
$T_{pop}$	Planned operation period
$T_R$	Reference period
$T_{tot}$	Time interval
$T_{op}$	Operational period
$T_0$	Moonpool Natural period
$T_\eta$	Resonance period
$V$	Volume
$V_r$	Reference volume
$v$	Fluid particle velocity
$\dot{v}$	Fluid particle acceleration

*if not specified otherwise*

# Chapter 1

## Introduction

### 1.1 Background

To realize large floating wind farm projects in the future, cost-effective and safe marine operations is crucial. Costs related to marine operations when installing the floating wind farm is a large part of the total economic investment. A floating wind farm will consist of multiple turbines and the installation of the mooring system and the anchors are a major part of the work.

Equinor is planning to install the world's biggest floating wind farm consisting of eleven turbines with a total capacity of 80-100MW (NRK (2020)). The area is located about 140 km from shore at 260-300 meters water depth. A typical mooring layout for a wind turbine is three lines equally spread down to the anchors. For the Tampen project, the eleven turbines will require 33 mooring lines and 19 anchors (Equinor (2019)). The installation of the 19 anchors may be challenging as the Tampen area is characterized by the harsh weather conditions that is found in the North Sea. Minimum waiting on weather for the installation vessel is desired to keep installation costs to a minimum. This thesis will use the Tampen area as the basis of the marine operations.

Minimum waiting on weather is closely related to the operation reference period and the  $H_s$  operational criterion for the crane operation. The Weather conditions are an external factor that is beyond the control of the engineer. However, smart and innovative solutions regarding the execution of the marine operations is the responsibility of the engineer. The engineers also have the responsibility of studying alternative approaches that may minimize costs and realize projects for the future. If the installation costs of a floating wind farm can be reduced by new innovative anchor concepts, offshore wind has a large potential not only in the North Sea but locations all over the world.

## 1.2 Objectives

The main objective of this thesis is to investigate the potential for improvement in the operability of installing the anchors for floating wind farms. This is done by a comparison of the crane operation with the traditional suction anchor with the deep penetrating anchor. The operability is decided by the operational limit in terms of significant wave height and operation reference period. The operability for the two different crane operations is assessed based on probabilities of expected operational duration.

## 1.3 Thesis Outline

Chapter 2 describes the definition of the marine operation and focus on the planning process. Weather restricted and weather unrestricted marine operations are described. The concept of the alpha factor is described, and how to estimate the operational criterion based on planned operational period and design criterion.

Chapter 3 covers different mooring systems that can be used for floating wind farms. Different anchor concepts are described.

Chapter 4 is giving an insight to different subsea lifting methods. The phases of the lift over-the-side with the suction anchor and DPA model is described in detail.

Chapter 5 is devoted to the hydrodynamic theory that is relevant for the lifting operation. Important parameters like added mass, Morison forces and slamming force is described in detail. How vertical crane tip motion is estimated based on heave, pitch and roll motion for the vessel center of gravity is also described.

Chapter 6 focus on relevant theory from statistical distributions. How the cumulative distribution function and the probability density function of the Gumbel distribution is found is described in detail. The design criterion based on extreme values from crane wire tension is also described.

Chapter 7 gives a brief description of the simulation software SIMA and how the post processor application is used to gather extreme values.

Chapter 8 describes the simulation models in detail. This involves the vessel, lifting equipment and anchors. How parameters like added mass and damping is implemented in for the two different anchor models is also described.

Chapter 9 covers the simulation properties. This includes environmental conditions, simulation length, eigen period of crane wire, and the determination of maximum and minimum allowable tension in the crane wire during the simulations.

Chapter 10 presents the simulation results. The crane tip motion with increased wave

height is presented. Examples of time series of the SA and DPA is plotted. The results from plotting the Gumbel distribution with extreme maximum and minimum tensions is shown.

Chapter 11 focus on the operability and assessment of waiting on weather for the two different crane operations.

Chapter 12 contain the conclusion, source of errors, and recommendations for further work.

Additional material such as vessel RAO's, statistical results, and a brief MATLAB-code is found in Appendix.





## Chapter 2

# Marine operations

Marine operations are operations specially designed to be performed in the marine environment. For safe execution, the operations are designed for limited duration and has predefined operational limits. The main goal of a properly planned marine operation is to minimize cost at an acceptable risk and operability level. The operation shall be designed to bring handled objects from one predetermined safe condition to another. A typical design criteria for marine operations is that the operation should have the ability to be stopped, and the object can be brought to a safe condition. Safe conditions are predefined in the planning process, representing a condition where the handled object is only exposed to average risk. Where "average risk" means the risk that the object would usually have when installed in its intended position (Larsen (2019b)).

Marine operations can be divided into *weather restricted* and *weather unrestricted* operations. The duration of the operation will decide which type it must be designed against. Some operations will need to be designed to withstand extreme weather. These are called weather unrestricted operations, and will be appropriate for operations that must be performed in areas or parts of the year where the weather must be assumed to be extreme (Larsen (2019b)). Here, the operational limits are determined from extreme statistical values, and the duration of the operation is usually over 72 hours (DNV-GL (2011b)). However, for a weather restricted operation, an assessment of the duration must be done in order to decide when to initiate the operation in terms of available weather windows.

### 2.1 Weather Restricted Marine Operations

An Operation with a duration under 72 hours, is usually designed as a weather restricted operation. Here, weather windows must be considered. A weather window is a duration of calm weather, long enough to contain the whole operation. A favorable weather forecast with a sufficient weather window, provides the opportunity to execute the operation

without designing it against statistical extreme values; hence the name weather restricted. Depending on the operational sensitivity to weather conditions and the reference period ( $T_R$ ), weather restricted operations is assigned a weather forecast level. Level A operations are primary marine operations that are very sensitive to weather conditions, e.g., towing or mating operations. Level B operations are also sensitive to environmental conditions in addition to being relevant concerning the consequence of failure. Level C operations refer to more basic operations where environmental conditions are of less importance and carried out regularly. Examples of level C operations are onshore lifting operations and tows in calm inshore waters (DNV-GL (2011a)). The level requirements can be seen in table 2.1.

**Table 2.1:** Weather forecast levels (DNV-GL (2011a))

Weather forecast levels			
Weather forecast Level	Meteorologist at site?	Independent WF sources	Maximum WF interval
A	Yes (1)	2 (2)	12 hours (3)
B	No (4)	2 (5)	12 hours
C	No	1	12 hours

(1) There should be a dedicated meteorologist, but it may be acceptable that he/she is not physically present at site. The meteorologist opinion regarding his preferable location should be duly considered. It is anyhow mandatory that the dedicated meteorologist has continuous access to weather information from the site and that he/she is familiar with any local phenomena that may influence the weather conditions.

(2) It is assumed that the dedicated meteorologist (and other involved key personnel) will consider weather information/forecasts from several (all available) sources.

(3) Based on sensitivity with regards to weather conditions smaller intervals may be required.

(4) Meteorologist shall be conferred if the weather situation is unstable and/or close to the defined limit.

(5) The most severe weather forecast to be used.

### 2.1.1 Alpha factor

The alpha factor is introduced to take into account uncertainties in the forecasting and monitoring of environmental conditions. The alpha factor is found in the standard (DNV-GL (2011a)) and multiplied with the design criterion  $OP_{LIM}$ , as shown in Equation 2.1. A specific marine operation will have an estimated duration called *planned operation period*  $T_{POP}$  and an operational limit, usually in the form of a significant wave height  $H_s$  or wind speed. Based on these parameters, an alpha factor  $\alpha$  can be found in the standard. In the north sea, the alpha factor is selected from the relevant table based on the weather forecast levels (Table 2.1). Using the alpha factor, we avoid unnecessary discussion at site between personnel, and set clear lines for when the operation can be started (Larsen (2019b)). In equation 2.1,  $OP_{LIM}$  usually is the significant wave height or the wind speed. By using the alpha factor, the operational limit becomes a conservative measure, and we get the operational criterion  $OP_{WF}$ .

$$OP_{WF} = \alpha \cdot OP_{LIM} \quad (2.1)$$

An offshore crane operation may be classified as a forecast level B operation. Table 2.2 shows the alpha factor for such an operation taken from *DNV-OS-H101: Marine Operations, General*, a standard that provides guidance to performing marine operations safely.

**Table 2.2:** Alpha factors for level B weather forecast level (DNV-GL (2011a)).

Alpha factor for waves, Level B operation							
Operational period [Hours]	Design wave [m]						
	Hs = 1	1 <Hs <2	Hs = 2	2 <Hs <4	Hs = 4	4 <Hs <6	Hs >6
Tpop <12	0.68	Linear	0.80	Linear	0.83	Linear	0.84
Tpop <24	0.66		0.77		0.80		0.82
Tpop <36	0.65		0.75		0.77		0.80
Tpop <48	0.63	interpolation	0.71	interpolation	0.75	interpolation	0.78
Tpop <72	0.58		0.66		0.71		0.76

### 2.1.2 Weather Windows

concerning environmental conditions. When it comes to marine operations, essential factors are the use of time and rapid change in weather conditions. The forecasted weather window must contain environmental conditions below the operational criterion so that the operation can be executed safely for all associated equipment and personnel.

The duration of the operation is referred to as the operation reference period  $T_R$ . This duration is given by the planned operation period  $T_{POP}$ , which is a carefully calculated estimate based on the scope of the operation, and the contingency time  $T_C$ . The contingency time is used for covering uncertainties in  $T_{POP}$  and should not be less than 6 hours. This can be time spent on unforeseen problems that may arise during the work

(DNV-GL (2016a)). These two periods are added together to give the reference period.

$$T_R = T_{POP} + T_C \quad (2.2)$$

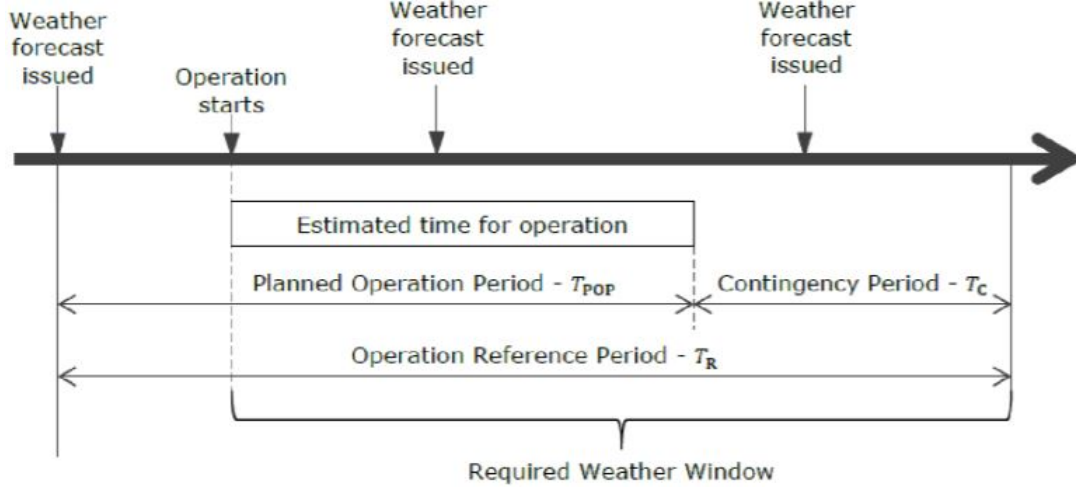


**Figure 2.1:** Relation between  $T_R$ ,  $T_{POP}$  and  $T_C$  (DNV-GL (2016a)).

When the reference period is found, it is easier to picture the scope of the operation, and we know the time we need to design the operation against. Weather windows should be conservatively assessed based on worst-case scenarios (DNV-GL (2011a)).

Ways have been developed to calculate the probability that the operation can be executed. During a year, the summer period is May to September in the northern hemisphere. During this period, we have the calmest weather, which is the desired period to perform marine operations in the north sea. For the operations to be performed, we need that the duration of calms  $\tau_C$  has to be higher than  $T_R$ . If we assume that  $H_s$  is the governing parameter and statistical data of this parameter exist, we need that  $H_s$  is lower than the operational criterion within the calms. The probability that  $H_s$  is lower than the operational criterion and at the same time, the duration of calms is longer than the reference period is given by equation 2.3 (Larsen (2019c)).

$$P_{work} = P[(\tau_C \geq T_R) \cap (H_s \leq OP_{WF})] \quad (2.3)$$

We can calculate the total operational period ( $T_{op}$ ) in a given time interval ( $T_{tot}$ ). This is done by multiplying the time interval with the probability of safe execution (Equation 2.4).  $T_{tot}$  is a time interval e.g. during the summer months. This will give an impression of how much *waiting on weather* one must expect during this period based on a statistical approach. For financial reasons, it is desirable to keep waiting on weather to a minimum. Figure 2.2 shows how marine operations can be divided by weather conditions. Here,

the operational criterion is defined by the significant wave height  $H_s$ , and work can only be performed when  $H_s$  is below this (Larsen (2019b)).

$$T_{op} = T_{tot} \cdot P_{work} \quad (2.4)$$

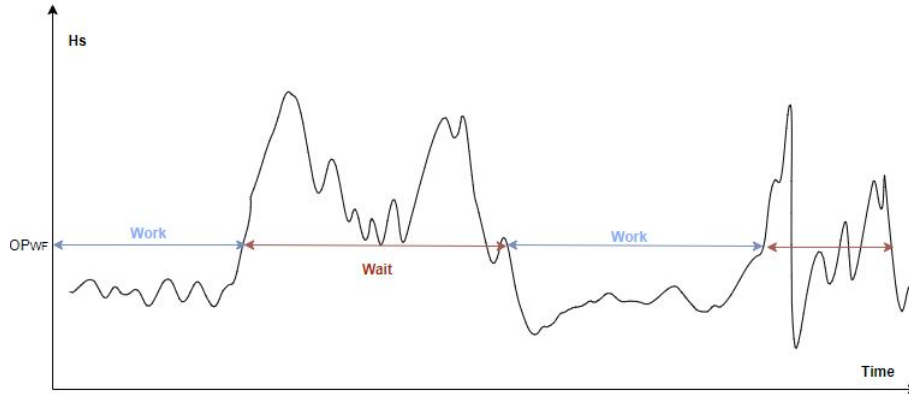


**Figure 2.2:** Varying significant wave height with associated working and waiting times. (Larsen (2019b)).

## 2.2 The Planning Process

A marine operation consists of two phases. First comes the planning and design phase, followed by the execution phase (DNV-GL (2011b)). The operation shall be precisely planned and designed with regards to safety for personnel, equipment, and the environment. A marine operation shall be designed after the fail-safe principle. This means that if something goes wrong during the operation, the object will fail to a safe condition. The planning phase has the potential to save much money if it is done wisely. Identifying risks early will help lower the probability of injuries and make right project decisions. The planning and design phase shall identify which part of the year the operation can be performed and provide clear weather criteria for initiating and halting the operation. This is called the availability analysis and is based on historical weather data from minimum of 5-10 years (DNV-GL (2011b)).

Reviewing relevant standards is an essential part of the planning phase. The standards contain guidance on how to perform safe operations. The VMO standards from DNV-GL provides knowledge on how to perform safe marine operations. These standards contain safety-, load-, and material factors and guidance notes to ensure a probability for structural failure less than 1/10000 per operation (DNV-GL (2011a)). It is advisable to split the planning phase in the following plan:

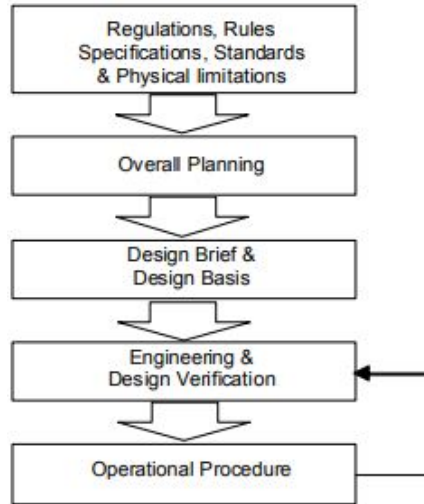


**Figure 2.3:** Recommended planning and design sequence (DNV-GL (2011a)).

The planning should start with identifying rules, regulations, and existing physical limitations. In the engineering phase, it is helpful to take advantage of computer software to run simulations which can be included in the operational procedures. This is advantageous in terms of showing graphically how the operation shall be done for all involved parties, maintaining safety, and preventing unnecessary time spent due to ambiguities. The procedures are extensive work and should prevent any adverse events from occurring and ensure that everything goes according to plan. The following is taken from DNV-GL (2011a), and gives a detailed proposal on the planning phase.

1. Identify relevant and applicable regulations, rules, company specifications, codes and standards, both statutory and self-elected.
2. Identify physical limitations. This may involve pre-surveys of structures, local conditions and soil parameters.
3. Overall planning of operation i.e. evaluate operational concepts, available equipment, limitations, economical consequences, etc.
4. Develop a design basis describing environmental conditions and physical limitations applicable for the operation.
5. Develop design briefs describing activities planned in order to verify the operation, i.e. available tools, planned analysis including method and particulars, applicable codes, acceptance criteria, etc.
6. Carry out engineering and design analyses.
7. Develop operational procedures.

## Chapter 3

# Mooring Systems

This chapter present possible mooring systems to be used for floating wind turbines. This includes different anchor concepts available for the industry.

The mooring system can be categorized as a safety critical system (SCS). A SCS is a system where the consequence of failure results in fatal events, i.e., damage to people, equipment, and the environment (Rausand (2014)). The main functional requirements of the mooring system are to prevent large horizontal offsets for the floating object so that it stays in place in its intended position. This is to maintain safety in terms of other moored objects nearby and prevent damage on e.g., umbilicals and risers attached to the structure. For a floating wind turbine, this will mainly be the connected power cable. Another critical aspect is that the mooring system must absorb the wave frequencies (Larsen (2019d)).

There exist several different station keeping systems. For a floating wind turbine, the most suitable method will be a taut leg or a catenary system. Both systems use embedded anchors at the seabed connected to the turbine with anchor lines. The difference lies in the configuration of the system and the anchor line material.

### 3.1 Catenary System

Catenary mooring systems (CMS) will have the mooring lines freely hanging down to the seabed by gravity. From here, the catenary lines lie horizontally on the seabed with a length such that it is larger than the water depth, usually 5-20 times larger (Chakrabarti (2005)). By doing so, the anchors will only be exposed to horizontal forces, making it possible to use easy-installation anchors such as drag embedded anchors. The restoring force acting on the moored structure will come from the enormous weight of the catenary lines. These lines usually consists of heavy chain in combination with wire ropes. The catenary system can be seen in figure 3.1. This is a conventional mooring system and has proven to be a reliable system over the years. The easy-installation and flexibility when it comes to water depths makes this an excellent alternative to use for a floating wind farm.

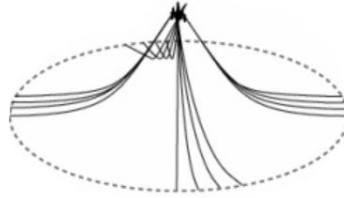


**Figure 3.1:** Catenary mooring system (ABC-Moorings (2019)).

### 3.2 Taut Leg System

In a Taut leg mooring system, synthetic fiber lines are used. The fiber lines are elastic compared to the catenary chain, making them a good absorber of dynamic motions. The fiber lines are shorter and lighter per meter, making them more practical to handle during deep-water installations. Using a taut system leads to reduced seabed footprint (Chakrabarti (2005)). The mooring layout can be seen in figure 3.2.

In this mooring layout, the mooring lines are pre-tensioned and touch the seabed at an angle, usually around 30-40 degrees (ABC-Moorings (2019)). Because of this angle, the anchors that are used in the system will have to withstand vertical and horizontal forces (unlike for a CMS where the mooring lines are laid horizontally only generating horizontal forces).

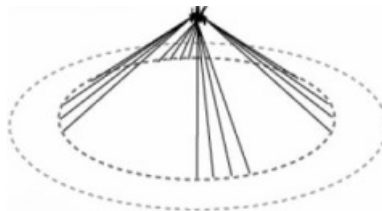


**Figure 3.2:** Taut leg mooring system (ABC-Moorings (2019)).



### 3.3 Anchor concepts

Anchors are installed on the seabed to be a fixed connection point for the mooring lines. There are several different types of anchors that are used by the industry today. The two most common ways in which an anchor is attached are either by suction force or self-weight. The choice of anchor type depends on multiple factors. The soil profile at the location can be a limitation for some anchor types, as the tip resistance is increasing with the depth under the seabed. The anchor types have different loading capacities in different directions. Anchors with high vertical loading capacity can be used for mooring of e.g., a tension leg platform. Some anchors can only be used for horizontal directions.

The different anchor types also have different installation methods. The installation method will characterize the financial part of the project, and in marine operations, this is important to keep to a minimum. In some projects, the anchor must meet the requirements in terms of loading conditions, precision of positioning, and quick installation for the completed project. An example of such a project is the Equinor's Hywind tampen and will be discussed later.

#### 3.3.1 Suction Anchor

A *suction anchor* (SA) is a widely used anchor type for the mooring of offshore structures. The anchor is a giant steel bucket that is held in place by vacuum. The SA is transported by offshore construction vessels (OCV) or if needed on barges. If it is transported on a barge, typically, an OCV is brought out to lift the anchor from the barge with its crane. The anchor is open in the bottom and closed at the top and can weight up to 170 tons (*Offshore Magazine* (2007)). In the top, the anchor has venting holes for evacuating air as it is lowered through the splash zone. These holes are also used as an interface for pumping water out of the caisson by using ROV's.



**Figure 3.3:** Suction anchor (Hansen (2013)).

This anchor type is popular because it is relatively easy to install and can withstand

both horizontal and vertical loads (Halse (2019)). The anchor is lowered to the seabed, where a remotely operated vehicle (ROV) is used to monitor the positioning to ensure the anchor is placed in an approved location. The crane is used with precision to ensure safety and to prevent damage to the anchor. When the SA hits the seabed, it will self-penetrate due to its weight. When this is done, an ROV is used to pump trapped seawater from the caisson by creating a vacuum. By doing this, the anchor is embedded down into the seabed (Ma et al. (2019)).

On the lower part of the SA (Figure 3.4), there is a pad eye where the mooring line is connected. The tension from the pad eye gives a transverse tension in the anchor. When a horizontal load is applied, the soil will, therefore, support the anchor at its maximum. The SA is also effective on vertical or inclined loading conditions, and can thus be used for the taut mooring system.

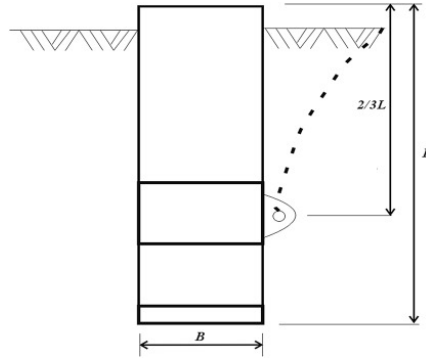


**Figure 3.4:** Pad eye on an embedded suction anchor (Bai and Jin (2016)).

### 3.3.2 Fluke Anchors

*Drag embedded anchors* (DEA) (figure 3.5a) rely on horizontal loading. The anchors are dropped from an anchor handling vessel (AHV) and is embedded into the seabed with force. Later tensions in the mooring line will dig the anchor deeper. This anchor type is low-cost and easy to install. Precise placement of the DEA during installation is not easy; this makes it a convenient anchor type for catenary systems where the exact placement of the anchor is less important than taut leg. The DEA has high load capacity in horizontal directions, but not in vertical directions.

To improve the vertical load capacities of the DEA, another concept has been developed. This is called *Vertical load anchors* (VLA) and can be seen in figure 3.5b. The VLA is installed in the same way as the DEA and can be used in taut leg mooring systems (Vryhof (2010)). The VLA's have a high level of efficiency in vertical loading conditions compared to suction anchors. This efficiency is simply calculated from a ratio based on the highest allowable force and the weight of the anchor (Aubeny (2016)). This is because the vertical projected area of the "buried" VLA is more efficient than that based on friction.

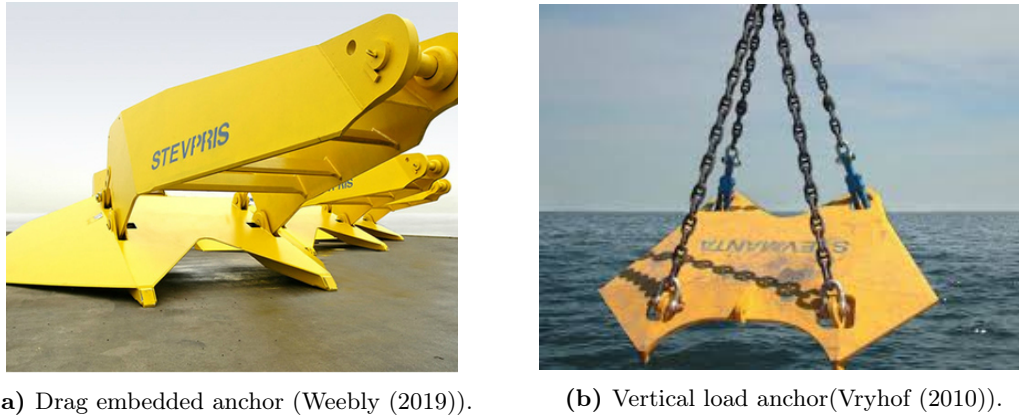


**Figure 3.5:** Drag embedded vs. vertical load anchor.

### 3.3.3 Deep Penetrating Anchors

*Deep penetrating anchors* (DPA) are installed by being released from a distance above the sea bed (usually 70m - 100m) in which gravity is used to penetrate the surface with great force. The anchor has an optimized, dynamic design that allows it to achieve velocities up to 30 m/s at the time of impact. The level of penetration into the sea bed depends on local sea bed sediments and can vary in deformation characteristics (Deepsea anchors (2019)).

The DPA installation method is less time consuming compared to the SA as the installation of the DPA is finished when the anchor is dropped. This gives reason to believe that the concept have great potential if a large numbers of anchors need to be installed. The small projected areas of the DPA leads to limited hydrodynamic forces as the anchor is lifted through the splash zone. This can result in a lesser weather-sensitive marine operation with a higher operational criterion compared to e.g., a suction anchor (Hove (2001)). Other benefits may be simple installation by one specialized vessel only. Solutions to attach multiple lines to the DPA to reduce the number of anchors and installation costs considerably exist (Lieng (2020)). The DPA can be used for any load angle, low sensitivity to large water depth, and applicable for taut systems.

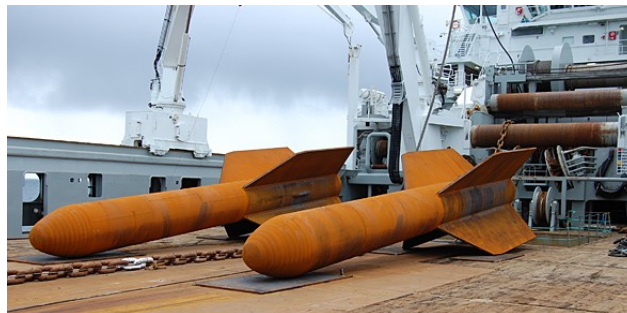


**Figure 3.6:** Deep penetrating anchors (Deepsea anchors (2019)).

### 3.3.4 Driven Pile Anchor

Driven piles are a very popular concept in the offshore oil production industry. The piles are installed by using a pile driving vessel equipped with a vibratory or impact hammer to knock the piles down into the seabed. The driven piles are proven to be a reliable method and can be used when high precision in terms of positioning is needed. The anchors can withstand high loads in both horizontal and vertical loading. The main disadvantage is the extensive process involving the pile driving vessel which contributes to high costs (Aubeny (2016)).

## 3.4 Mooring of Floating Wind Turbines

For the mooring of a floating wind farm, the basic idea is using multi-line attachment at the anchor, as seen in Figure 3.7. This is because the wind farm consists of several wind turbines moored together in a network, connected to the same anchors. Hywind Tampen is a wind farm project consisting of 11 wind turbines based on Equinor's floating offshore wind concept Hywind (Equinor (2019)). A typical mooring layout for a wind turbine is three lines equally spread down to the anchors. With 33 mooring lines, the quantity of anchors for Hywind Tampen is expected to be around 19.

In such a network, where multiple turbines are moored to the same anchor, forces in multiple directions is expected. This makes it challenging to use anchors that rely on one direction horizontal forces only. The driven piles will be a costly solution because of the large number of anchors installed by the expensive vessel. The drag embedded anchors will not be able to withstand the loading conditions due to the multi-line attachment. The needed properties from the network of turbines, makes the suction anchor and DPA good alternatives. The anchors must operate with multiple loading directions and have the ability to be efficiently installed to keep costs to a minimum. However, logistical problems may arise, especially with suction anchors as the Hywind tampen field is located 140 kilometers from shore (Equinor (2019)), and transport of the anchors may be expensive.

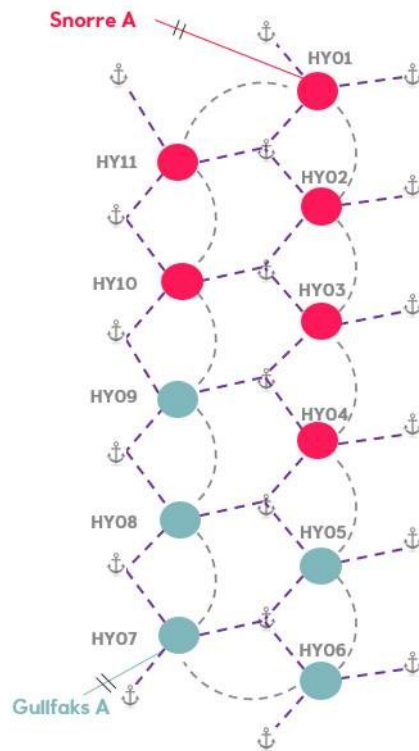


**Figure 3.7:** Wind farm network ( DOF (2019)).

The suction anchor and the DPA both have qualities that a floating wind farm requires for its mooring system. The installation and especially the lifting operation of the anchor is a weather critical activity. Different lifting methods by use of crane vessels is presented in the following chapter.



## Chapter 4

# Subsea Lifting and Installation

According to DNV-GL (2014), *The crane, crane vessel, and lifting equipment shall be in good condition, properly manned for performing the intended operations.* The crane should be equipped with a load monitoring system with an accuracy of 5% of the crane capacity. During the operation, the vessel should be moored or positioned with a reliable Dynamic Positioning (DP) system. Limiting operational conditions must be assessed, and a combination of the following parameters should determine the operational limit (DNV-GL (2014)):

- Dynamic amplification factor (DAF)
- Wind speed
- Crane wire angle tolerances
- Heel and trim of the crane vessel
- Crane tip motion and acceleration due to waves
- Stability of the vessel as the object is lifted
- Wave conditions

Several different lifting methods can be used for subsea installations. This depends on the lift category of light and heavy lifts. Light lifts are lifts of objects that are typically less than 1-2 % of vessel displacement. Heavy lifts involve objects more than 1-2 % of vessel displacement (typically above 1000 tons). These lifts will impact vessel stability, and there will be a dynamic coupling between the vessel and the lifted object (Larsen (2019a)). Three common lifting methods will be briefly described: lift through moonpool, lift by a special handling system (SHS), and a lift over-the-side.

## 4.1 Lifting Methods

### 4.1.1 Moonpool

Moonpool is a tool installation-vessels, rigs and drillships have for lowering instruments and objects into the water. The Moonpool is an opening in the hull that provides good protection of the object as it is lowered through the splash zone, thus increasing operability. It can also be an advantage regarding the stability of the vessel as it avoids unnecessary heeling moment. The moonpool is also used by the vertical lay system (VLS). This system is used to lay cable vertically straight into the sea while the ship is slowly moving forward. This is done by mounting the VLS over the moonpool. The location of the moonpool is normally located so that operations can be performed with minimal angular motions. This will be where the roll and pitch axis intersects.

The dynamic forces acting on the object in a moonpool will come from the natural period of the oscillating (vertical direction) water in the water plug. If the resonance period of the water plug comes close to the wave period, it can provide a significant response, and this will not be desirable. The motion of the water inside the moonpool is dependent on the level of damping. Damping inside the moonpool is provided by viscous effects from the walls and other structures inside the moonpool (Larsen (2019a)). The natural period of the oscillating water can be calculated by equation 4.1 (DNV-GL (2011b)).



**Figure 4.1:** Moonpool (Bourbon Offshore (2020)).

$$T_o = 2\pi \cdot \sqrt{\frac{D_m + 0.47 \cdot \sqrt{A_m}}{g}} \quad (4.1)$$

In equation 4.1  $D_m$  is the moonpool diameter,  $A_m$  is the constant moonpool area and  $g$  is the gravitational acceleration.

### 4.1.2 Special Handling System

A vessel equipped with a special handling system (SHS) will have significant handling of the object and can be operated in sea states up to  $H_s = 4.5m$  (AXTech (2020)). This is with a safe working load (SWL) of 420t. An SHS consists of a frame and a tower that guides the object controlled through the splash zone. The disadvantage of this system is the high cost and that only one vessel has this on the menu (the offshore installation and IMR vessel North Sea Giant).



### 4.1.3 Over-the-side

This method involves using the vessel's crane to lift the object from the deck and over the side into the depth. The method is flexible in terms of object shape and weight and can be used on many different layouts. Over-the-side crane operations are the most common lifting method in today's marine operations. This is because of the wide range of possibilities this method inhabits. The method is cheaper than the SHS because of the availability of vessels that can provide this kind of lift. The lift over-the-side is used for installations of modules, anchors and is also used for recovering operations.

By use of the vessel crane for installation of sub-sea equipment, the handled object is exposed to direct wave excitation forces through the splash zone. The operability of the installation depends on the operational limit that, in some cases, is decided from crane wire tension. This method allows for significant force contributions during the phase through the splash zone, which can be a limitation. In this thesis, the crane operation of a DPA and a SA is simulated using the lift over-the-side method. A more detailed approach to the lifting phases from an over-the-side crane operation is described in the following section.



**Figure 4.2:** Vessel main crane (Hansen (2013)).

## 4.2 Suction Anchor Installation

When installing the suction anchors, a lift over the side is performed using the vessel crane. When sea fastenings are cut, the next safe condition for the anchor will not come until it is landed on the seabed with slack in the crane wire. The weather window must be sufficiently large to contain the whole operation from safe condition to safe condition without the risk of damage to the anchor or safety for vessel and crew.

### 4.2.1 Phase 1: Lift-off

This phase includes cutting sea fastenings, connecting the lifting arrangement to the anchor, and getting the anchor ready for over boarding. Usually, the deck of the vessel will be equipped with "rails" that guides the anchor towards the over boarding zone for increased control. When weather forecast allows, the operation can start, and sea fastenings can be removed. The duration is dependent on the type of sea fastenings but typically around 1.5 hours (Jørdre (2020)).

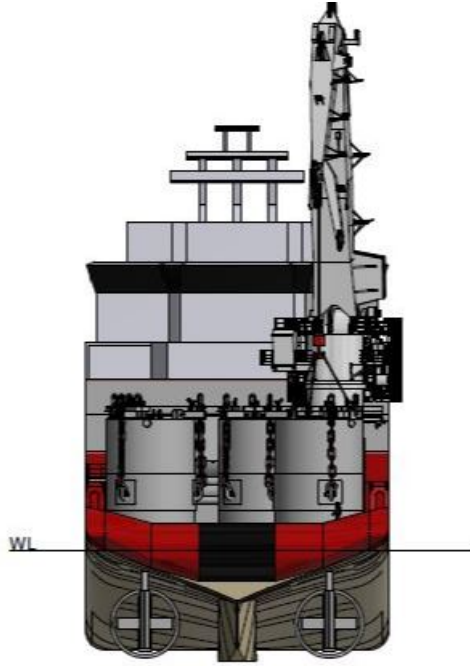


**Figure 4.3:** Lift of from Skandi Skansen (DOF (2019)).

The lift-off is initiated when the engineers, together with the commanding officer, approves. The crane hook should be positioned above the center of gravity of the anchor, and no vertical constraints should be present when lift is initiated (DNV-GL (2014)). Ballasting of the vessel should be considered prior to lift-off to maintain stability when the object is lifted. As mentioned, the next safe condition will not come until the anchor has landed on the seabed. A sufficiently large weather window to contain the whole operation must therefore be present.

#### 4.2.2 Phase 2: Object in Air

As the anchor is lifted and in air, the anchor will immediately gain horizontal motions relative to the vessel. Uncontrolled motions of the anchor is critical to consider for safety reasons.

The stability of the vessel must be considered. This depends on the weight of the anchor relative to the ship and the moment arm that occurs when the crane rotates the anchor over the ship side. The need for ballasting for stability corrections should be discussed before this phase.

The static hook load ( $SHL$ ) can be used to find the resulting dynamic load that the anchor will apply the system when lifted. The  $SHL$  is calculated from the mass of the anchor and rigging in air. Dynamic effects are included through a dynamic amplification factor ( $DAF$ ), which is multiplied with the  $SHL$  and added to additional loads due to wind and tugger lines ( $F(SPL)$ ) (Equation 4.2). The  $DAF$  is calculated from

table 3-1 in *DNV-OS-H205* based on the *SHL* of the lifted object and lifting location (inshore/offshore).

$$DHL = DAF \cdot SHL + F(SPL) \quad (4.2)$$

**Table 3-1 Dynamic Amplification Factors<sup>1)</sup>**

<i>SHL (Static Hook Load)</i>	<i>DAF Onshore</i>	<i>DAF Inshore</i>	<i>DAF Offshore</i>
3 <sup>2)</sup> – 100 t	1.10	$1.07 + 0.05\sqrt{100/SHL}$	$1 + 0.25\sqrt{100/SHL}$
100 - 300 t	1.05	1.12	1.25
300 - 1000 t	1.05	1.10	1.20
1000 - 2500 t	1.03	1.08	1.15
> 2500 t	1.03	1.05	1.10

1) See Guidance Notes in [3.2.2.4].  
 2) For objects weighing less than 3 tonnes it is recommended to assume an object weight of 3 tonnes and use this throughout the calculations.  
 3) See [6.2.3.2] for recommendations to moving cranes onshore.

**Figure 4.4:** DAF as found in standard (DNV-GL (2014)). t is the weight in tons.

### 4.2.3 Phase 3: Object Crossing Splash Zone

When the anchor is lowered through the splash zone, direct wave excitation forces from the Morison equation is acting on the system. This is the drag and inertia forces coming from the relative motion between the lifted object and the water particles. A suction anchor has an enormous added mass contribution because of the large amount of entrapped water, resulting in a large slamming force in this phase. The hydrodynamic force contributions are described in detail in Section 5.4.

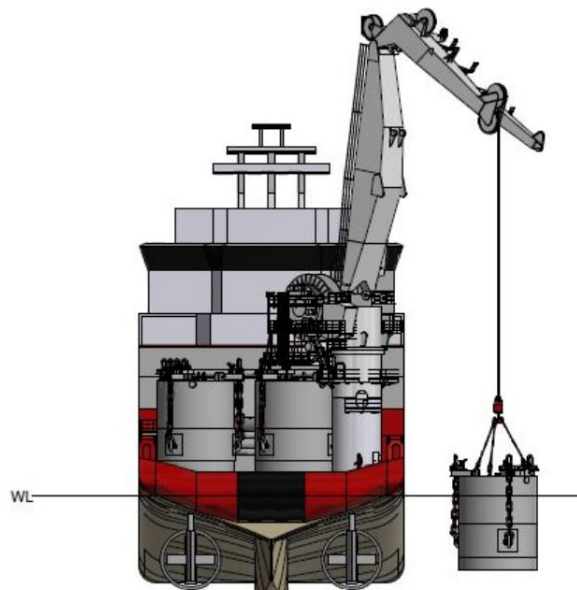


**Figure 4.5:** Suction anchor lowered by Skandi Skansen through splash zone (DOF (2019)).

This phase is usually the most critical phase for the crane operation. The amplitude of the direct wave excitation forces are dependent on object shape and wave conditions. In the splash zone, the anchor has contact with both air and water simultaneously. The anchor behavior, when interacting with the waves in the splash zone, is crucial in determining the operational limits. This is because the forces acting on the anchor is directly transferred to the slings and crane wire.

The lift through the splash zone is a weather-critical activity, and the duration depends on hoisting velocity and object size. The duration of the lift-off and the lower through splash zone are assumed to be around 2 hours for the SA.

#### 4.2.4 Phase 4: Object submerged

When the object is submerged, the lowering is initiated. In some cases, if the lifted object contains entrapped air, the object may hang for a while until the air is evacuated. The lowering of the suction anchor through the water column should be monitored by ROV's. This is to get information about the state of the lifted object throughout the lowering and have the ability to detect any error that might occur with e.g., rigging early.

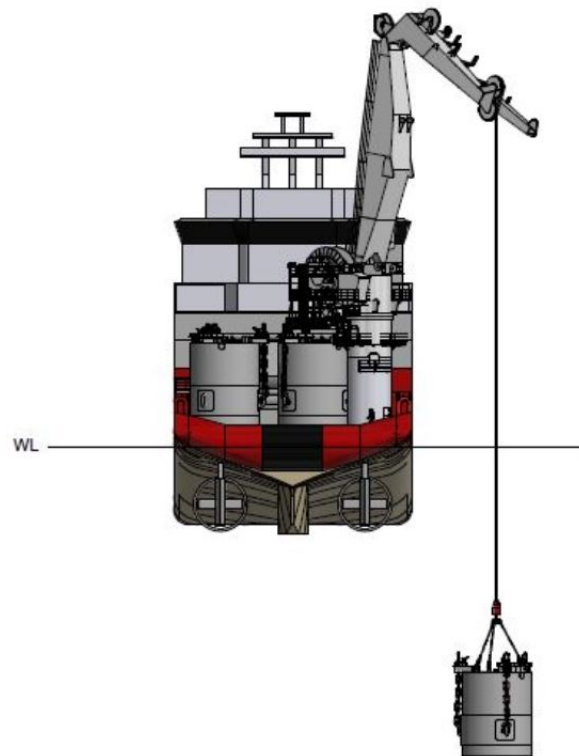


**Figure 4.6:** Anchor lowered by Skandi Skansen (DOF (2019)).

Time consumption from this phase depends on water depth. Larger horizontal offsets must be expected at vast water depths with currents present. Some anchor types require high precision in positioning during installation. The horizontal offset estimation can be done by considering the horizontal drag force of the anchor and lifting wire, together with the weight of the anchor, and calculate the moment about the crane tip. With vast water depths, it is also necessary to consider the delay between the vessel and the anchor in terms of movement response.

In the case of large wave-induced movements in the vessel, movements in the crane tip can cause oscillation at the object and dynamic resonance. If this is the case, heave compensation can be used to minimize the response in the object. As the anchor is lowered into the depth, the hook load in the lifting increases with cable length. When the cable length is increased, the system's vertical resonance period ( $T_\eta$ ) increases (Larsen (2019a)). In equation 4.3,  $m_w$  is the weight of the hoisting wire per meter,  $M$  is the anchor weight,  $A$  is the vertical added mass,  $K_E$  is the elastic stiffness, and  $L$  is the length of the hoisting wire.

$$T_\eta = 2\pi \cdot \sqrt{\frac{M + \frac{1}{3} \cdot m_w L + A}{K_E}} \quad (4.3)$$

The anchor is lowered to approximately five meters above the seabed (DOF (2019)). Here an additional ROV is used to dock onto the anchor for assisting with positioning control. The duration is dependent on water depth. At the Tampen area, the water depth is approximately 300 meters (Equinor (2018)) which results in a 30 minutes lowering with 0.2 m/s.

#### 4.2.5 Phase 5 and 6: Anchor Landing and Installation

When the anchor is landed on the seabed, a safe condition is reached as the crane wire can be disconnected if necessary. The final installation phase where the anchor is sucked into the seabed may be done with a new operational limit, as this phase can be done without exposing the crane wire for enormous tension by creating some slack in the wire.

The landing itself can be done safely using heave compensation on the crane winch. It is expected that the suction anchor will self-penetrate into the seabed due to its own weight. Another ROV is employed for pumping seawater out of the caisson. This creates a vacuum so that the suction anchor is fully fastened. Time consumption is dependent on the size of the anchor and volume of entrapped water to be pumped, usually around 1.5 hours (Jørdre (2020)). In step 6, the anchor is installed. The ROV's disconnect the lifting arrangement are retrieved.

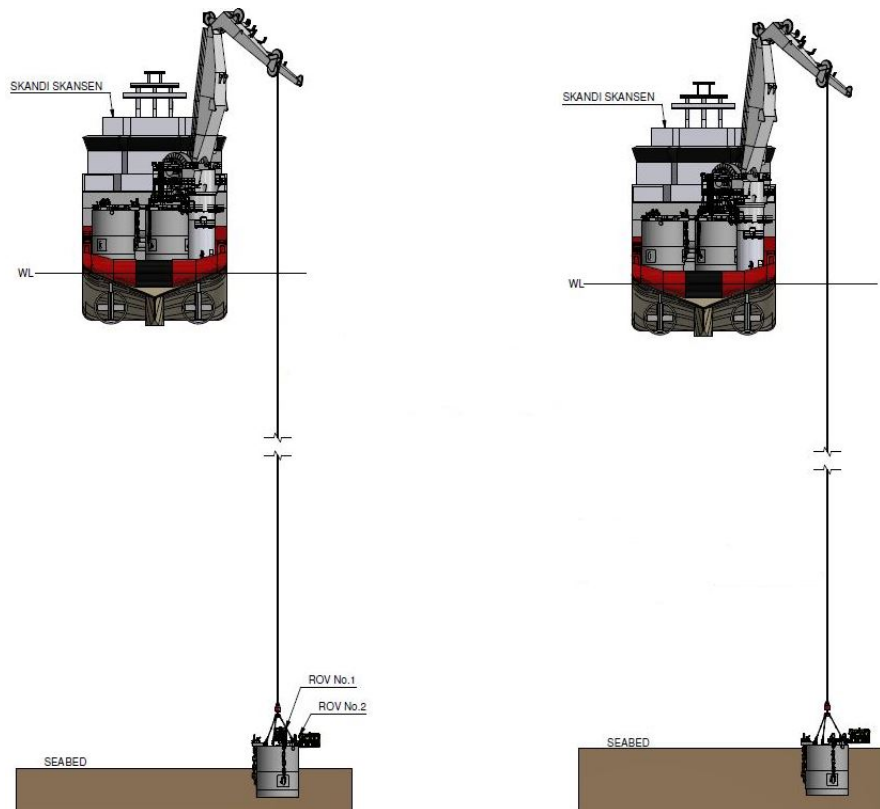


Figure 4.7: Anchor landed and fastened (DOF (2019)).

### 4.3 Deep Penetrating Anchor Installation

There are multiple ways to install a DPA. One method is by using an anchor handling vessel (AHV) to guide the anchor over the stern using a winch (Figure 4.8). And then lower the anchor until it has reached the desired height above seabed before disconnecting the anchor. The disconnection can be done in multiple ways. ROV manipulation or mechanical methods using deck tugger lines are the most common. When the anchor is disconnected, the gained kinetic energy is used for penetrating deep into the seabed. The DPA can also be installed over-the-side with a crane vessel. The first steps of this method are similar to those used for suction anchors.

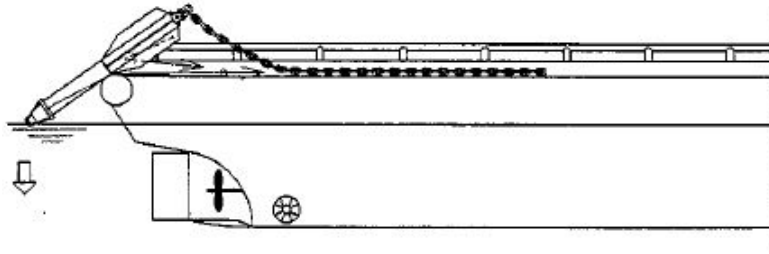
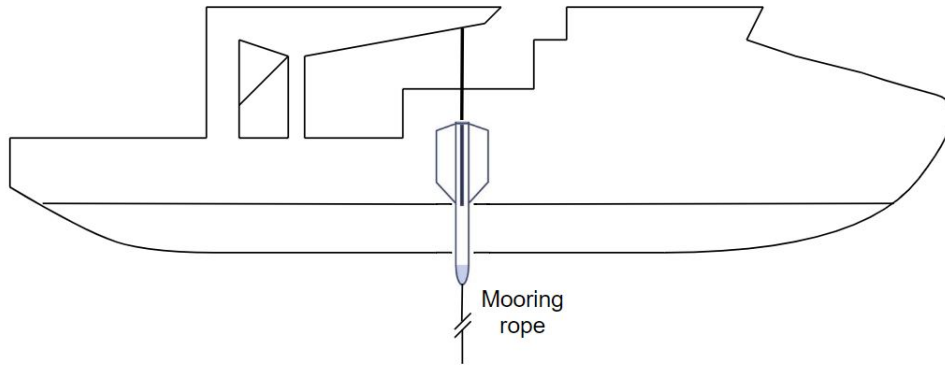


Figure 4.8: DPA installed from the stern of vessel (Hove (2001)).

DPA's are anchors with significantly smaller surface area than a suction anchor of the same dimensions. For the SA installation, the operational limit is often determined based on crane wire tension through the splash zone. The DPA geometry provides the basis for believing that an installation of this anchor type will have higher operational limits. This is utterly because the DPA with its smaller surface area will be less responsive to wind and waves and, therefore, can be handled in rougher weather environments. In theory, this leads to greater availability of weather windows and cheaper operations.

The differences in DPA installation lie in how many vessels that are used and how the permanent anchor line is handled during installation. Sometimes two ships are used where one handles the anchor while the other handles the permanent anchor line. The method illustrated here is a simple and effective method created by Delmar (2020). The system is called OMNI-max, and the installation is done by attaching a mooring rope on the anchor itself that is laid on the seabed before penetration is initiated, and attaching the mooring line to the pre-laid mooring rope later. The OMNI-max system can be installed by over the stern like in figure 4.8, or over-the-side by the vessel crane (Shelton (2020)).



**Figure 4.9:** DPA hoisted through the splash zone.

As mentioned, the first phases of the lift will have the same vulnerabilities as the suction anchor (phases 1,2, and 3). Figure 4.9 shows a DPA being lifted over-the-side with the main vessel crane through the splash zone. The anchor is lifted over the vessel side with an attached mooring rope. This rope is landed on the seabed before the anchor is disconnected from the hoisting wire (Figure 4.10). The length of the rope must be over 50 m, as this is the drop height needed for sufficient penetration (Delmar (2020)). At the same time, an ROV is being used to observe the anchor and the mooring rope.

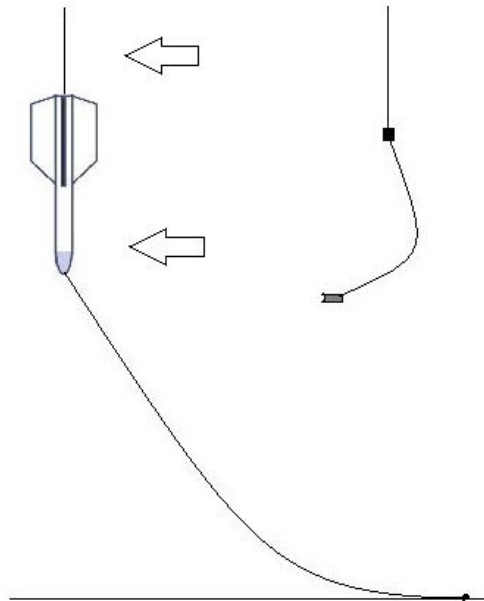


**Figure 4.10:** Mooring rope landed on the seabed. Vessel carefully moves to intended drop location.

Depending on the length of the deployed hoisting wire, the recoil from the drop must be considered. A shock reduction component such as a segment of chain between the main crane and the anchor could be beneficial to avoid any shock load on the crane. This also depends on the weight and size of the anchor.



When the anchor is disconnected, the gained kinetic energy allows the anchor to penetrate the seabed. The level of penetration depends on seabed soil conditions. The installation is hence rather simple and has the potential of being time-efficient. However, the consolidation of the plowed seabed soil may require some days or weeks for the anchor to be appropriately embedded. This means that there will be some waiting time before the anchor can be operative after its installation. According to Shelton (2020), six hours is a reasonable estimate for the installation operation of the DPA.

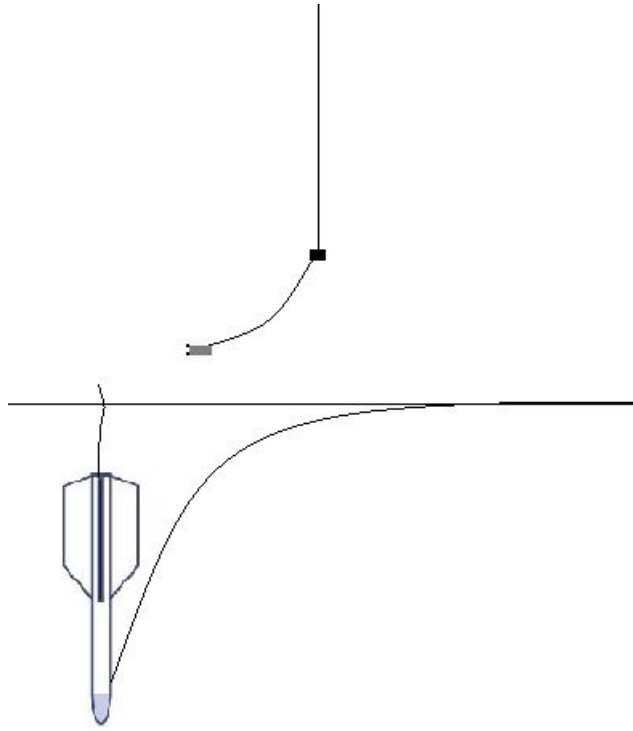


**Figure 4.11:** DPA installed. Mooring rope lays on sea bed ready to be picked up.



# Chapter 5

## Hydrodynamics

Relevant theory needed to understand the hydrodynamic forces that is present during an crane operation at sea will be described. This includes the theory used by the numerical simulation software to calculate crane wire tension.

### 5.1 Linear Wave Theory

Linear wave theory (often referred to as Airy wave theory) can be used to calculate wave forces manually. Here, regular waves with various assumptions are used to describe water behavior. The water particles are assumed to be incompressible and inviscid, and the fluid motion irrotational. A velocity potential can then be used to describe the velocity of the fluid. Given that the pressure satisfies the Bernoulli equation the velocity potential can be written as in Equation 5.1 (Faltinsen (1990)).

$$\phi = \frac{g\zeta_a}{\omega} e^{kz} \cos(\omega t - kx) \quad (5.1)$$

- $\zeta_a$  = Wave amplitude [m]
- $g$  = Gravity acceleration [ $\frac{m}{s^2}$ ]
- $\omega$  = Wave frequency
- $z$  = Depth [m]
- $t$  = Time step [s]
- $k$  = Wave number ( $k = \frac{2\pi}{T}$ )
- $T$  = Wave period [s]

Regular waves have a distinct height, length and wave period. The wave elevation for a sinusoidal incident wave at deep water can be written as in Equation 5.2.

$$\zeta = \zeta_a \sin(\omega t - kx) \quad (5.2)$$

The fluid kinematics decrease with depth under the wave profile. The vertical velocity and acceleration of a fluid particle at a specific location under a wave crest can be found from Equation 5.3 and 5.4 respectively. Horizontal motion components are not included here, the only adjustment to equations 5.3 and 5.4 for horizontal motions will be the sine and cosine parts (Faltinsen (1990)).

$$w = \omega \zeta_a e^{kz} \cos(\omega t - kx) \quad (5.3)$$

$$a_3 = -\omega^2 \zeta_a e^{kz} \sin(\omega t - kx) \quad (5.4)$$

## 5.2 Irregular waves

A set of regular waves can be used to describe a realistic sea state. Ocean waves will behave in an irregular manner with random elevation and consist of multiple different-sized waves.

### 5.2.1 Wave Spectra

A useful property from linear theory is that we can add results from regular waves and create irregular sea states, i.e. the superposition principle is valid. The wave elevation can thus be written as in Equation 5.5.

$$\zeta = \sum_{j=1}^N \zeta_{aj} \sin(\omega_j t - k_j x + \epsilon_j) \quad (5.5)$$

Here,  $\zeta_a$  is the wave amplitude and  $\epsilon$  is the random phase angle (between 0 and  $2\pi$ ) of the wave component number  $j$ .  $\zeta_a$  can be expressed by a wave spectrum i.e.

$$\frac{1}{2} \zeta_{aj}^2 = S(\omega_j) \Delta\omega \quad (5.6)$$

Where  $S(\omega_j)$  is a wave spectrum, and  $\Delta\omega$  is a constant phase difference of the successive frequencies. As for the wave elevation, the superposition principle can be used to obtain other irregular wave properties. The behavior and response of offshore structures in irregular waves can thus be approximated as the sum of regular waves. The relationship between the time domain solution (equation 5.5) and the frequency domain solution ( $S(\omega)$ ) for the waves is illustrated in Figure 5.1. The time series used to create wave spectrum's are made by buoys located at specific locations at the open ocean. These buoys are equipped with measurement tools designed to measure multiple parameters

several times a day e.g. wave height, wave period and wind speed.

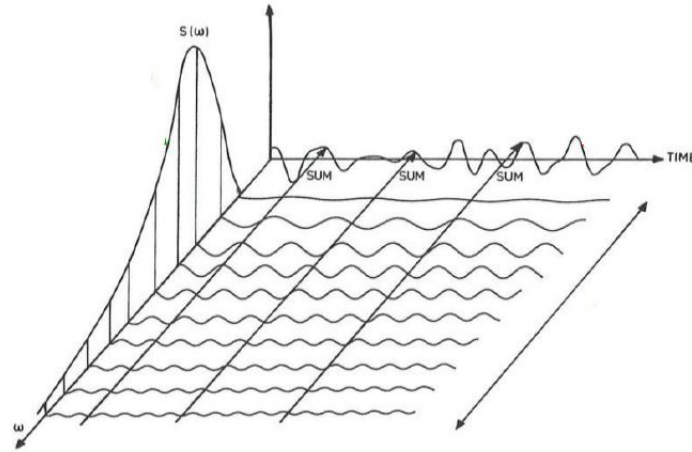


**Figure 5.1:** Time domain and frequency domain in same illustration (Faltinsen (1990)).

The measurement process is assumed to be a stationary random process, which means that the process is a stochastic process whose unconditional joint probability distribution does not change when shifted in time. The measurement is a short-term description of the waves i.e. of finite duration (1/2 hour to 10 hours).

To describe real ocean wave characteristics in a realistic manner, idealized wave spectra are developed. Recommended sea spectra from International Ship and Offshore Structures Congress (ISSC) and International Towing Tank Conference (ITTC) can be used. The ITTC recommend using the Pierson-Moskowitz (PM) spectrum for fully developed sea states (Faltinsen (1990)). This spectrum is based on big amounts of weather data from the North Atlantic Ocean. The PM-spectrum is created from wind blowing steadily over a great distance until the waves comes to a state of equilibrium (fully developed sea state). A great distance in this case is roughly five thousand wave lengths on a side (WikiWaves (2012)).

In a later conference, the ITTC recommended a joint North Sea wave project (JONSWAP) to be used. The JONSWAP spectrum is a PM-spectrum multiplied with a peak enhancement factor. This is a correction to the PM-spectrum due to that the sea is never fully developed. The JONSWAP spectrum is made from a significant wave height ( $H_s$ ), a peak frequency ( $\omega_p$ ) and a peakedness parameter ( $\gamma$ ). A comparison of the spectrum's can be seen in Figure 5.2. The total energy is the same in both spectrum's. The difference lays in the energy distribution along the axis.

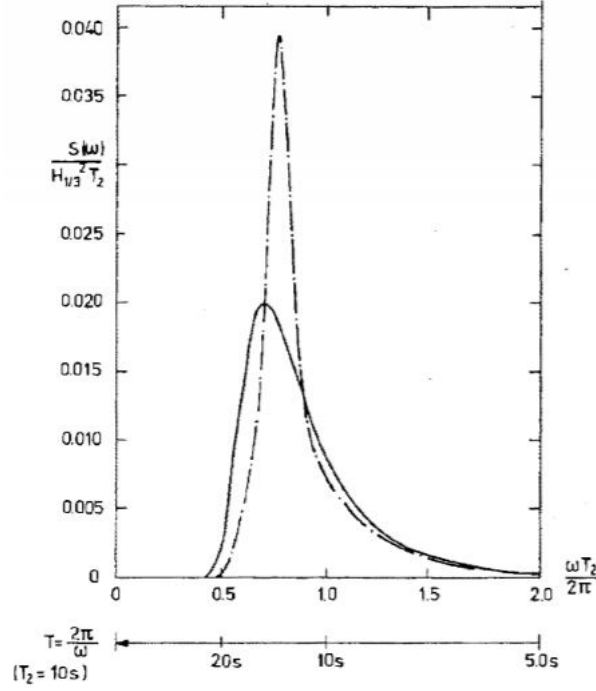


**Figure 5.2:** Pierson-Moskowitz and JONSWAP spectra (Faltinsen (1990)).

As seen in Figure 5.2 the spectrum's have different peak periods. A greater amount of the energy is concentrated around the peak for the JONSWAP spectrum. The JONSWAP spectrum is described by the following equation (Faltinsen (1990)).

$$S(\omega) = 155 \frac{H_s^2}{T_1^4 \omega^5} \exp\left(\frac{-944}{T_1^4 \omega^4}\right) (3.3)^Y \quad (5.7)$$

- $Y = \exp\left(-\left(\frac{0.191\omega T_1 - 1}{2^{0.5}\sigma}\right)^2\right)$
- $\sigma = 0.07$  for  $\omega \leq 5.24/T_1$
- $\sigma = 0.09$  for  $\omega > 5.24/T_1$

Here  $H_s$  is the significant wave height defined as the mean of the largest one third of the measured waves.  $T_1$  is a mean wave period and is defined by equation 5.8.

$$T_1 = \frac{2\pi m_0}{m_1} \quad (5.8)$$

$$m_k = \int_0^\infty \omega^k S(\omega) d\omega \quad (5.9)$$

### 5.2.2 Seed Waves

The seed number of the simulation decides the amount of data that is produced from a simulation. A large seed number results in many simulations and good quality data. The random seed wave is a parameter to increase the randomness of the phase of the waves. This helps to create diversity in the applied condition in the simulation. Adding random seed waves to the condition results in a condition set with a constant significant wave height, wave direction, and peak period. The condition is then simulated several times with different seed numbers. As a result, the model is exposed to several variants of the same wave condition, only with a phase shift. Sometimes we can achieve "good enough" results with a smaller seed number, thus drastically reducing the simulation time.

## 5.3 Time Domain Analysis

In general, the time domain analysis is an analytical tool that can be used on physical signals, mathematical functions, and various other variables with respect to time. The time-domain solution differs from the frequency domain solution described in the previous section. The frequency domain is described by the energy spectrum and shows how much of the signal lies within a specific frequency band amongst multiple frequencies. The time-domain solution outputs a realization of the response with time. A time-domain analysis considers non-linear effects, which is time-consuming and complicated. This makes computer software's well suited for this task. This section describes the time domain analysis for a lifting operation at sea.

### 5.3.1 The Equation of Motion

The equation of motion is important when estimating dynamic forces on a system. This equation considers dynamic forces by having a time dependent solution. The equation of motion for heave direction is given in Equation 5.10 (Larsen (2019a)).

$$(M + A_{33})\ddot{\eta}_3 + C\dot{\eta}_3 + K\eta_3 = F_3 \sin(\omega t) \quad (5.10)$$

$M$  = Mass [kg]

$A_{33}$  = Added mass in heave [Kg]

$C$  = Damping coefficient [Kg/s]

$K$  = Stiffness coefficient [Kg/s<sup>2</sup>]

$F_3$  = Excitation force in heave direction [N]

$\eta_3$  = Translation in heave [m]

$\dot{\eta}_3$  = Velocity in heave [m/s]

$\ddot{\eta}_3$  = Acceleration in heave [m/s<sup>2</sup>]

$F_3$  = Excitation force in heave [N]

In Equation 5.10, the translation in heave  $\eta$  is equal to  $\eta_0 \sin(\omega t - \epsilon)$ , where  $\epsilon$  is the phase angle between the crane tip motion and the waves.  $\eta_0$  is calculated by Equation 5.11.

$$\eta_0 = \frac{F_3}{K} \cdot DAF \quad (5.11)$$

The dynamic amplification factor (DAF) is included to consider the global dynamic load effects (DNV-GL (2014)), and can be calculated by Equation 5.12. Here,  $\omega_0$  is the natural frequency and  $\omega$  is the wave frequency equal to  $2\pi/T$ .

$$DAF = \frac{1}{\sqrt{(1 - (\frac{\omega}{\omega_0})^2)^2 + \omega^2 \frac{C^2}{K^2}}} \quad (5.12)$$

$$\omega_0 = \sqrt{\frac{K}{M + A}} \quad (5.13)$$

### 5.3.2 Static and Dynamic Equilibrium

The tensions in the crane wire in a lifting operation is a complex problem and are due to multiple factors. The total crane wire tension will be a combination of two contributions: a static and a dynamic force (Equation 5.14).

$$F_{line,tot} = F_{line,static} + F_{line,dynamic} \quad (5.14)$$

The static forces in the lifting wire is given by Equation 5.15. Here the forces come from the object and rigging mass ( $Mg$ ) and time dependent water filling  $m(t)g$  and buoyancy force  $F_b(t)$ . Some porous structures will be filled with water when submerged, therefore the time dependent water filling is included. Equation 5.16 is the time dependent buoyancy force. Here  $V$ ,  $A_w$  and  $\zeta(t)$  is the volume, water plane area and wave surface elevation respectively.

$$F_{line,static} = Mg + m(t)g - F_b(t) \quad (5.15)$$

$$F_b(t) = \rho g V(t) = \rho g A_w \zeta(t) \quad (5.16)$$

The dynamic tension in the crane wire can be found by Equation 5.17. Here  $K$  is equal to  $EA/L$  and multiplied to the relative vertical crane tip and object motion ( $\eta_{ct}$  and  $\eta$  respectively).  $EA$  is the modulus of elasticity of the crane wire and  $L$  is the length.



$$F_{line,dynamic} = K(\eta_{ct} - \eta) \quad (5.17)$$

To find the dynamic line force, we have to study the dynamic equilibrium equation (Equation 5.18). From Newton's second law we know that the force can be found from mass times acceleration. The system get increased inertia when submerged with added mass due to the surrounding water, and the acceleration of the object is dependent on both wave excitation's and heave motions of the crane tip. The relative motion of the object and crane tip is accounted for in the last term of Equation 5.18. We can find the dynamic tension from the dynamic equilibrium equation by solving for the dynamic line force ( $K(\eta_{ct} - \eta)$ ). The hydrodynamic forces consist of the inertia force  $F_I$ , the drag force  $F_D$ , the slamming force  $F_S$  and the buoyancy force  $F_B$  (Larsen (2019a)).

$$M\ddot{\eta} = F_I + F_D + F_S + F_B + K(\eta_{ct} - \eta) \quad (5.18)$$

where,

$$F_I = -\rho C_A V \ddot{\eta} + \rho V (1 + C_A) \dot{v} \quad (5.19)$$

$$F_D = \frac{1}{2} \rho C_D S (v - \dot{\eta}) |v - \dot{\eta}| \quad (5.20)$$

$$F_S = \frac{1}{2} \rho C_s A_p (\dot{\zeta} - \dot{\eta})^2 \quad (5.21)$$

$$F_B = \rho g A_w \zeta \quad (5.22)$$

$\rho$  = Density of sea water [ $Kg/m^3$ ]

$V$  = Displaced volume [ $m^3$ ]

$S$  = Projected area normal to force direction [ $m^2$ ]

$\dot{v}$  = Fluid particle acceleration [ $m/s^2$ ]

$\dot{\eta}$  = Vertical object velocity [ $m/s$ ]

$C_S$  = Slamming coefficient

$\zeta$  = Vertical wave elevation [ $m$ ]

$M$  = Lifted object mass [ $Kg$ ]

$g$  = Gravitational acceleration [ $m/s^2$ ]

$A$  = Added mass [ $Kg$ ]

$C_A$  = Added mass coefficient

$C_D$  = Drag coefficient

$v$  = Fluid particle velocity [ $m/s$ ]

$\eta$  = Vertical object motion [ $m$ ]

$\ddot{\eta}$  = Vertical object acceleration [ $m/s^2$ ]

$A_p$  = Horizontal projected area [ $m^2$ ]

$\dot{\zeta}$  = Vertical wave velocity [ $m/s$ ]

$K$  = Stiffness hoisting cable [ $N/m$ ]

$A_w$  = Object water plane area [ $m^2$ ]

$A_p$  = Projected area [ $m^2$ ]

$$(M + A)\ddot{\eta} + K\eta = F_I + F_D + F_S + F_B + K\eta_{ct} \quad (5.23)$$

Equation 5.23 can be used to solve vertical object motion  $\eta$ . The total line force is summarized by Equation 5.24, which is solved in each time step by numerical softwares.

$$F_{line,tot} = \underbrace{Mg + m(t)g - F_B(t)}_{\text{Static force}} + \underbrace{K(\eta_{ct} - \eta)}_{\text{Dynamic force}} \quad (5.24)$$

## 5.4 Hydrodynamic Forces

The hydrodynamic force contributions is calculated at time steps by the numerical software. Figure 5.3 shows a vessel hoisting an object through the splash zone, with the different parameters that determine the hydrodynamic forces.  $\eta_{ct}$  is the crane tip motion.  $\zeta$  and  $\dot{\zeta}$  is the wave elevation and velocity respectively.

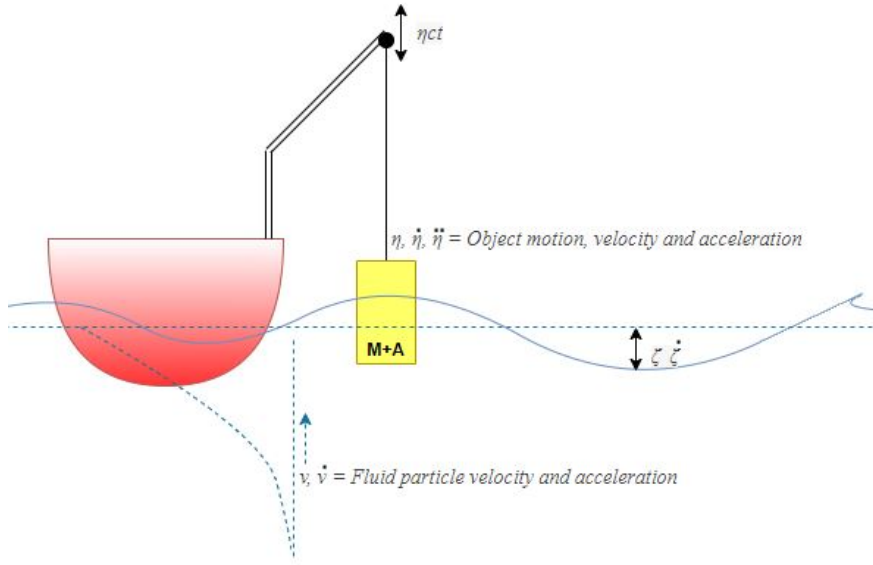


**Figure 5.3:** Parameters that determine the vertical forces in the hoisting wire.

### 5.4.1 Inertia Force

The inertia force  $F_I$  is one of the direct wave excitation forces from the Morison formula. This force is dependent on fluid-particle acceleration  $\dot{v}$  and lifted object acceleration  $\ddot{\eta}$ . This can be seen in Equation 5.25, where acceleration from the waves and object is multiplied with the mass and summed. The wave period is an important factor for the inertia force. Short wave periods with large wave amplitudes will have large vertical fluid acceleration  $\dot{v}$  with high energy, and thus induce large inertia forces. Added mass is in phase with the acceleration, the suction anchor has relatively large added mass and may result in large inertia forces through the splash zone. The inertia force can be written as in Equation 5.25.

$$F_I = \rho V \dot{v} + \rho V \dot{v} C_A - \rho V \ddot{\eta} C_A \quad (5.25)$$

$$F_I = \underbrace{\rho V}_{mass} \underbrace{(\dot{v} + \dot{v}C_A - \ddot{\eta}C_A)}_{acceleration} \quad (5.26)$$

### 5.4.2 Drag Force

The drag force, together with the inertia force, constitutes the Morison Equation. This force is the second direct wave excitation force. The drag force is dependent on the relative velocity between the water particles in the wave  $v$ , and the lifted object  $\dot{\eta}$ . This force will be present where the waves can energize the fluid particles. Depending on the wave size, this is mainly through the splash zone. Depending on the hoisting velocity, the drag force is also present during the object lowering.

The amplitude of the drag force is dependent on the projected area normal to force direction  $S$ . The drag coefficient  $C_D$  is usually found from *DNV-RP-H103: Modelling and Analysis of Marine Operations*. How the drag coefficient is implemented in SIMA is described in section 5.6.1.

$$F_D = \frac{1}{2} \rho C_D S (v - \dot{\eta}) |v - \dot{\eta}| \quad (5.27)$$

### 5.4.3 Slamming Force

The slamming force comes from the sudden change of added mass when an object is entering or leaving the splash zone. The added mass comes from the change of density of the surrounding fluid, and this change results in slamming forces. In other words, the slamming force is proportional to the change in added mass, and is dependent on the hoisting velocity  $v$ . This is illustrated in figure 5.4. The derivation of the slamming force is shown in Equation 5.28. It starts out differentiating Newton's second law with respect to time. Hoisting velocity  $v$  is time constant, which zeroes out this part. Added mass  $A$  is introduced when going through the splash zone and will, unlike mass  $M$ , change with time as the anchor is submerged.

The slamming force is only present when we have a change of added mass. This means that the slamming force will rise and peak when the maximum change in added mass is achieved i.e., through the splash zone. When there is no change in added mass, equation 5.29 gives zero slamming force.

$$F_S = \frac{d}{dt}(Mv) = \frac{dM}{dt} \cdot v + \frac{dv}{dt} \cdot m = \frac{d(M + A)}{dt} \cdot v = \frac{dA}{dt} \cdot v = \frac{dA}{dz} \frac{dz}{dt} \cdot v \quad (5.28)$$

$$F_S = \frac{dA}{dz} \cdot v^2 \quad (5.29)$$

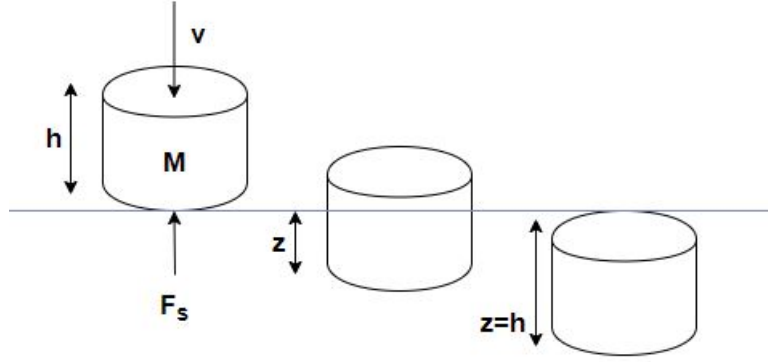


**Figure 5.4:** Slamming force proportional with change of added mass

In SIMA, the added mass is modeled with a depth-dependent coefficient and is suddenly increased when the anchor top is submerged. The slamming force is proportional to the velocity of the water particles squared, which gives reason to believe that this force is also more significant for smaller wave periods. If we have a substantial change in added mass at a given time in the simulation where a significant tension occurs in the outputted tension time series, this is likely a slamming impulse.

#### 5.4.4 Buoyancy Force

The buoyancy force  $F_B$  will be activated as soon as the object is in contact with the water. Variation in this force is due to change in the water surface elevation relative to the object. When the object is in the splash zone, the wave elevation will vary with time along the vertical axis of the object. The buoyancy force will thus be dependent on the wave elevation.

$$F_B = \rho g A_w \zeta \quad (5.30)$$

### 5.5 Crane Tip Motion

The crane tip motion is important to analyze, because it transmits the motions from the vessel directly to the lifted object through the crane wire. The crane tip will be located at an offset position from the vessel center of gravity and will therefore experience greater motions than the center of the vessel. According to Faltinsen (1990), the motions of any point on a rigid 6 DOF body can be found using Equation 5.31.  $i$ ,  $j$ , and  $k$  is the direction of motion in x, y and z direction respectively.

$$s = \eta_1 i + \eta_2 j + \eta_3 k + \omega \times r \quad (5.31)$$

$$\omega = \eta_4 i + \eta_5 j + \eta_6 k \quad (5.32)$$

$$r = xi + yj + zk \quad (5.33)$$

Here,  $\eta_1, \eta_2$  and  $\eta_3$  is the translations in x, y, and z.  $\eta_4, \eta_5$  and  $\eta_6$  is the rotations about the x,y and z axis. Inserting Equation 5.32 and 5.33 into 5.31 results in Equation 5.34. Here,  $s_1, s_2$  and  $s_3$  can be used to find the motion of a point in x, y and z direction respectively.  $s_3$  is used to analyse the vertical motion of the crane tip.

$$s = \underbrace{(\eta_1 + z\eta_5 - y\eta_6)}_{s_1} i + \underbrace{(\eta_2 - z\eta_4 + x\eta_6)}_{s_2} j + \underbrace{(\eta_3 + y\eta_4 - x\eta_5)}_{s_3} k \quad (5.34)$$

## 5.6 Hydrodynamic Parameters

Hydrodynamic parameters like drag and added mass are important parameters in lifting operation when estimating forces on the lifted object. Drag and added mass is implemented through coefficients in the numerical software. The added mass is implemented as a coefficient with the unit  $kg/m$  in three degrees of freedom (x,y, and z). The drag can either be implemented as quadratic or linear drag. Also, these are applied for three directions.

The drag and added mass coefficients must be found in order to model the forces correctly. The coefficients can be found either theoretically or experimentally. A common way is to use the standards of DNV GL to acquire the coefficients based on body shape and direction of motion. According to DNV-GL (2011b), the hydrodynamic coefficients are dependent on the proximity to the water surface and sea bottom, aspect ratio, projected angle towards water current, perforation ratio and surface roughness.

### 5.6.1 Drag Coefficient

The drag coefficient can be found either by experiments or from tables in DNV-GL (2011b). The drag coefficient is included to compensate for the resistance or *drag* of an object in a fluid flow. A higher drag coefficient ( $C_D$ ) gives a higher value of aerodynamic or hydrodynamic drag from the surrounding fluid.

The quadratic drag coefficient ( $K_D$ ) is implemented in SIMO in the unit  $\frac{Ns^2}{m^3}$ . The drag and added mass is inputted for three directions for each element, and calculated per meter length of the element. Thus the drag is divided by the element length  $L_E$  in Equation 5.36.

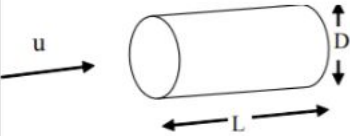
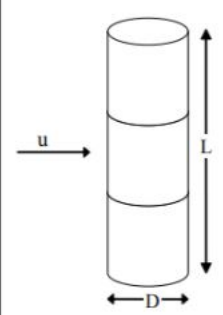
<b>Table B-2</b> Drag coefficient on three-dimensional objects for steady flow $C_{DS}$ . Drag force is defined as $F_D = \frac{1}{2}\rho C_{DS} S u^2$ . S = projected area normal to flow direction [m <sup>2</sup> ]. $R_e = uD/\nu$ = Reynolds number where D = characteristic dimension.				
Geometry	Dimensions	$C_{DS}$		
Circular cylinder. Axis parallel to flow. 	L/D			
	0	1.12		
	1	0.91		
	2	0.85		
	4	0.87		
	7	0.99		
		$R_e > 10^3$		
Circular cylinder normal to flow. 	L/D	Sub critical flow $R_e < 10^5$	Supercritical flow $R_e > 5 \cdot 10^5$	
	2	$\kappa$ 0.58	$\kappa$ 0.80	
	5	0.62	0.80	
	10	0.68	0.82	
	20	0.74	0.90	
	40	0.82	0.98	
	50	0.87	0.99	
	100	0.98	1.00	
	$C_{DS} = \kappa C_{DS}^\infty$			
	$\kappa$ is the reduction factor due to finite length. $C_{DS}^\infty$ is the 2D steady drag coefficient.			

Figure 5.5: Drag coefficients from DNV-GL (2011b).

$$F_D = \frac{1}{2} \rho C_D A_s v^2 \quad (5.35)$$

$$\frac{F_D}{L_E} = K_D v^2 \quad (5.36)$$

$$K_D = \frac{F_D}{L_E \cdot v^2} = \left[ \frac{Ns^2}{m^3} \right] \quad (5.37)$$

### 5.6.2 Added Mass

Added mass is the additional mass an object gets when the object is in motion, and the surrounding fluid is accelerated. Added mass is, in other words, the inertia added to the system because of the acceleration of the surrounding fluid caused by the object. The object ability to accelerate its surrounding fluid is dependent on the object shape. The added mass for simple structures can easily be estimated with added mass coefficients found in *DNV-RP-H103: Modelling and Analysis of Marine Operations*. The standard contains accurate coefficients for simple 2D and 3D compact bodies far away from boundaries such as the sea surface or seabed. The coefficients are fairly known for 2D porous plates, but problems arise with complex 3D structures (DNV-GL (2011b)).

The added mass of the deep penetration anchor is straight forward to estimate as its shape is close to a compact 3D cylinder with flukes on top. The suction anchor is a hollow steel cylinder closed at the top and receivable to water filling during the submergence. This means that as the anchor is submerged and filled with water, the potential added mass is drastically increased until the anchor top hits the sea surface where the weight of the entrapped water suddenly is part of the added mass. The large change of added mass is important because this results in large slamming forces.

On top of this, suction anchors have vent holes in the top plate for evacuating air during the submergence. The size and number of vent holes can vary, and decide the *perforation ratio*. The perforation ratio is given in a percentage of the total plate area and impact the added mass. With a large perforation ratio, the added mass will decrease drastically (Sandvik and Solaas (2017)).

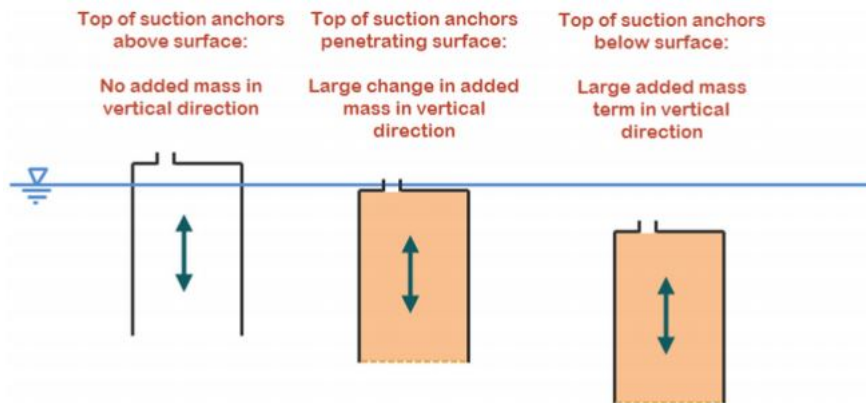


**Figure 5.6:** Change of vertical added mass for suction anchor (T.Næss et al. (2014)).

Figure 5.7 grants the basis for estimating vertical added mass for the anchors in this thesis. The vertical added mass for the DPA is estimated by that of a circular disc. Vertical added mass for the suction anchor is found from Equation 5.38. I.e., an added mass contribution from the disc added with the mass of the entrapped water. The decrease of added mass due to the perforation rate is subtracted based on information from experimental results. This is described in detail in Chapter 8.



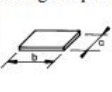

Table A-2 Analytical added mass coefficient for three-dimensional bodies in infinite fluid (far from boundaries). Added mass is $A_{ij} = \rho C_A V_R$ [kg] where $V_R$ [m <sup>3</sup> ] is reference volume							
Body shape		Direction of motion	$C_A$				$V_R$
Flat plates	Circular disc 	Vertical	$2/\pi$				$\frac{4}{3}\pi a^3$
	Elliptical disc 	Vertical	$b/a$	$C_A$	$b/a$	$C_A$	$\frac{\pi}{6} a^2 b$
	$\infty$		1.000	5.0	0.952		
	14.3		0.991	4.0	0.933		
	12.8		0.989	3.0	0.900		
10.0	0.984		2.0	0.826			
7.0	0.972	1.5	0.758				
6.0	0.964	1.0	0.637				
Rectangular plates 	Vertical	$b/a$	$C_A$	$b/a$	$C_A$	$\frac{\pi}{4} a^2 b$	
1.00		0.579	3.17	0.840			
1.25		0.642	4.00	0.872			
1.50		0.690	5.00	0.897			
1.59		0.704	6.25	0.917			
2.00		0.757	8.00	0.934			
2.50		0.801	10.00	0.947			
3.00		0.830	$\infty$	1.000			
Triangular plates 	Vertical	$\frac{1}{\pi} (\tan \theta)^{3/2}$				$\frac{a^3}{3}$	

Figure 5.7: Added mass coefficients ( $C_A$ ) (DNV-GL (2011b)).

$$A_{33} = \underbrace{\rho C_A V_R}_{disc} + \underbrace{\rho \pi R^2 h}_{water} \quad (5.38)$$

In Equation 5.38,  $\rho$  is the seawater density,  $C_A$  is the added mass coefficient,  $V_R$  is the reference volume,  $R$  is top plate radius and  $h$  is the anchor height.

Horizontal added mass properties for the anchors is found using Figure 5.8 from *DNV-RP-H103: Modelling and Analysis of Marine Operations*. The horizontal added mass coefficient is found based on the height/diameter ratio. For the suction anchor, the weight of the entrapped water must also be included to acquire the total horizontal added mass (Solaas (2020)).

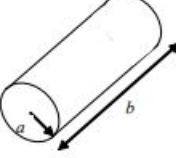
Table A-2 Analytical added mass coefficient for three-dimensional bodies in infinite fluid (far from boundaries). Added mass is $A_{ij} = \rho C_A V_R$ [kg] where $V_R$ [m <sup>3</sup> ] is reference volume (Continued)					
Body shape		Direction of motion	$C_A$		$V_R$
Right circular cylinder 	Vertical	$b/2a$	$C_A$		$\pi a^2 b$
		1.2	0.62		
		2.5	0.78		
		5.0	0.90		
		9.0	0.96		
		$\infty$	1.00		

Figure 5.8: Added mass coefficients ( $C_A$ ) from DNV-GL (2011b).



## Chapter 6

# Statistical Approach

The sea environment is random, and statistical models are beneficial when describing ocean waves or wind behavior. In this thesis, a statistical approach is used when locating design limits. The design limit is based on the Gumbel extreme value distributions where multiple extreme values are found, and a characteristic load is set. A characteristic load defines a load which will be exceeded with a pre-defined probability. When operating with statistical models, the accuracy dramatically depends on the available data. A large sample of the statistical process increases the accuracy of the statistical model.

The extreme values are found using SIMA (Chapter 7) and output the extreme maximum/minimum tension in the hoisting wire (extreme value) for each time series. The number of time series depends on the seed number, and thus the accuracy of the sample depends on the chosen number of seeds.

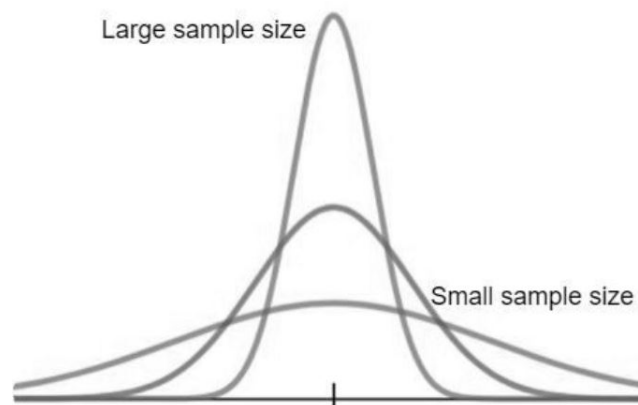


**Figure 6.1:** Increased sample size yields increased accuracy in the statistical distribution.

Multiple measurements of the statistical process make up the statistical sample. According to the central limit theorem, if the number of measurements is large, the distribution will approach the normal distribution (Leira (2019)). The normal distribution is also called the Gaussian distribution. A definition of a Gaussian process and its extreme distribution is shown in Figure 6.2. If one selects the peaks i.e., all the maximums from the up-crossings, the curve is offset to the right. The extreme values are the absolute largest (or smallest) value from each measurement, and the distribution will concentrate around the most probable extreme maximum. The extreme value distribution is described in section 6.1.

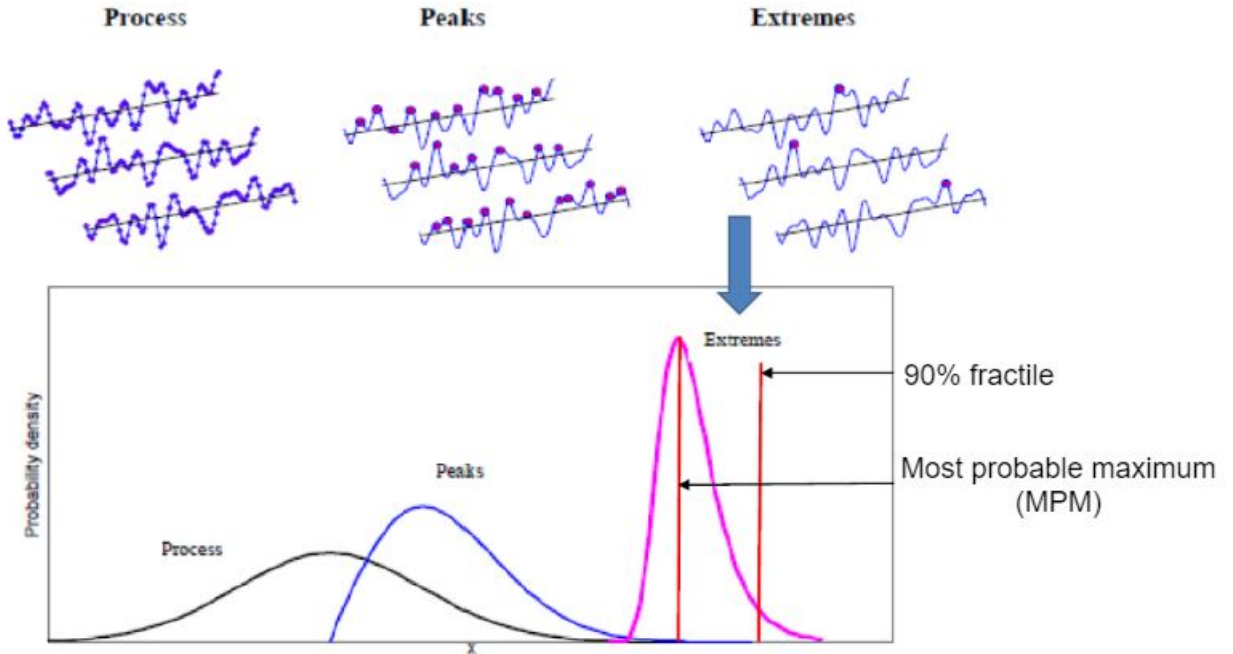


**Figure 6.2:** Definition of peaks (maximums) and extremes of the statistical sample (Larsen (2020)).

The term *fractile* is rapidly used throughout this chapter. The fractile is a value that states how much of the distribution lies below this value given as a percentage. The 90% fractile is shown in Figure 6.2. The 90% fractile gives an x-value, which with a probability of 90% will not be exceeded.

## 6.1 Gumbel Extreme Value Distribution

The Gumbel distribution is an extreme value distribution used to make the distribution of the extreme minima and maxima collected from statistical samples. The distribution applies to samples from natural phenomena and can be used to find, for example, the 100-year flooding of a river or rapidness of earthquakes.

In this thesis, the minimum and maximum tension in the crane wire is investigated to settle an operational limit for the anchor in terms of  $H_s$ . This can be done using the Gumbel extreme distribution. The results from a simulated  $H_s$  will consist of 15 different time series of crane wire tension. The extreme maximum and minimum are gathered from each time series using the Post Processor application in SIMA. The distribution of the extremes are plotted in MATLAB for assessment of the operational limit. The distributions are described in the following section.

### 6.1.1 Probability Density Function

The probability density function (*PDF*) is useful when studying statistical phenomena. The PDF of the extreme maximum and minimum will have different shapes. The PDF from the Gumbel distribution will have positive skewness for the maximum and negative skewness for the minimum. This is shown in figure 6.3 and 6.4, where the PDF is skewed to the right and left for the maxima and minima respectively. The Gumbel distribution contains two parameters, a scale ( $\beta$ ) and a location ( $\mu$ ) parameter. The  $\beta$  parameter (Equation 6.1) is identical for the maxima and minima and decides the spread of the distribution. In Equation 6.1,  $\sigma$  is the standard deviation of the sample.

$$\beta = \sigma \cdot \frac{\sqrt{6}}{\pi} \quad (6.1)$$

The second parameter is the location parameter  $\mu$ , which is also known as the most probable maximum or minimum *MPM*. The location parameter for the maximum can be calculated by Equation 6.2, where  $E[X_{max}]$  is the mean value of the extreme sample and  $\gamma$  is the Euler-Mascheroni constant set to 0.57721 (Leira (2019)). When the Gumbel parameters are identified, the probability density function and the cumulative distribution function can be plotted. In Equation 6.3  $z$  is equal to  $\frac{X_i - \mu_{max}}{\beta}$  where  $X_i$  is the extreme maxima from the sample (Leira (2019)). The PDF is calculated by Equation 6.3.

$$\mu_{max} = E[X_{max}] - \gamma\beta \quad (6.2)$$

$$f(X_{max}) = \frac{1}{\beta} \cdot \exp(-z + \exp(-z)) \quad (6.3)$$

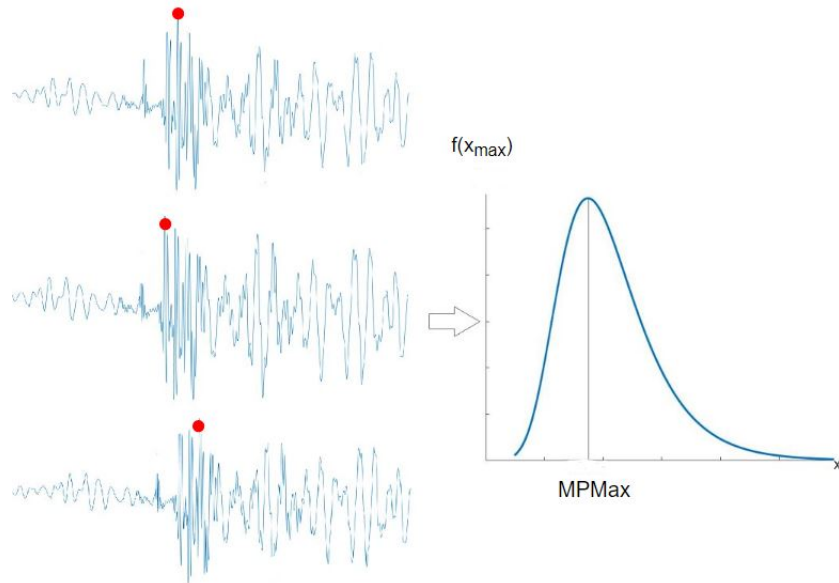


**Figure 6.3:** Gumbel PDF created from extreme maximum values from multiple measurements.

The PDF for the extreme minima is shown in Figure 6.4. The PDF is calculated by Equation 6.5 by use of the location parameter for the minima's  $\mu_{min}$ . Here  $z = \frac{x_i - \mu_{min}}{\beta}$  where  $x_i$  is the extreme minimum from the sample (Leira (2019)).

$$\mu_{min} = E[X_{min}] + 0.57722\beta \quad (6.4)$$

$$f(X_{min}) = \frac{1}{\beta} \cdot \exp(z - \exp(z)) \quad (6.5)$$

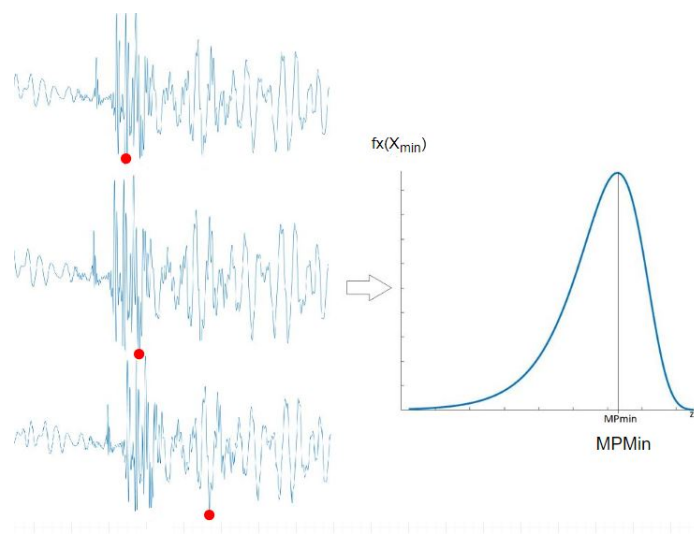


**Figure 6.4:** Gumbel PDF created from extreme minimum values from multiple measurements.

### 6.1.2 Cumulative Distribution Function

The cumulative distribution function (*CDF*) for the maxima and minima is expressed by equation 6.6 and 6.7 respectively.

$$F(X_{max}) = P(X \leq x_{max}) = \exp(-\exp(-z)) \quad (6.6)$$

$$F(X_{min}) = P(X \leq x_{min}) = 1 - \exp(-\exp(z)) \quad (6.7)$$

The CDF returns the probability of  $X$  being smaller or equal to some value  $x$ . It is useful when wanting to locate a probability of occurrence for a given  $x$ -value. In Figure 6.5 a CDF for extreme max crane wire tension for  $H_s = 1m$  is shown. By using the plot or Equation 6.6, the probability of getting e.g. wire tension less than 1870kN is found to be 0.9 or 90%.

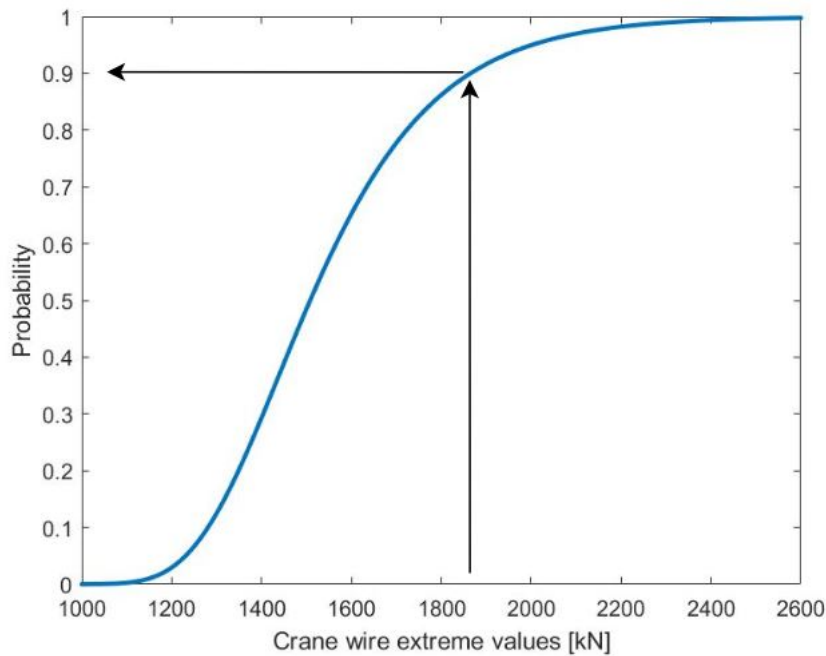


**Figure 6.5:** Example of Gumbel cumulative distribution function.

Alternatively, if wanting to find an  $x$ -value for a given probability, we introduce the quantile function sometimes called the inverse cumulative distribution function (Leira (2019)). These functions are useful when operating with fractiles. The  $x$ -value (crane tension) can be found by using Equation 6.8 and 6.9 for the maxima and minima samples respectively. Figure 6.6 shows graphically how the quantile functions work.

$$X_{max}(P) = \mu - \beta \ln[-\ln(P)] \quad (6.8)$$

$$X_{min}(P) = \mu + \beta \ln[-\ln(1 - P)] \quad (6.9)$$

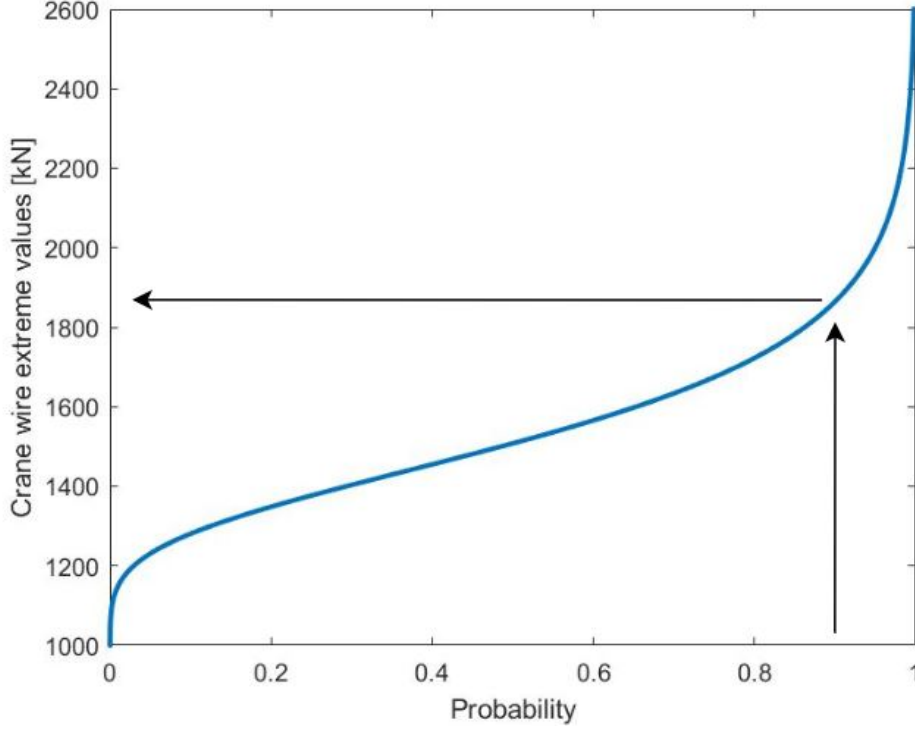


**Figure 6.6:** Example of inverse cumulative distribution function.

### 6.1.3 Gumbel Plot

A Gumbel plot can be used to make two linear plots for comparison to make sure that the data set fits the Gumbel distribution. The values from the sample is plotted as the right side of equations 6.10 and 6.11. Where the two equations represent maximum and minimum, respectively. The left side is plotted from the sample *size*, where P is equal to  $\frac{k}{n+1}$ . where  $k = \{1, 2, 3, \dots, n\}$  and  $n$  is the total number of data in the sample.

$$-\ln[-\ln(P)] = \frac{X_{max} - \mu}{\beta} \quad (6.10)$$

$$-\ln[-\ln(1 - P)] = -\frac{X_{min} - \mu}{\beta} \quad (6.11)$$

The linear fit in Figure 6.7 is plotted with the help of the Polynomial curve fitting function in MATLAB. The linear fit is meant to visualize the linearity of the empirical distribution scatter plots and compare the results with the sample's distribution. Figure 6.7 shows the two linear curves are close to similar, and therefore there is reason to believe that the data set fits the Gumbel distribution.

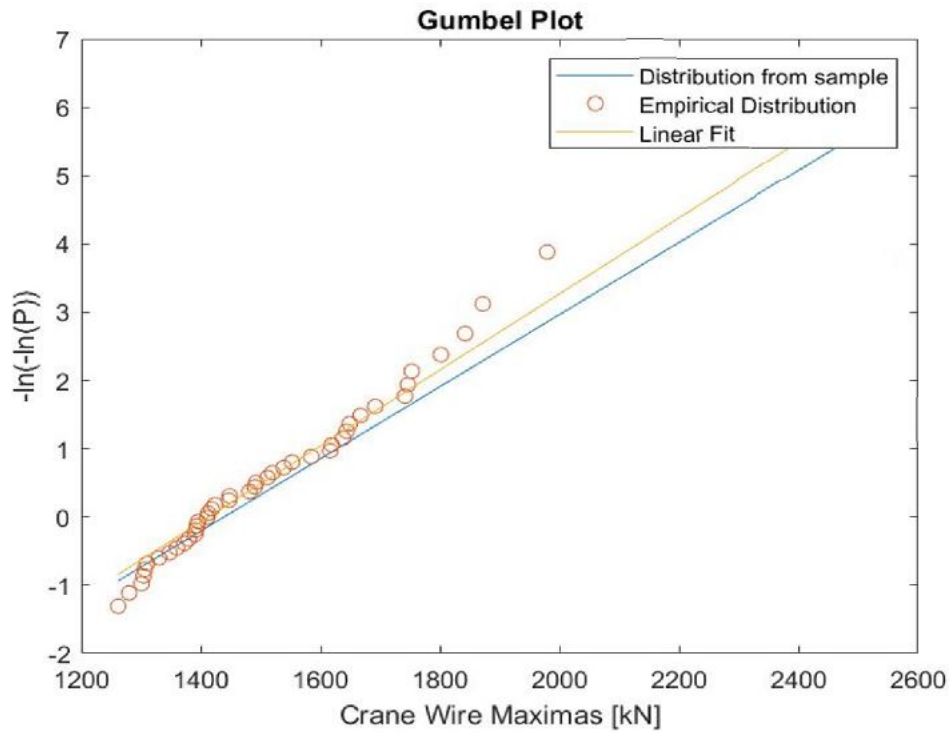


**Figure 6.7:** Example of Gumbel plot from a extreme maximum sample.

## 6.2 Exceedance Probabilities

When analyzing statistical phenomenons, exceedance probabilities are used. Exceedance probabilities is the probability of reaching a certain value and is useful to find trends and more information about the statistical sample. The exceedance probabilities are denoted as a  $P$  followed with the given probability. As an example, the P90 value will be exceeded by a probability of 10% (Figure 6.8). In this thesis, the exceedance probability is useful for analyzing crane wire tension thresholds, wave period for a specific wave height, and operation duration estimation.

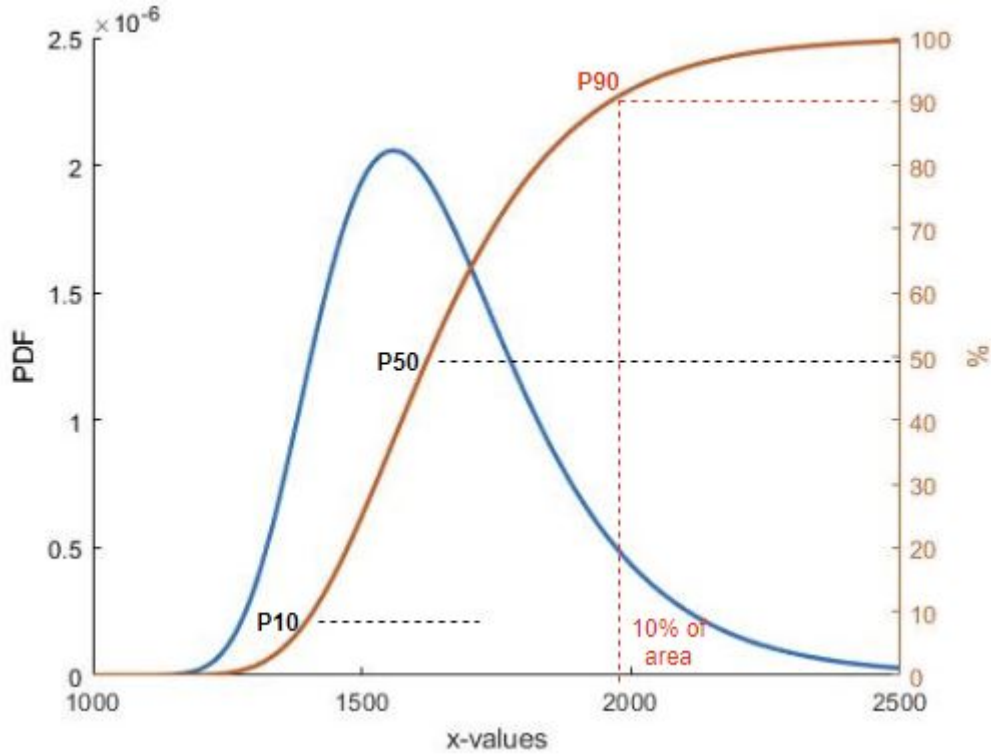


Figure 6.8: Definition of P90, P50 and P10 probabilities.

### 6.2.1 Design Criteria Based on Crane Wire Tension

When locating the significant wave height design criteria based on crane wire tension, two different factors are assessed: the slack criterion and design strength of the crane wire. According to DNV-GL (2011b), large snap loads might occur with slack in the hoisting wire. It is, therefore, a requirement that the hydrodynamic force shall not exceed 90% of the total submerged weight of the object. This slack requirement results in a specific minimum allowable crane wire tension.

The second requirement defines the upper limit in terms of crane wire tension. The crane wire will have a pre-defined design strength that should not be exceeded with a certain probability. The upper limit can be chosen based on the MPM or a 90% fractile (Larsen (2020)). The P90 value will be a more conservative approach compared to the MPM as the MPM will be a lower extreme value than given by the 90% fractile (Figure 6.2).

A comparison of the extreme value distribution of the maxima and minima is shown in Figure 6.9. Here one  $H_s$  simulation is performed, and the maximum and minimum extreme value distributions are plotted. The 10% fractile must indicate a value above the slack criterion on the x-axis. For the maximum distribution, the 90% fractile must indicate an x-value lower than the design strength of the crane wire. If the sea condition satisfies both requirements, the sea condition can be increased and analyzed again. This is done until the requirements are violated.



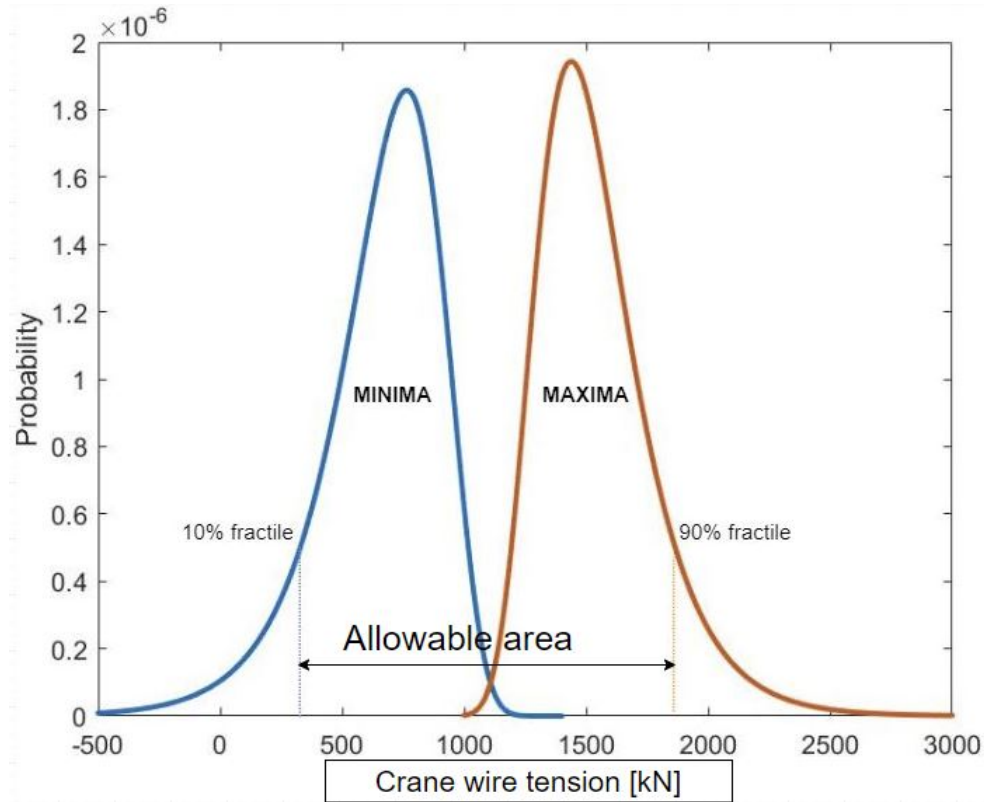


**Figure 6.9:** 10% fractile of minima must be above the slack criteria and 90% fractile of maxima must be below wire design strength.

### 6.3 Weibull Distribution

The Weibull model is frequently applied for empirical samples (Leira (2019)). In this thesis, the Weibull distribution is used to plot the PDF and CDF of the total measured  $H_s$  from the Tampen area in the time interval stretching from 1957-2019. MATLAB's built-in function *wblpdf* and *wblcdf* is used to plot the PDF and CDF respectively (MathWorks (2020)). This is done because the Weibull model is not directly used to gather any results for the operational limit study, only getting an insight and validating the given sample of  $H_s$ . The theory behind the Weibull model is not included in this thesis.

The fit of the Weibull distribution to the measured sample of  $H_s$  is done by a Weibull probability plot. This is done through the *wblplot* function in MATLAB. The function plots the data points as a blue plus sign ('+') and draws the reference line that is the theoretical distribution (Figure 6.10). If the sample fit the Weibull distribution, the data points are located along the reference line. The Weibull probability plot may often result in a concave or convex curve. This may be a result of a few or inadequate number of measurements in the lower or upper tail (Leira (2019)).

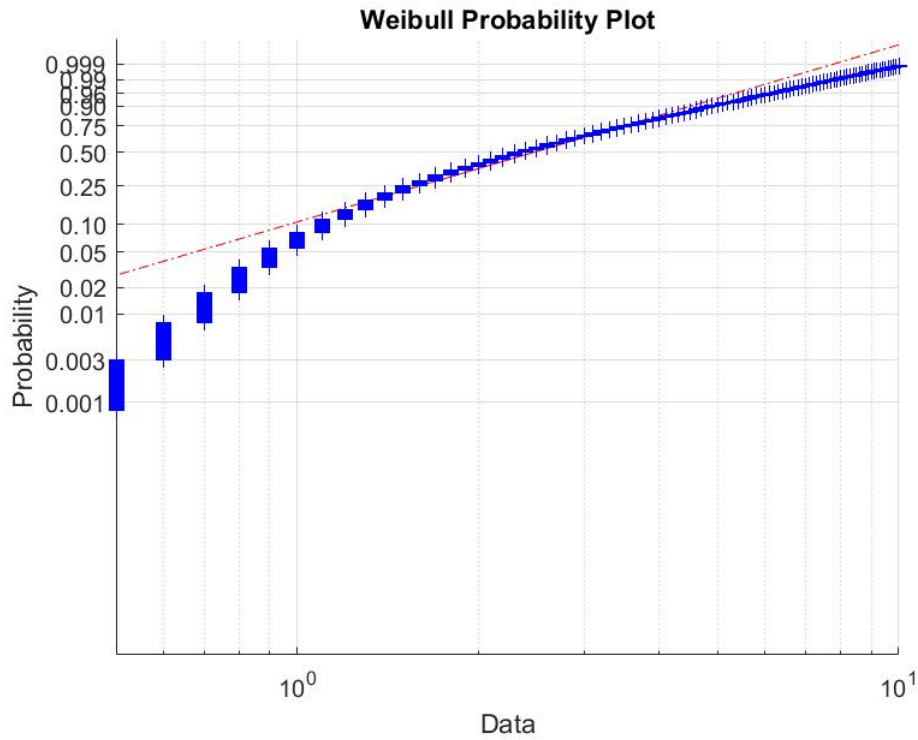


**Figure 6.10:** Weibull probability plot for sample of measured  $H_s$ .

The  $H_s$  sample consists of values with only one decimal; this results in the concentrated data points along the x-axis. Most data points are measured in the region from approximately 1.5m to 5m. This is visualized in Figure 6.10, where this is the area where the data points concentrate strictly around the reference line. This gives reason to believe that the  $H_s$  sample follows the Weibull distribution.

## Chapter 7

# Simulation Software

SINTEF Ocean develops the SIMA Software for simulating marine operations and floating systems. In general, SIMA is a simulation workbench for marine operations and is used to study station keeping motions and loads of floating bodies. The numerical calculations done in SIMA is done by a different and older software called SIMO. These two systems work together for a good user interface. Among the essential features of the SIMO software are flexible modeling of systems (slender and/or fixed body elements), realistic modeling of environmental conditions like wind waves and current, and the simultaneous nonlinear time-domain solutions of both low-frequency forces and wave frequencies (SINTEF Ocean (2019b)). The software is designed for easy use and holds a good user interface. This makes it an excellent tool for both experts and beginners.

SIMA provides the benefit of having graphical representation in 3D of the simulated operation. This is helpful when creating the model and especially as the complexity of the model increase. SIMA can be used throughout the whole operation from start to finish. This includes defining a sea environment, body modeling, implementing hydrodynamic parameters, simulating, and post-processing the results.

## 7.1 Time Domain Analysis

SIMO uses the time domain solution and solves the equation of motion for different time steps. Complex models with irregular sea use the time domain solution to output response because of the non-linear effects present. This method is time-consuming if done manually. The outputted response is based on small time steps to be accurate, and the method is well suited for numerical software. In SIMO, the model consists of different simplified bodies that together constitute a full model. The motions and loads of the coupled system are solved simultaneously (SINTEF Ocean (2019a)).

## 7.2 Distributed element force

In SIMO, the distributed element force model can be used on two different element types: fixed and slender element. The slender element is used for long objects like a spar buoy, jacket legs, or the vertical cylinder walls of an anchor. Fixed elements can be used as fixed connection points in between e.g., spool pieces but is not relevant in this thesis. More information about concentrated, fixed elements can be found in SINTEF Ocean (2019a).

The anchors are modeled in a simplified way as multiple slender elements with different lengths. The slender elements are divided into strips with equal length. A summation can then estimate the resulting hydrodynamic force from all strips (Greco ((2019))). One single element strip is subjected to external loads from three different contributions: buoyancy force ( $F_B$ ) wave force ( $F_W$ ) and slamming force ( $F_S$ ). When working with slender elements in SIMO, three different coordinate systems are used: global coordinate system ( $X_G$ ), local body-fixed coordinate system ( $X_B$ ), and local strip coordinate system ( $X_S$ ). The strip coordinate system can be seen in figure 7.1. For a slender element, the x-axis will always be the longitudinal element direction.

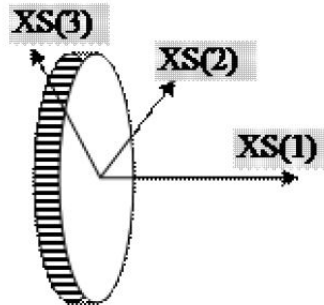


**Figure 7.1:** Local strip coordinate system (SINTEF Ocean (2019a))

The gravity and buoyancy force acts in the global z-direction, and can be calculated from equation 7.1 and 7.2 respectively.  $F_B$  acts through the center of buoyancy.

$$F_{G,G} = \begin{bmatrix} 0 \\ 0 \\ -mgdS \end{bmatrix} \quad (7.1)$$

$$F_{B,G} = \begin{bmatrix} 0 \\ 0 \\ -\rho V_s g d S \end{bmatrix} \quad (7.2)$$

The wave force (Equation 7.3), also acts through the center of buoyancy but expressed in the local strip coordinate system. Here, the first term is the diffraction and Froude-Krylov force. The second and the last term is the quadratic and linear drag respectively.

$$F_{W,S} = \rho V_s a_s + m_h \circ a_s + C_q \circ \{(U_s + v_s - \dot{X}_s) \circ |U_s + v_s - \dot{X}_s|\} + C_l \circ (U_s + v_s - \dot{X}_s) \quad (7.3)$$

$\circ$  = Element wise multiplication

$\rho$  = Density of seawater

$m_h$  = Hydrodynamic mass

$V_s$  = Submerged volume per length unit

$v_s$  = Water particle velocity in local strip coordinate system in x,y, and z direction

$a_s$  = Water particle acceleration in local strip coordinate system in x,y, and z direction

$\dot{X}_s$  = Strip velocity components in local strip coordinate system

$U_s$  = Current velocity in local strip coordinate system

$C_q$  = Quadratic drag

$C_l$  = Linear drag

The slamming force on a moving strip is proportional to the change in vertical added mass (Equation 7.4), and thus is found in a local coordinate system (SINTEF Ocean (2019a)). In Equation 7.4  $m_s$  is the strip mass.

$$F_{S,s} = -\frac{\partial m_s}{\partial t} \dot{X}_s \quad (7.4)$$

### 7.3 Post processor application

The post-processor application in SIMA is used to gather extreme values from the total crane wire tension. A window filter is created in the post processor, making it possible to define a time interval in the time series for the gathering of extreme values. The time window must be set to contain the full lifting operation, excluding high tension dynamics in the equilibrium phase due to transient effects. The post-processor also contains a statistics toolbox that, with a signal input, outputs extreme maximum and minimum. If we now run a condition set with several simulations, it outputs the extreme maximum and minimum total crane tension from each simulation (or time window intervals).

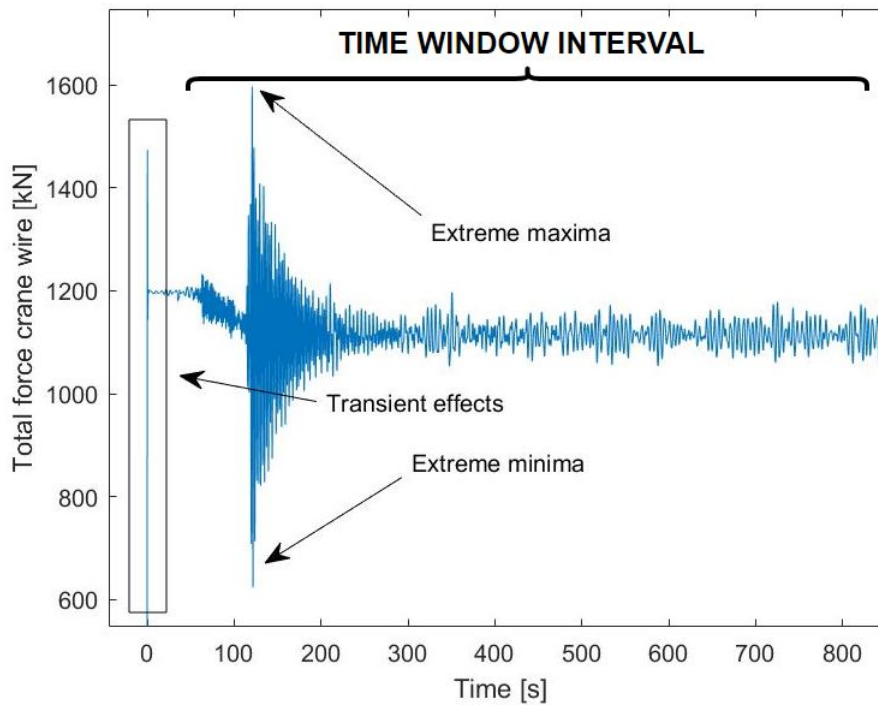


**Figure 7.2:** Extreme value taken from time window interval.

## Chapter 8

# The Simulation Model

### 8.1 Installation Vessel

The vessel model used in the simulation is given by supervisor and is the 157-meter long Skandi Acergy. This is a ROV construction vessel well suited to perform subsea installations and marine operations. The vessel is flexible in work tasks and can handle objects of different shapes at varying water depths and environmental conditions (DOF (2013)). The vessel is implemented in SIMA with its kinetics which include its hydrodynamic properties and damping. Dynamic positioning (DP) system is a system to maintain the vessel position with thrusters and propellers during offshore operations. The DP system is difficult to model in SIMA, and therefore the vessel is moored with a horizontal system consisting of four lines. The anchoring system has the same stiffness and damping as a DP system to simulate the effect of the DP.

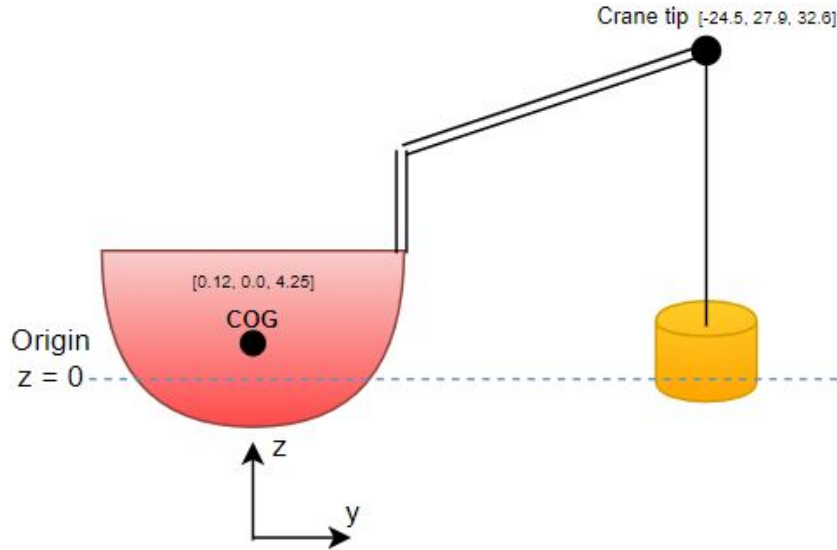


**Figure 8.1:** Skandi Acergy (Skipsrevyen (2018))

**Table 8.1:** Skandi Acergy vessel data

Built	2008
LPP	137.7m
Breadth	27m
Draught	8.5m
DWT	11 558 t

The vessel coordinate system is located at origo in all directions, where the water surface is defined at  $z=0$ . The vessel centre of gravity is located at  $x=0.1221\text{m}$ ,  $y=0.0\text{m}$  and  $z=4.25\text{m}$  as seen in Figure 8.2. The x-axis stretches along the longitudinal direction of the vessel positive forward. The vessel mass coefficients i.e. total mass and moments of inertia are found in Table 8.2.

**Figure 8.2:** Global coordinate system, vessel centre of gravity and crane tip location.**Table 8.2:** Mass coefficients for vessel in SIMA

Mass [kg]	Ixx [ $kgm^2$ ]	Iyx [ $kgm^2$ ]	Iyy [ $kgm^2$ ]	Izx [ $kgm^2$ ]	Izy [ $kgm^2$ ]	Izz [ $kgm^2$ ]
1.69e+07	1.93e+09	0.0	2.35e+10	8.78e+06	0.0	2.31e+10

The crane tip is a body point on the vessel body, meaning that its coordinates is given from the reference coordinate system of the vessel. The crane tip is given the coordinates  $x=-24.5$   $y=27.9$  and  $z=32.6$ , all coordinates are given in meters. The large weight of the anchors (110 tons) results in a large roll moment about the x-axis of the vessel. This is a disturbance in the initial phase of the lift when stabilizing the anchors in air prior to the lowering. This is solved by applying a specified force with equal magnitude to the anchor located on the opposite side of the vessel.



### 8.1.1 First Order Motion Transfer Functions

First order motion transfer functions (RAO's) is included in the vessel body. The RAO's are given for six degrees of freedom and dependent on wave direction. The vessel six degrees of freedom is shown in Figure 8.3. The vessel is symmetric about the x-axis meaning that RAO from  $0^\circ$  to  $180^\circ$  is identical to  $180^\circ$  to  $360^\circ$ .  $180^\circ$  wave direction corresponds to direct *head sea* hitting the bow of the vessel,  $90^\circ$  direction is coming in starboard also called *beam sea*. The six degrees of freedom consist of three translations and three rotations. The translational motions are surge, sway and heave. The rotational motions are roll, pitch and yaw.

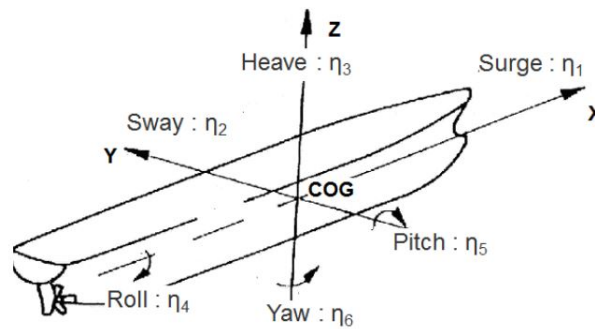


Figure 8.3: Vessel degrees of freedom (Larsen (2019a)).

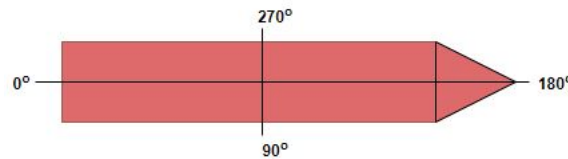


Figure 8.4: Wave direction definitions, vessel seen from above.

During a crane operation, vessel responses in all directions is important to assess. Horizontal motions may result in the lifted object crashing into the vessel side. In this section, the vessel RAO's that is important for vertical motions in the crane tip is prioritized. This will be the heave, roll and pitch RAO's. The vessel headings of interest is the  $180^\circ$ ,  $160^\circ$  and  $135^\circ$  directions. This is because the best vessel heading in terms of finding the highest operation limit is unknown, and therefore these headings is analyzed in the simulations. RAO's for sway, yaw and surge is included in Appendix A.

Heave is the translational motion in vertical z-direction. Figure 8.5 shows clearly the importance of vessel heading to minimize response when performing a offshore operation. Beam sea results in a significant response around 7-8 second wave periods. The response is decreasing with increased vessel heading towards head sea. The vessel eigen period in heave is located in the interval from 6-8 seconds for the relevant wave directions (red and green).

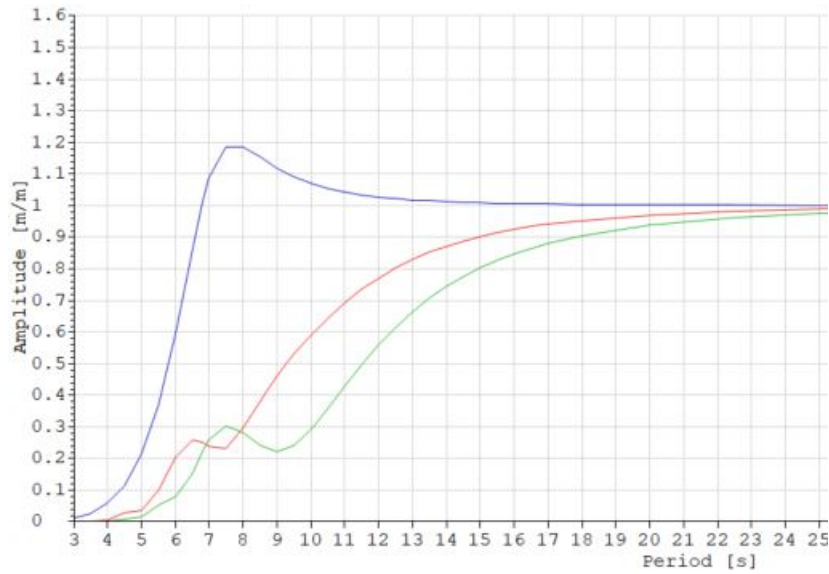


Figure 8.5: Heave RAO: blue=90° red=135° green=180°.

Roll motion is the vessel rotation about the x-axis and is an important parameter in the vessel stability. Figure 8.6 shows the RAO for the vessel roll motion. The vessel gets a significant response at peak period around 14.5 seconds. Here the response is 11.5 degrees per meter for beam sea and this is assumed that the vessel get resonance in roll for this wave period. For increased vessel headings the curve has a similar shape and about the same peak period. Large roll motions results in large motions in heave and sway direction for the lifted object.

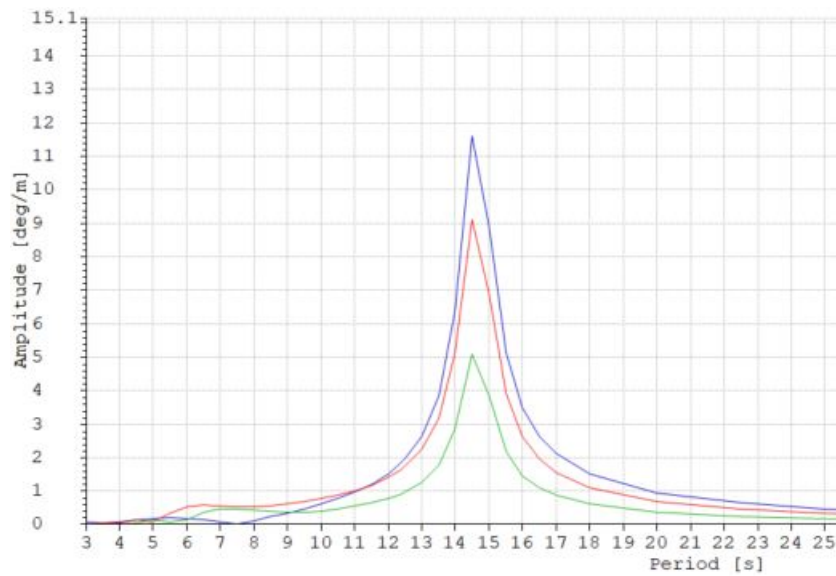
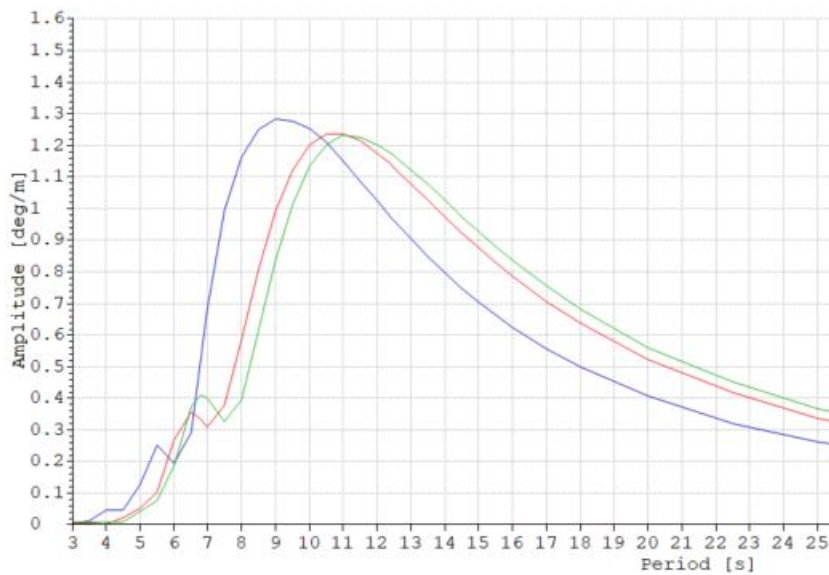


Figure 8.6: Roll RAO: blue=90° red=135° green=158°

The pitch RAO can be seen in Figure 8.7. Pitch motion is the vessel rotation about the y-axis and measured in degrees per meter. As the crane tip is located some distance

away from the vessel center of gravity in the x-direction, the lifted object may experience large heave and surge motions by large pitch motions of the vessel. The pitch motion is important because of the desired wave directions during a crane operations is usually in the area of head sea. Head sea waves will induce large pitch response if the wave period is in the area of 9-11 seconds.



**Figure 8.7:** Pitch RAO: blue=135° red=158° green=180°.

## 8.2 Lifting Equipment

The lifting equipment in the model consists of slings, the hook and the crane wire. The slings and the crane wire consist of the same type of wire and share the same characteristics. The crane block has an estimated mass of 12,000 kg, which contributes to a correspondingly increased total mass on the lift. In the simulations, two lifts are performed: a suction anchor lift, where three slings with an angle are used as rigging; and a lift of a torpedo anchor with a sling attached at the disconnection point located at the anchor top.

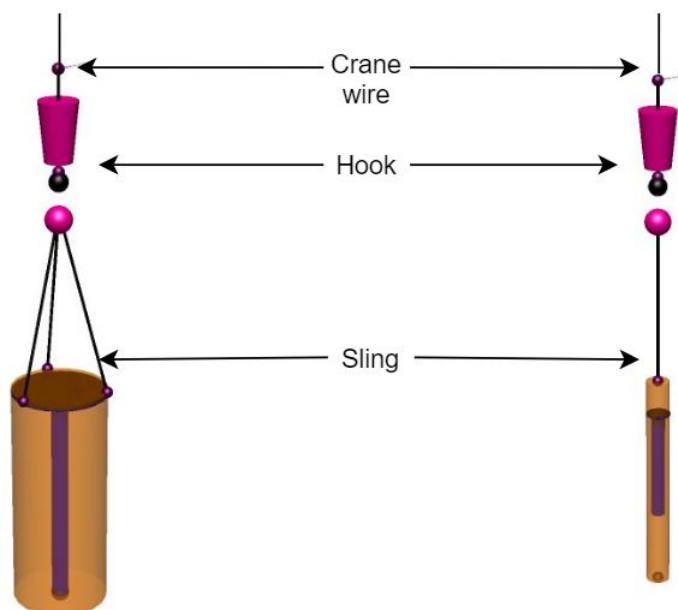


**Figure 8.8:** Lifting equipment for suction anchor (left) and deep penetration anchor (right).

### 8.2.1 Hook

Couplings are used to connect the slings and crane wire to different points in the model. The crane wire is coupled to the vessel through the crane tip ( $x=-24.5$   $y=27.9$  and  $z=32.6$ ) and the hook top. Further the slings are coupled to the hook bottom and down to the anchor body point(s). The hook mass coefficients are given in Table 8.3.

**Table 8.3:** Mass coefficients for hook in SIMA.

Mass [kg]	$I_{xx}$ [ $kgm^2$ ]	$I_{yx}$ [ $kgm^2$ ]	$I_{yy}$ [ $kgm^2$ ]	$I_{zx}$ [ $kgm^2$ ]	$I_{zy}$ [ $kgm^2$ ]	$I_{zz}$ [ $kgm^2$ ]
12 000	48 000	0.0	48 000	0.0	0.0	24 000

The hook is modelled with a main body given the initial coordinates  $x=-24.5$ ,  $y=27.9$  and  $z=27.1$ . The hoisting wire and the slings are connected to the hook body through two body points located on the top and bottom of the hook (Figure 8.9). The hoisting wire is connected to the top body point given in the hook local coordinate system at  $x=0$ ,  $y=0$  and  $z=0.5$ . The slings are coupled to the bottom point with identical  $x$  and  $y$  coordinates as the aforementioned, but  $z$  equal to  $-1.5$ .

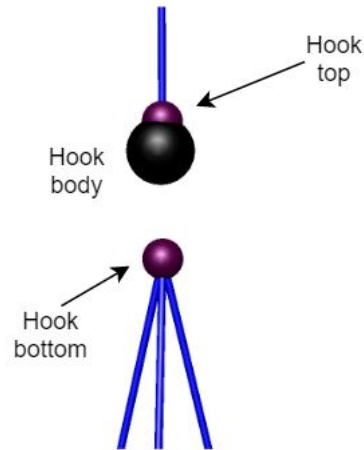


**Figure 8.9:** Hook body points in SIMA

### 8.2.2 Crane wire and slings

The choice of hoisting wire characteristics is based on Bridon-Bekaert (2020). Galvanized steel wire ropes are recommended, and with a minimum tensile grade of 1-960  $N/mm^2$  (DNV-GL (2016b)). The hoisting wire characteristics decide how high the allowable total crane force can be. The *minimum breaking force* or sometimes referred to as *minimum breaking load (MBL)* of the hoisting wire, is an important parameter that states how much force the wire can be designed for. Together with a safety factor, the design tension for the wire can be found. The safety factor shall not be less than 3 (DNV-GL (2016b)). The wire characteristics are found in Table 8.4. The material damping is assumed to be 1% of the axial stiffness (SINTEF Ocean (2019b)). In this thesis, the characteristics apply to both the slings and the hoisting wire, although these are often not completely identical.

**Table 8.4:** Wire characteristics.

Diameter	Weight		Minimum breaking force		Axial stiffness	Cross section	Material Damping
	In air	Submerged	1960 grade				
<i>mm</i>	<i>kg/m</i>	<i>kg/m</i>	<i>kN</i>	<i>Tonnes</i>	<i>N</i>	<i>mm<sup>2</sup></i>	<i>Ns</i>
84	30.6	26.5	5821	593	$3.67 \cdot 10^8$	3491	$3.67 \cdot 10^6$

For the suction anchor lift, three slings are used. Each sling is coupled to the hook and down to three body points located on the top of the suction anchor. The slings are given a length equal to 9.77m which results in a  $75^\circ$  sling angle (Figure 8.10). The three anchor body points are located so that they are equally spread around the circumference of the anchor top. The DPA anchor have one 10m sling connected to a single body point on the top of the anchor.

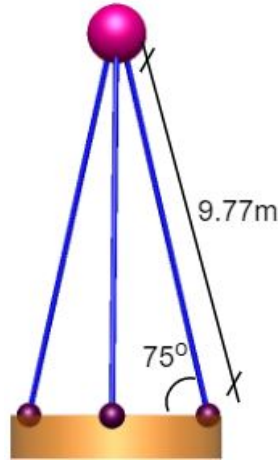


**Figure 8.10:** Sling angle and length for suction anchor rigging.

### 8.3 Suction Anchor Model

A suction anchor (SA) has complex hydrodynamic properties due to the void inside the anchor, which is gradually filled with water through the splash zone. This makes the modeling method essential to make a realistic model that considers all the factors rightly. The suction anchor model in this thesis consists of three slender elements. Each element has a specific task in the quest to simulate the behavior of the suction anchor in water.

A suction anchor consists of a top plate and cylindrical walls stretching down as an upside-down cup. The top plate includes a hatch or several hatches that results in a perforation ratio. In this thesis, the perforation ratio is set to 6%, minimizing the vertical added mass by 10% (Solaas (2020)). The anchor is modelled using three slender elements (SE), as shown in Figure 8.11. Anchor weight and dimensions are determined from the anchor's operational purpose, i.e., for a floating wind farm. The final anchor properties can be found in Table 8.5.

The suction anchor body is modelled as a 6 DOF time domain type. The anchor body is given a local body coordinate system, where origo is located at  $x=-24.5$ ,  $y=27.9$  and  $z=4.3$ . The slender elements are given coordinates based on the local body coordinate system. The element distribution is inspired by Solaas (2020).

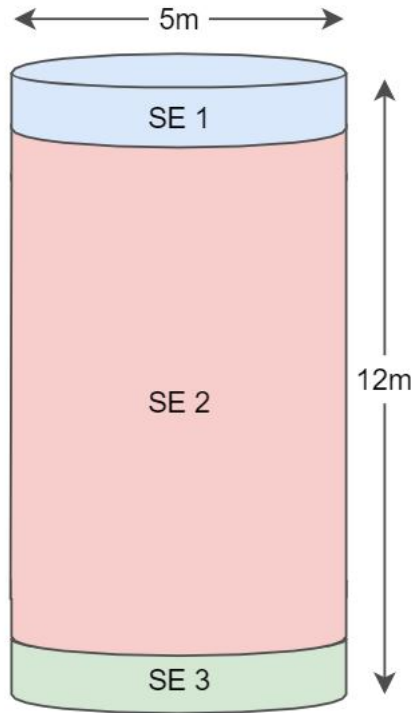


**Figure 8.11:** Suction anchor with highlighted slender elements.

**Table 8.5:** Suction Anchor properties.

Diameter [m]	Height [m]	Thickness [m]	Perforation Ratio [%]	Mass [Kg]
5	12	0.035	6	110 000

### 8.3.1 Anchor top element

The slender first element (SE 1) represents the top plate of the suction anchor. This element includes the added mass due to the water above the anchor and drag around the top edges. The added mass is calculated from Figure 5.7 as a circular disc. The element is given a length equal to the plate thickness of 0.035 m, hence the element will have negligible horizontal hydrodynamic contribution. The cross-section is found from  $\pi R^2$ . The hydrodynamic properties of the element can be found in Section 8.3.4.

According to T.Næss et al. (2014), full added mass for suction anchors is achieved when the anchor is submerged approximately one anchor diameter below the sea surface (Figure 8.12). To model this effect, a depth dependency tool is used for the added mass. SIMO provides the ability to apply a relative added mass for increasing the vertical position of the element. When the anchor is submerged approximately 5 meters, the relative horizontal element added mass is set equal to 1. The depth-dependent increase in added mass is implemented, as in Figure 8.12.

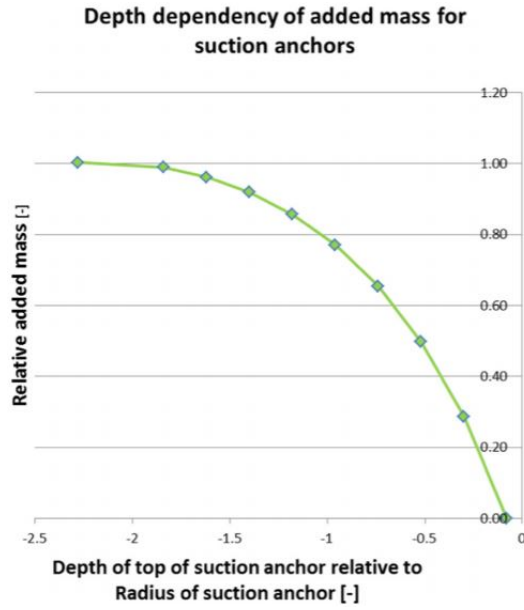


**Figure 8.12:** Depth dependent added mass for suction anchors (T.Næss et al. (2014)).

**Table 8.6:** Suction anchor top plate element (SE 1) properties.

Length [m]	Cross-section area [ $m^2$ ]	Volume [ $m^3$ ]	Number of strips
0.035	19.6	0.687	1

### 8.3.2 Anchor Wall element

Slender element 2 (SE 2) represents the cylindrical walls of the suction anchor. This element is given a length equal to 12 meters, and a cross section from a hollow cylinder like in Figure 8.13. The main task of SE 2 is to represent horizontal drag and added mass. The vertical added mass from water filling is delegated to SE 3. The cross section area is calculated with an assumed thickness of 0.035m.



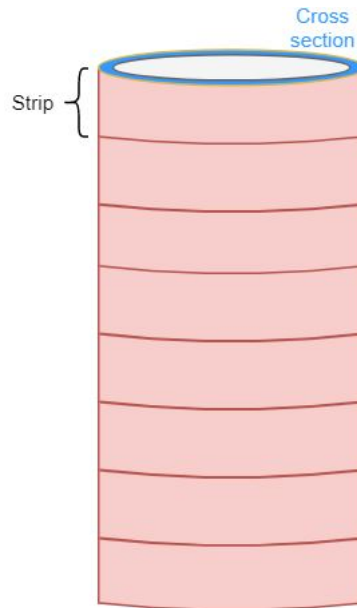


**Figure 8.13:** Suction anchor wall element with strips.

**Table 8.7:** Anchor wall element properties.

Length [m]	Cross-section area [ $m^2$ ]	Volume [ $m^3$ ]	Number of strips
12	0.546	6.6	8

### 8.3.3 Entrapped water element

The third element (SE 3) is included to consider the entrapped water inside the suction anchor caisson. The element is not given any cross-section or volume, only a length equal to 0.1m. The entrapped water will make a significant contribution in the vertical added mass when the water level reaches the top inside the anchor. Therefore this element is given a depth-dependent added mass, which reaches its maximum when the anchor is fully submerged. The vertical drag is also implemented as depth-dependent and fully achieved when anchor is submerged.

### 8.3.4 Vertical added mass and damping

The vertical added mass and damping for the suction anchor is found from a combination of hand calculations and experimental results. In an experiment performed by Sandvik and Solaas (2017), added mass and damping is found for suction anchors with different diameter/height ratio and perforation ratio.

This experiment is used when estimating the vertical damping and the reduction in added mass due to the perforation ratio. The experiment is used because of the complex hydrodynamic properties of the SA. This is due to the perforation ratio and the entrapped water. In the experiment, added mass and damping is found from the motion decay method for the different anchors, where the anchor is suspended in a spring and

released from an offset position. The anchor chosen from the experimental results has the same diameter as the anchor in this thesis (5m) but is slightly shorter (10m). However, based on studying the different anchors' results, it is assumed that the anchors will have approximately similar vertical damping coefficients due to the small difference in length but identical diameter.

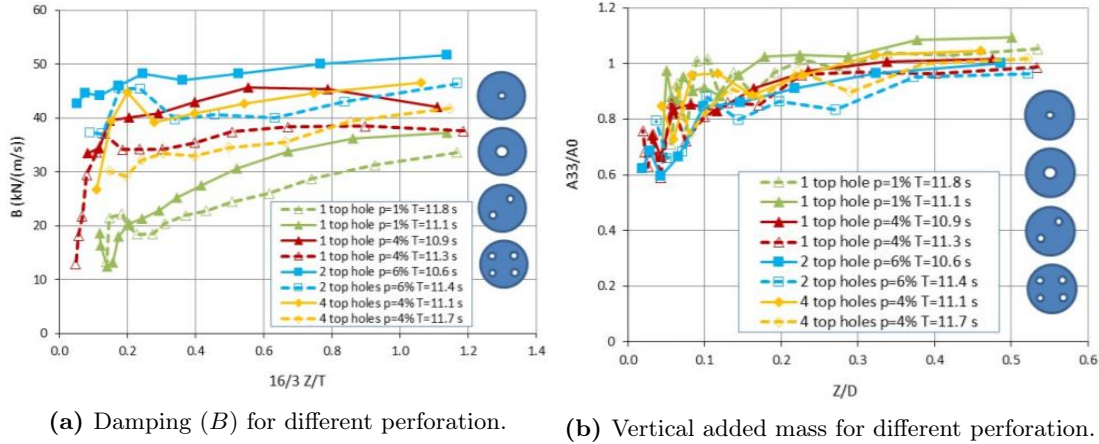


**Figure 8.14:** Experimental results by Sandvik and Solaas (2017).  $T$  is the oscillation period,  $Z$  is the oscillation amplitude and  $D$  is the anchor diameter.  $A_{33}$  and  $A_0$  is the vertical added mass for a perforated and a non perforated SA respectively.  $B$  is the vertical damping.

In Figure 8.14b  $A_{33}$  is the vertical added mass for suction anchor with a given perforation, and  $A_0$  is the added mass for a suction anchor without perforation. When a curve comes close to 1 on the y-axis, the added mass for the actual anchor is close to that of a non-perforated anchor.

From Figure 8.14a, the linear drag for the suction anchor, is found. The perforation ratio of the top plate is set to 6%. Looking at the top blue line, the damping is linear from approximately 45 kN/(m/s). The damping is then divided into the three elements based on which element is assumed to occupy most of the damping. Assuming that most of the damping occurs due to the flow through the vent holes in the top plate, SE 3 gets 77% of the damping ( $35\text{kN}/(\text{m}/\text{s})$ ). The other two elements is given small vertical damping contributions of  $5\text{kN}/(\text{m}/\text{s})$  each (Solaas (2020)).

**Table 8.8:** Vertical linear drag for suction anchor elements.

Element	Linear Drag [N/(m/s)]	Drag per element length [Ns/m <sup>2</sup> ]
SE 1	5000	$1.43 \cdot 10^5$
SE 2	5000	417
SE 3	35 000	$3.5 \cdot 10^5$
Total	45 000	

In this thesis, the vertical drag is implemented as linear drag as in Table 8.8, where each element is given a vertical drag coefficient per meter element length. Alternatively, if experimental results is not at hand, the vertical drag may be implemented as quadratic drag found in *DNV-RP-H103: Modelling and Analysis of Marine Operations* (Figure 5.5).

When it comes to the vertical added mass, this value is calculated from the DNV GL standard, but the results from Sandvik and Solaas (2017) is used to model the effect of perforation ratio on the added mass. From Figure 8.14b, it is seen that with a perforation ratio of 6%, the reduction of added mass is approximately 10%. The vertical added mass properties of the suction anchor is complex from a modeling perspective. This is where the different slender elements is useful. The added mass due to the water above the top plate is represented by SE 1, and the entrapped water from SE 3. Equation 8.1 calculates the added mass for the two elements. The reduction of vertical added mass due to perforation is subtracted after the added mass is calculated. We recall that the vertical direction from the local slender element coordinate system is in the local x-direction.

$$A_{mx} = \underbrace{\rho C_A V_R}_{\text{SE 1}} + \underbrace{\rho \pi R^2 h}_{\text{SE 3}} \quad (8.1)$$

**Table 8.9:** Vertical Added mass for suction anchor elements.

Element	Added mass [kg]	Added mass per element length [kg/m]
SE 1	60 377	$1.725 \cdot 10^6$
SE 2	0	0
SE 3	217 360	$2.17 \cdot 10^6$
Total	277 737	

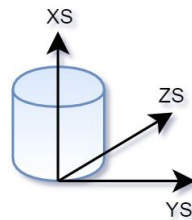


**Figure 8.15:** Slender element coordinate system.

### 8.3.5 Horizontal added mass and damping

The horizontal hydrodynamic properties for the suction anchor is as mentioned, represented by the anchor wall element (SE 2). The large diameter and length of the anchor results in a large projection area in horizontal wave direction, thus drag forces. The drag and added mass is calculated from DNV-GL (2011b). The horizontal added mass is also

two-parted: 3D added mass due to body shape; and added mass due to the weight of entrapped water inside the suction caisson.

The first part of the added mass for the suction anchor is calculated from Figure 5.8 as a 3D cylinder. With a length/diameter ratio 2.4 the added mass coefficient  $C_A$  is 0.767 (interpolated). In Equation 8.2  $R$  is the anchor radius and  $L$  is the anchor length.

$$A_{my} = A_{mz} = \underbrace{(\rho C_A \pi R^2 L)}_{\text{3D added mass from cylinder shape}} + \underbrace{(\rho \pi R^2 L)}_{\text{Weight of entrapped water}} \quad (8.2)$$

**Table 8.10:** Horizontal added mass for suction anchor elements.

Element	Added mass [Kg]	Added mass per element length [kg/m]
SE 1	0	0
SE 2	426 750	35 560
SE 3	0	0
Total	426 750	

The horizontal quadratic damping is calculated from Equation 5.37. The horizontal drag coefficient  $C_D$  is set to 0.6. The suction anchor will have a quadratic damping equal to  $13.7kN/(m/s)^2$ . The surface area is calculated from the horizontally projected cylinder wall.

**Table 8.11:** Horizontal quadratic drag for suction anchor model.

Element	Quadratic drag [ $N/(m/s)^2$ ]	Drag per element length [ $Ns^2/m^3$ ]
SE 1	0	0
SE 2	13 700	1 140
SE 3	0	0
Total	13 700	

## 8.4 Deep Penetrating Anchor Model

The deep penetrating anchor (DPA) is modeled as a solid cylinder with four flukes on the upper half. The DPA hydrodynamic properties are, in general, from a modeling perspective, less complicated than the suction anchor. This is because the DPA is only a solid cylinder without any vent holes or entrapped water. The DPA model consists of two slender elements: the first one represents the cylindrical body, which includes little vertical drag and added mass; the other represents the flukes with the primary horizontal drag contribution.

The DPA dimensions are shown in Figure 8.16. The dimensions are based on the suction anchor described earlier in the thesis. This is for comparative purposes. The anchor mass is also identical (110 000 Kg).

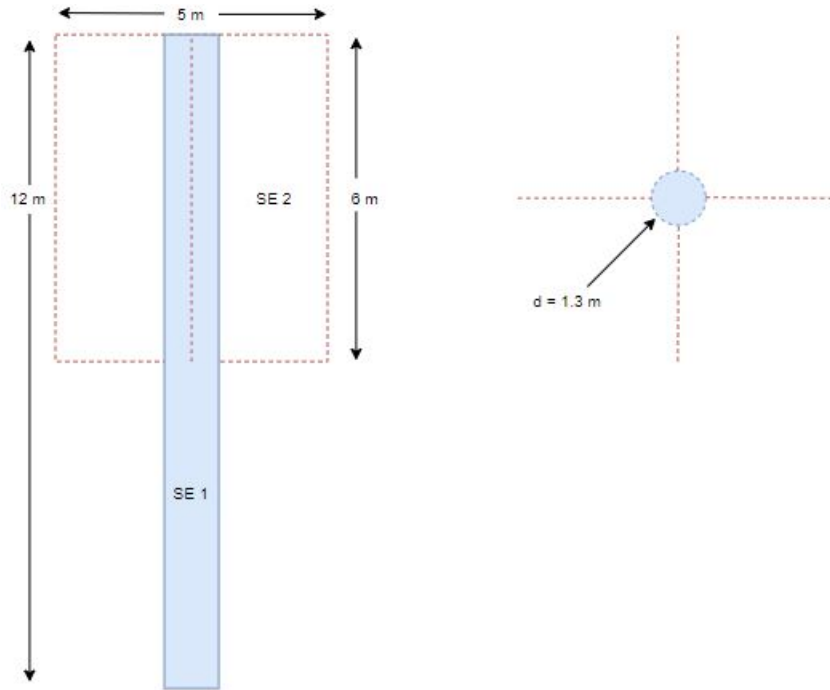


**Figure 8.16:** DPA model with two slender elements.

#### 8.4.1 Shaft element

The shaft element (SE 1) represents the solid shaft body of the deep penetrating anchor model. This element has a diameter equal to 1.3m and is 12 meters long. The element is given a small hydrodynamic contribution i.e. added mass and drag coefficients in both horizontal and vertical directions.

**Table 8.12:** Shaft element properties.

Length [m]	Diameter [m]	Cross section [ $m^2$ ]	Strips
12	1.3	1.38	8

#### 8.4.2 Fluke element

The fluke element (SE 2) is intended to represent the flukes, which in general are two plates perpendicular to each other with dimensions given in Table 8.13. The flukes are modeled as a slender element with cross-section and hydrodynamic coefficients calculated based on two perpendicular plates (Figure 8.16 right). In SE 2, vertical added mass and drag is neglected because of its small projection area in this direction. SE 2 is given a cross-section area equal to  $0.035m^2$ . The cross-section is calculated from two  $0.035m$  thick and  $5m$  wide plates. The width of the plates is set equal to the diameter of the suction anchor (Figure 8.11). The length of the flukes is set to  $6m$ , which is half of the total anchor length.

**Table 8.13:** Fluke element properties.

Length [m]	Width [m]	Thickness [m]	Cross section [ $m^2$ ]	Strips
6	5	0.035	0.35	8

### 8.4.3 Vertical added mass and damping

The vertical DPA added mass is calculated from Table A-2 as for a circular disc (Figure 5.7). In reality, the tip of the DPA anchor will be sharp for soil penetration. This is not the case in the simulation model, where the anchor shaft is a plain cylinder with circular plates at the ends. The added mass will thus be overestimated. The vertical hydrodynamic properties of the flukes are neglected because of their narrow projection area in this direction.

The drag is implemented as quadratic drag with unit  $Ns^2/m^2$ , and calculated from Table B-2 in DNV-RP-H103 (Figure 5.5).

**Table 8.14:** Vertical Added mass and quadratic drag for DPA.

Element	Added mass [Kg]	Quadratic drag [ $Ns^2/m^2$ ]
SE 1	750	680
SE 2	0.0	0.0
Total	750	680

### 8.4.4 Horizontal added mass and damping

The horizontal hydrodynamic properties of the DPA is found from two contributions: the cylinder and the flukes. The flukes are modeled as two plates perpendicular to each other, which results in one plate normal to the horizontal flow direction. The horizontal added mass and quadratic drag for the flukes is therefore calculated from rectangular plates. The 1.3m diameter anchor shaft will also have a small horizontal drag and added mass contribution.

The horizontal added mass for the shaft (SE 1) is found from Figure 5.8 (DNV-GL (2011b)) where the drag coefficient  $C_D$  is set to 0.96 based on the length/diameter ratio. The added mass for the flukes (SE 2) is calculated from Figure 5.7 (DNV-GL (2011b)). The drag coefficient is interpolated to be 0.629. The horizontal quadratic drag of SE 1 and SE 2 is found from Figure 5.5 for circular cylinder and rectangular plate, respectively.

**Table 8.15:** Horizontal added mass and quadratic drag for DPA.

Element	Added mass [Kg]	Quadratic drag [ $Ns^2/m^2$ ]
SE 1	15 670	5 436
SE 2	75 954	17 865
Total	91 624	23 301

## 8.5 Anchor Kinetics

Both anchors are given a mass and moment of inertia. The moment of inertia is calculated for three degrees of freedom (x, y and z) and implemented in the anchor models as mass coefficients. In Equation 8.3 and 8.4  $M$ ,  $R$  and  $L$  is the anchor weight, radius and length respectively. The anchor model kinetics are shown in Table 8.16. Its worth mentioning that the moments of inertia is calculated from the local anchor body coordinate system, thus z is the vertical direction.

$$I_{zz} = \frac{MR^2}{2} \quad (8.3)$$

$$I_{xx} = I_{yy} = \frac{MR^2}{4} + \frac{ML^2}{12} \quad (8.4)$$

**Table 8.16:** Mass and moment of inertia properties for SA and DPA.

	Mass [Kg]	Ixx [ $Kgm^2$ ]	Iyx [ $Kgm^2$ ]	Iyy [ $Kgm^2$ ]	Izx [ $Kgm^2$ ]	Izy [ $Kg^2$ ]	Izz [ $Kgm^2$ ]
<b>SA</b>	110 000	$1.4919 \cdot 10^6$	0.0	$1.4919 \cdot 10^6$	0.0	0.0	343 750
<b>DPA</b>	110 000	$1.3316 \cdot 10^6$	0.0	$1.3316 \cdot 10^6$	0.0	0.0	23 237

## 8.6 Static analysis

During the modelling of the suction anchor and the DPA one can compare the initial and static position of the anchor bodies to ensure that the model is implemented correctly before running the simulations. For this particular model, the design of the slings and the hook position together with the anchor dimensions is a critical part of the modelling as these parameters are dependent on each other when placed on top of each other in the model. If these bodies are placed incorrect, the static analysis will reveal the error when comparing the static position to the initial position. The static analysis contains no time-varying effects and provides information about the system equilibrium. In Table 8.17 and 8.18 the difference of the initial and static position is calculated. The smaller the difference, the better model.

**Table 8.17:** Initial and static position for SA model.

	Initial Position	Static Position	Difference
(x, y, z)	(-24.5, 27.85, 4.3)	(-24.5, 27.85, 4.1)	(0.0%, 0.0%, 4.6%)
(rx, ry, rz)	(0, 0, 0)	(0.05, 0.014, 0.0)	(5%, 1.4%, 0.0%)

**Table 8.18:** Initial and static position for DPA model.

	Initial Position	Static Position	Difference
(x, y, z)	(-24.5, 27.85, 4.3)	(-24.5, 27.9, 4.34)	(0%, 0.17%, 0.92%)
(rx, ry, rz)	(0, 0, 0)	(-0.016, -0.006, 0.0)	(1.6%, 0.6%, 0.0%)





# Chapter 9

## Simulation Properties

### 9.1 Environmental Conditions

The environmental conditions implemented in the model are based on data from the Tampen area located in the North Sea west of Bergen, Norway. In this area, Equinor is planning to install the world's biggest floating wind park consisting of eleven turbines with a total capacity of 80-100MW (NRK (2020)). The field will produce one-third of the total energy demand for the Snorre and Gullfaks platforms nearby. The wind park is located about 140 km from shore at 260-300 meters water depth. Each turbine will have a rotor diameter of about 160-170 meters and have a draft of 90-100 meters. The turbines are moored to the seabed with three anchor lines extending 900 meters. The wind park will occupy an area of approximately  $22.5 \text{ km}^2$  on the seabed (Equinor (2018)).



**Figure 9.1:** Hywind Tampen ( $61^{\circ}15', 995' N^{\circ}16, 117' E$ )

#### 9.1.1 Wave Conditions

The wave conditions are based on the environmental conditions at the Tampen area. A text file containing 14 800 data points from 1957 to 2019 is used to plot significant wave height ( $H_s$ ) and peak period ( $T_p$ ). This means that the measurements are done with a 3 hour interval the last 62 years.

Significant wave height ( $H_s$ ) and peak period ( $T_p$ ) is plotted to find the mean  $T_p$  for each  $H_s$ . To consider extreme values, and for the wave conditions in the simulation to be conservative, the P5 and P95 probabilities are identified based on the mean  $T_p$ . The scatter plot can be seen in Figure 9.2, and MATLAB code is included in Appendix B.2.

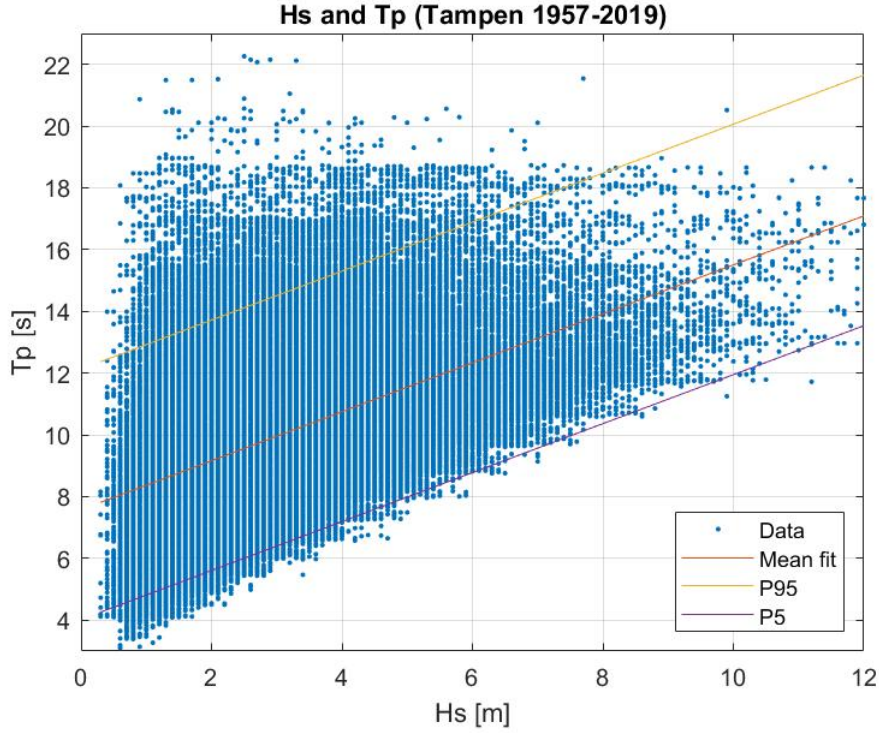


**Figure 9.2:**  $H_s$  and  $T_p$  in the period 1957-2019 Tampen area.

The condition set can be seen in Table 9.1. The  $H_s$  interval is chosen based on the assumption that the limiting operational environmental criteria ( $H_{s_{lim}}$ ) will be here.

To identify which wave periods will be critical in terms of the vertical vessel and crane tip motions, the vessel RAO is analyzed to identify the vessel eigen periods for heave, pitch, and roll. These motions are selected because they will directly affect the vertical motion in the crane tip. The simulation is performed for three different wave directions:  $180^\circ$ ,  $160^\circ$  and  $135^\circ$ . The vessel eigen period greatly depends on the wave direction, and the colors in Table 9.1 represent the eigen period interval for the three wave directions based on the vessel RAO. The green periods represent the vessel eigen period interval in heave. The yellow is the pitch eigen period and the blue is the roll.  $180^\circ$  wave direction contains negligible roll motion and direction of  $160^\circ$  and  $135^\circ$  with the same eigen period of 14.5 seconds.

**Table 9.1:** Condition sets used in Simulation. Colours represent vessel eigen period interval for wave dir. 180°160°135° : green = heave, yellow = pitch, blue = roll.

Hs	P5 Tp [s]	Mean Tp [s]	P95 Tp [s]
1	4.8	8.4	12.9
1.5	5.2	8.8	13.3
2	5.6	9.2	13.7
2.5	6	9.6	14.1
3	6.4	10.0	14.5
3.5	6.8	10.4	14.9
4	7.2	10.8	15.3
5	8	11.6	16.1
6	8.8	12.3	16.9

## 9.2 Simulation length

To estimate the simulation length, the vertical water particle motion is studied. The length of the simulation is found by using Equation 9.1 and locating at what depth the vertical fluid particle motion is negligible and thus the sea environment is no longer much energized.

$$w = \omega \zeta_a e^{kz} \cos(\omega t - kx) \quad (9.1)$$

In Equation 9.1  $\omega$  is the wave frequency and equal to  $\frac{2\pi}{T}$ .  $\zeta_a$  is the wave amplitude,  $z$  is the vertical coordinate positive upwards and zero at the mean water surface.  $k$  is called the wave number and is dependent on the wave length  $\lambda$ .  $k$  is equal to  $\frac{2\pi}{\lambda}$ .

Based on this and with a winch speed set to 0.2 m/s the length of the simulations is set to 885 seconds. This duration should be sufficient for the anchor to be lowered approximately 170 meters below the mean water surface, where the vertical fluid motion is low. In Figure 9.3 the vertical fluid particle velocity is plotted as a function of water depth. Here the wave period is set to 15.7 seconds with a wave amplitude of 4 meters. These wave properties are used because this is the largest wave used in the suction anchor simulation.

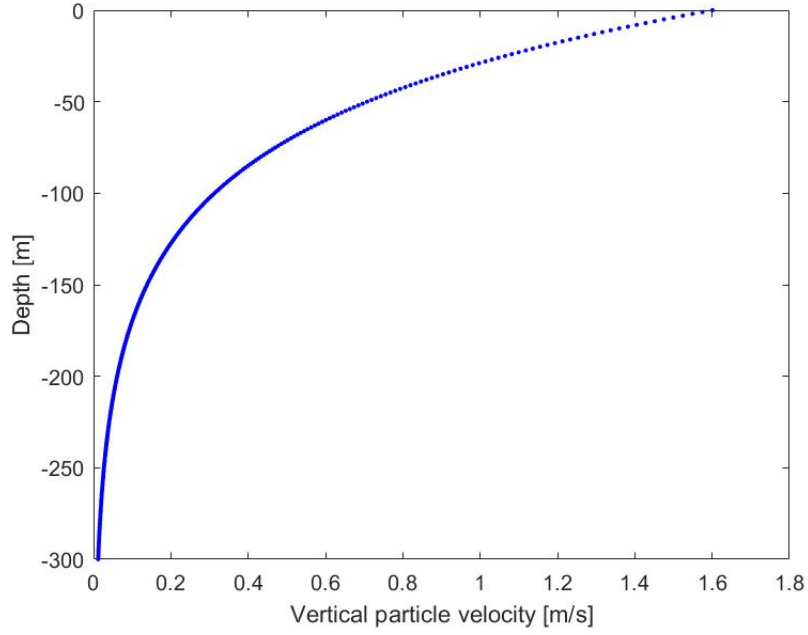


**Figure 9.3:** Vertical particle motion as a function of water depth.

### 9.3 Eigen Period of Crane Wire

The eigen period of the crane wire is calculated by Equation 9.2. Here  $M$  is the anchor mass, which is identical for both anchors, and  $A_{33}$  is the vertical added mass.  $K = EA/L$  is the elastic stiffness of the crane wire  $EA$  is the axial stiffness, and  $L$  is the wire length. Resonance in the crane wire is a phenomenon that occurs with a slight excitation of the lifted object. Figure 9.4 shows the eigen period of the system for the DPA and SA calculated with Equation 9.2. The wave conditions in the simulation contain peak periods from 4.8 to 16.9 seconds. If the period of the waves and the eigen period of the system coincide, resonance behavior might occur. Figure 9.4 shows that the probability of experiencing resonance is low for the higher peak periods. For  $H_s = 1m$  simulation with a peak period of 4.8 seconds, some of the waves can contain a peak period down towards 3-2.5 seconds, and the resonance phenomenon might occur.

$$T_r = 2\pi\sqrt{\frac{M + \frac{1}{3}mL + A_{33}}{K}} \quad (9.2)$$

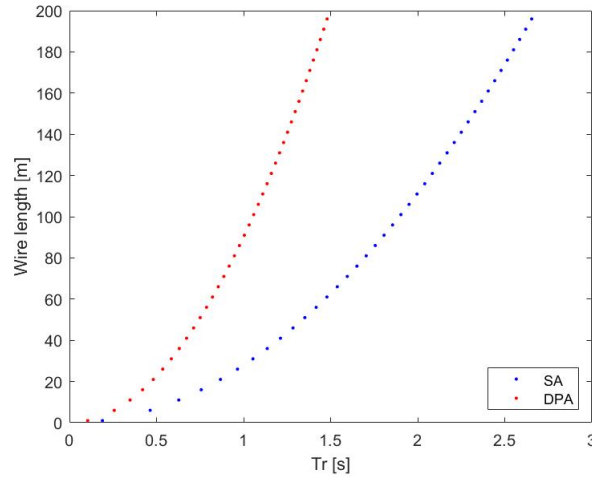


**Figure 9.4:** Vertical resonance period for SA and DPA.

### 9.3.1 Eigen Period Validation of Simulation Model

Figure 9.5 shows the suction anchor lowered in initial conditions. Before the crane winch is started after 35 seconds. The static force in the crane wire shows a value of 1196.8 kN, which is the weight of the anchor and the crane block (122 000 Kg). The first decay arise after 114 seconds where added mass of the entrapped water is activated.

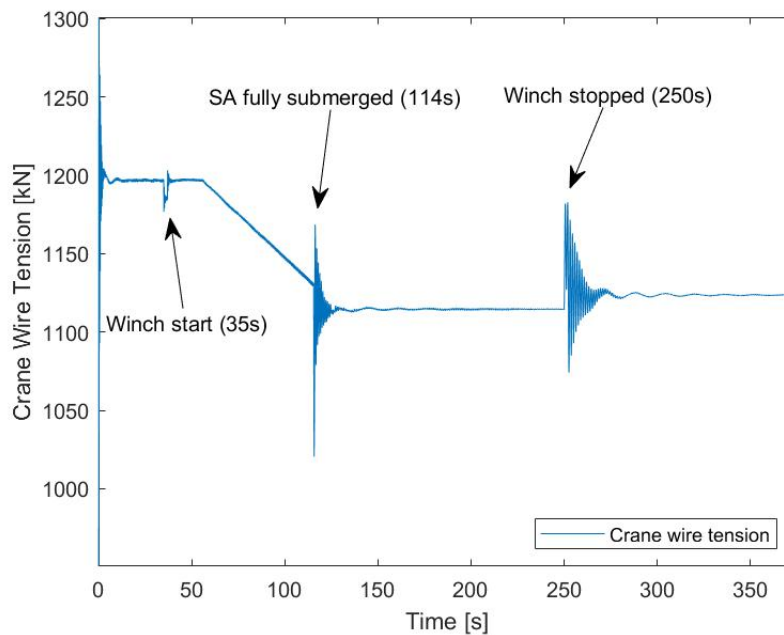


**Figure 9.5:** SA in initial conditions with winch start and stop.

The winch is stopped after 250 seconds to compare the eigen period of the decay from the simulation against the manual estimations of Figure 9.4 using Equation 9.2. At this point, the wire length is equal to 55 meters. Studying the decay of Figure 9.5 the motions of the crane tip can be seen as the longer tension period just after the eigen period oscillation at 250s. The mean tension in the wire is slightly increased after the winch is stopped, as vertical drag resulting from the hoisting velocity is gone.

Figure 9.6 shows the auto spectrum of the decay after 250 seconds when the winch is stopped. The auto spectrum  $S_{xx}(f)$  is computed with the post processor application in SIMA where the time series  $x(t)$  is divided into  $N$  parts. The Fourier transform of the time series of the individual parts are computed by SIMA using Equation 9.3 (SINTEF Ocean (2019a)). To investigate the eigen period, the time series from 250 to 300 seconds is outputted as a function of frequency.

$$S_{xx}(f) = \frac{1}{N} \sum_{j=1}^N \left| \int x_j(t) \exp(-2\pi i f t) dt \right|^2 \quad (9.3)$$

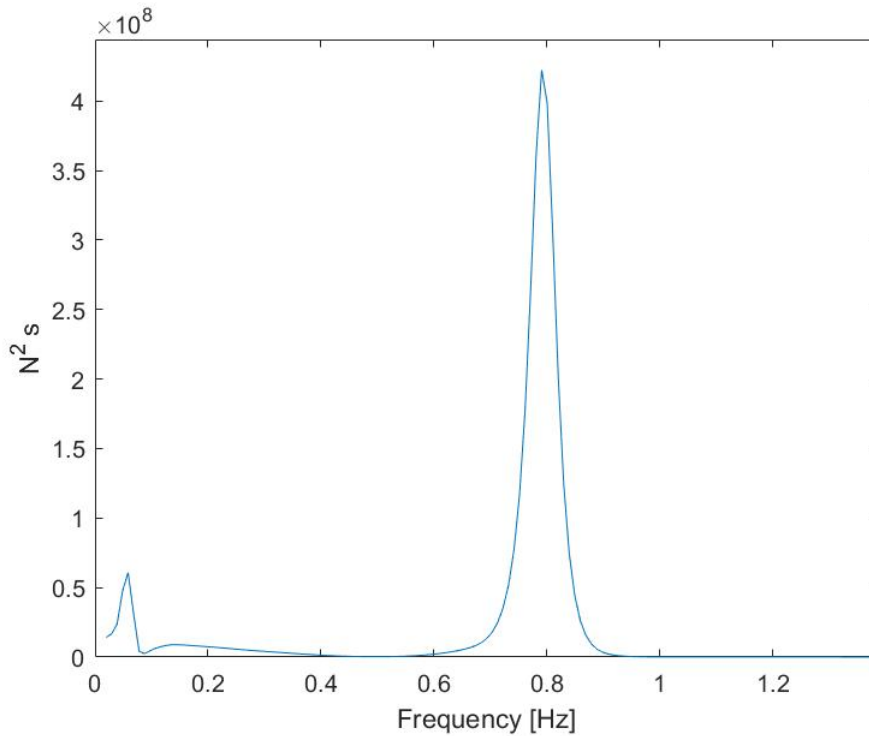


**Figure 9.6:** Wire tension spectrum for SA model in initial conditions.

The peak at 0.78 Hz represents the eigen period of the system (1.3 seconds) which corresponds to the manually calculated eigen period. A small peak is also seen at 0.07 Hz, which is equal to the vessel eigen period in roll (14.5 seconds).

The same is done for the DPA. A time series of a DPA simulation with initial conditions is found in Figure 9.7. Also, here, the crane wire holds a total weight of 122 000 Kg (1196 kN) in air. The winch is started at 35 seconds. The negligible vertical added mass compared to the SA yields no remarkable dynamics in the wire tension at 114 seconds when full submergence is achieved. The resonance period of the crane wire is analyzed at 250 seconds (60 m wire length).

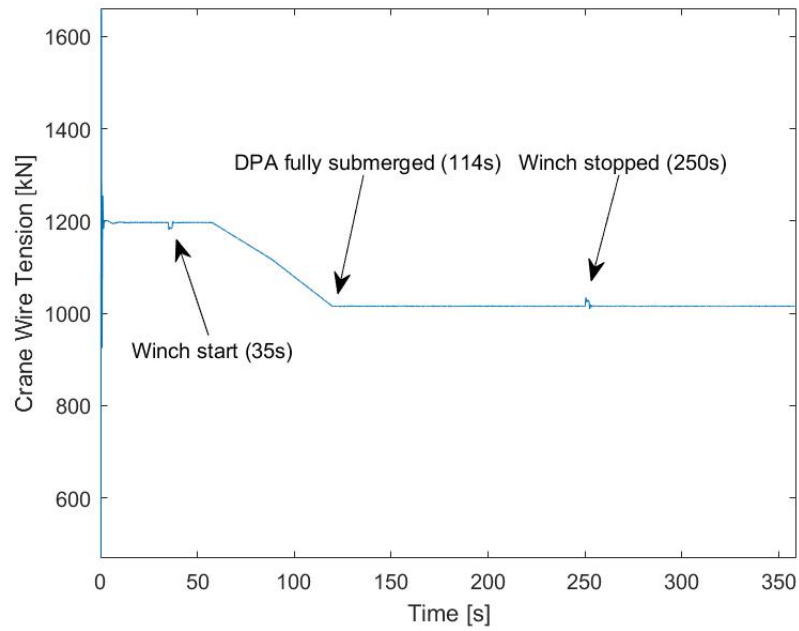


**Figure 9.7:** DPA in initial conditions with winch start and stop.

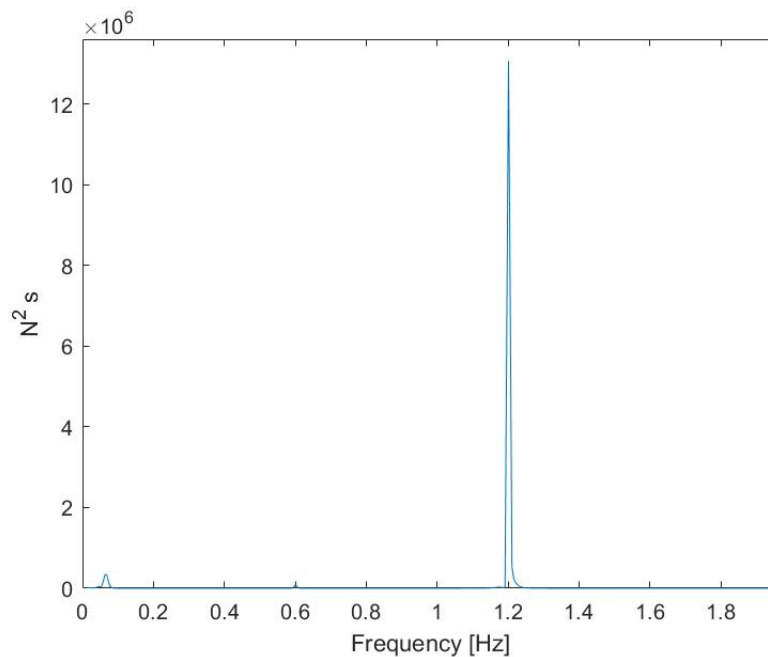


**Figure 9.8:** Wire tension spectrum for DPA model in initial conditions.

It is noted that the SIMA models are given a crane flexibility equal to  $1.33 \cdot 10^{-7}$  m/N after the eigen period investigation is performed. This is to consider the stiffness in the connection point (the crane tip). It is used to model the flexibility in the crane and not only the wire from the crane tip down to the anchor. This flexibility from the crane makes the system softer, and this results in a slightly longer eigen period (approximately 0.6 seconds longer at 50m depth).

## 9.4 Maximum and Minimum Allowable Tension

DNV GL's slack criterion decides the minimum tension. The slack criterion states that the tension in the crane wire shall not be lower than 10% of the submerged static tension. If the criteria is exceeded, there is a risk of slack in the crane wire, which can result in large snap forces (DNV-GL (2011b)). The static submerged tension in the crane wire for the SA and DPA models is found from Figure 9.5 and 9.7, respectively. For the SA, the static submerged tension is 1124 kN, which corresponds to a slack criterion of 112.2 kN. The static submerged wire tension for the DPA model is 1016 kN, which results in a 101.5 kN slack criterion.

The crane wire includes a design strength that, together with a safety factor of 3, must not be exceeded (DNV-GL (2016b)). The crane wire chosen for this model has a breaking strength of 5821 kN, which with the safety factor, has a design strength of 1940 kN. The hoisting wire characteristics was given in Table 8.4. A summary of the allowable tension is given in Table 9.2.

This means that the maximum limit for a wave condition is set when the P90 probability from the sample of extreme maximum crane wire tension exceeds 1940kN. The slack requirement is violated when the P10 probability from the extreme minimum for a wave condition is below the minimum allowable tension.

**Table 9.2:** Maximum and minimum allowable crane wire tension for SA and DPA.

	P10 Minimum	P90 Maximum
Suction anchor	112.2 kN	1940 kN
Deep penetrating anchor	101.5 kN	1940 kN

## 9.5 Seed Number

A study is performed to locate the minimum amount of seeds needed to get reliable results. This is done by performing convergence tests on the MPM parameter  $\mu$  from the Gumbel distribution, and see when it converges. The convergence test is done by running the simulation for one sea condition, starting with a low seed number. Gradually, the seed number is increased, thus increasing the sample of extreme maximum MPM.



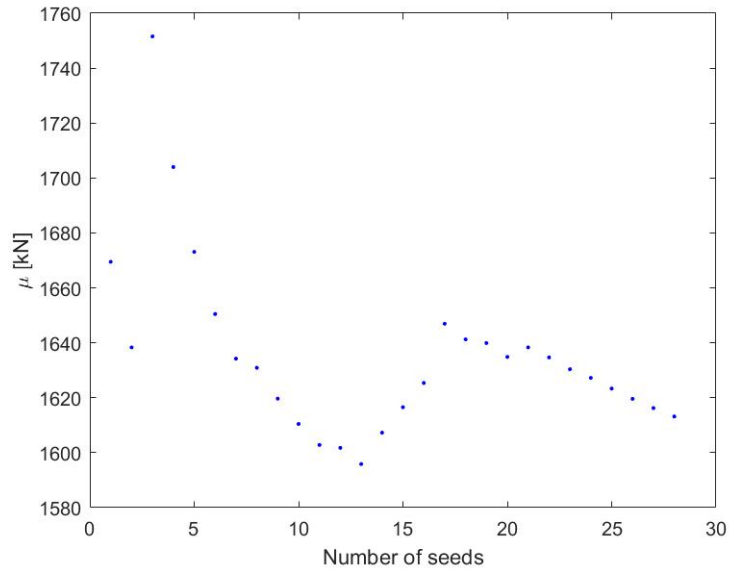


**Figure 9.9:** Convergence test for  $H_s=1\text{m}$ .

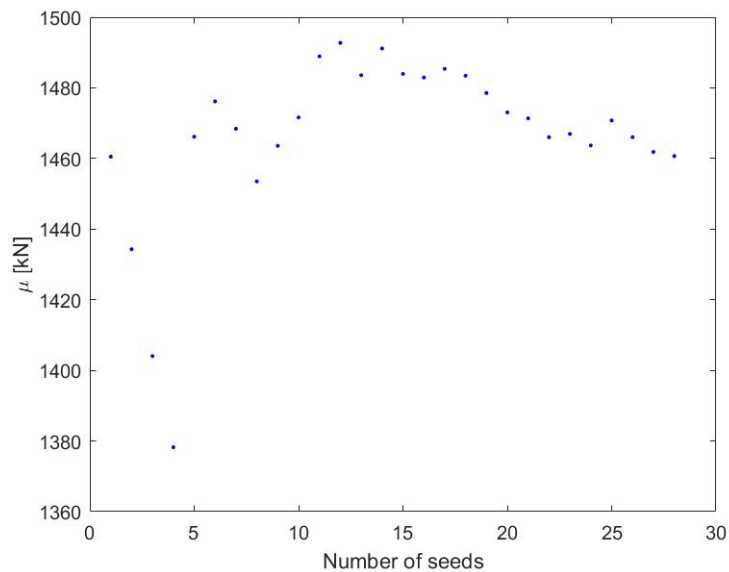


**Figure 9.10:** Convergence test for  $H_s=2\text{m}$ .

Figure 9.9 and 9.10 shows the results of two convergence tests for significant wave height  $H_s$  1 and 2 meter from 1 to 28 seeds. This was also done for higher  $H_s$  to check if higher  $H_s$  conditions required larger seed numbers. The plots showed little change in  $\mu$  after the seed number has surpassed a value around 5. The simulations in this thesis is performed with 5 seeds. Although this seed number is low, it is assumed that the difference from 5 seeds to higher seed numbers are low and thus the saved computational time is significant.

## 9.6 Simulation Properties

The simulation starts with the anchors hanging 4.2 m above water level. The winch start time is set to 35 seconds for the system to stabilize before initiating the anchor lowering. The winch stop time is set to the end of the simulation. Winch speed is set to 0.2 m/s, as this is a common lowering speed (Larsen (2020)).

The simulations is run for three wave directions: 180°, 160° and 135°. The simulation time step is set to 0.01 seconds, as this time step should be sufficient to consider the elasticity of the crane wire.

**Table 9.3:** Simulation characteristics.

Sart time winch	Stop time winch	Winch speed	Time step	Wave directions	Seeds
35 s	885 s	0.2 m/s	0.01 s	180°, 160°, 135°	5

Table 9.4 shows the selected  $H_s$  conditions for the SA and DPA. It is assumed that the limiting operational environmental criteria ( $H_{s_{lim}}$ ) for both anchors will be within these  $H_s$ -intervals. The simulations starts with a low  $H_s$ , which is gradually increased until design criterion is identified. Tests with the DPA model reveals that low  $H_s$  results in low hoisting wire tensions, therefore the condition set for the DPA starts at a higher  $H_s$ .

**Table 9.4:** Selected  $H_s$  conditions for SA and DPA simulation.

Hs [m]	Suction anchor	Deep penetrating anchor
1	x	
1.5	x	
2	x	
2.5	x	
3	x	
3.5	x	
4	x	x
5		x
6		x

# Chapter 10

## Simulation Results

### 10.1 Crane Tip Motion

The crane tip is located at  $x = -24.5m$ ,  $y = 27.8m$  and  $z = 32.6m$ , and the motion here is directly transferred from the vessel motion. The response in the crane tip is calculated by Equation 5.34 using the heave, pitch, and roll motions of the vessel COG from SIMA, located at  $x = 0.12m$ ,  $y = 0m$  and  $z = 4.25m$ .

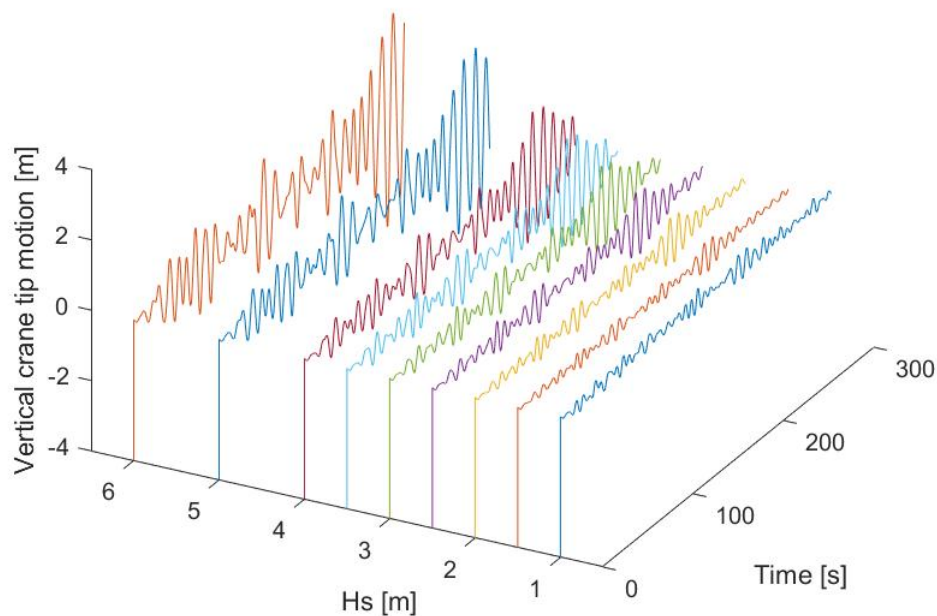


**Figure 10.1:** Vertical crane tip motion with increasing  $H_s$ .

Figure 10.1 shows how the vertical crane tip motion is increased with increased  $H_s$ . Here, the time series show the result from simulating the  $H_s$  with the mean peak period of Table 9.1 and  $180^\circ$  wave direction. Figure 10.1 shows that with increased wave condition, one must expect more significant anchor vertical motions, and this will result in more considerable tensions in the crane wire. Although the vertical motion is increased with  $H_s$ , so will the direct wave excitation forces. When the anchor is lowered beneath the wave energy area, the crane tip motions are the only force contribution for the crane wire, and this is where the crane tip motion is essential.

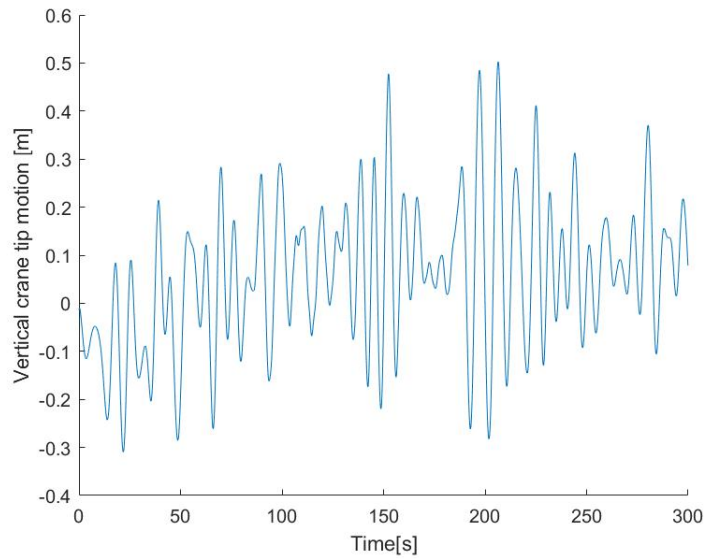


**Figure 10.2:**  $H_s=1\text{m}$   $T_p=8.4\text{s}$ .

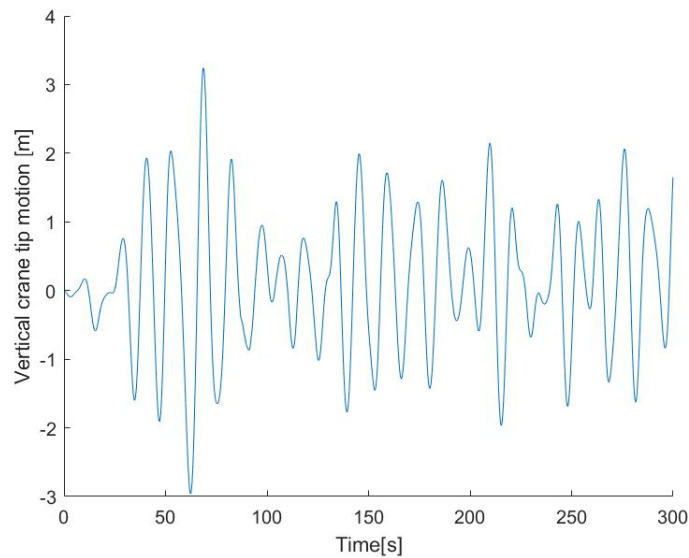


**Figure 10.3:**  $H_s=6\text{m}$   $T_p=12.3\text{s}$ .

## 10.2 Suction Anchor

The winch starts lowering the SA after 35 seconds. In this phase is the SA hanging in the air until the mean water line is reached after 57 seconds. The anchor is fully submerged after 114 seconds (Figure 10.4c). The model consists of three slender elements with dept dependent coefficients to model the drag and added mass through the splash zone. After 114 seconds, the top plate of the anchor is submerged, which results in a sudden increase of added mass. The water inside the anchor that until now has been allowed to move freely in the vertical direction is suddenly trapped, and this results in a drastic increase in added mass.

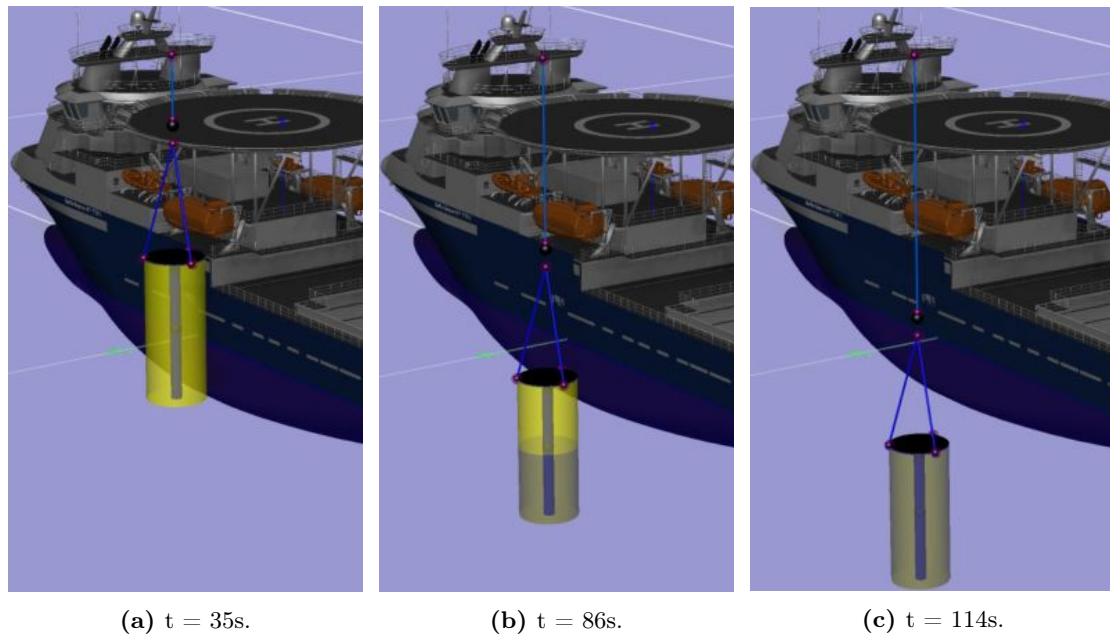


**Figure 10.4:** Visualization of SIMA SA lowering.

We start by comparing the tensions in the slings with the crane wire tension (Figure 10.5). Here, a simulation is performed with  $H_s = 1.5m$  and  $T_p = 8.8s$ . The crane wire and the slings are of the same material and thus holds the same design strength. The total crane wire tension also includes the weight of the hook (12t). The slings share the total force from the anchor, and therefore it is not expected that the maximum tension is near the breaking strength.

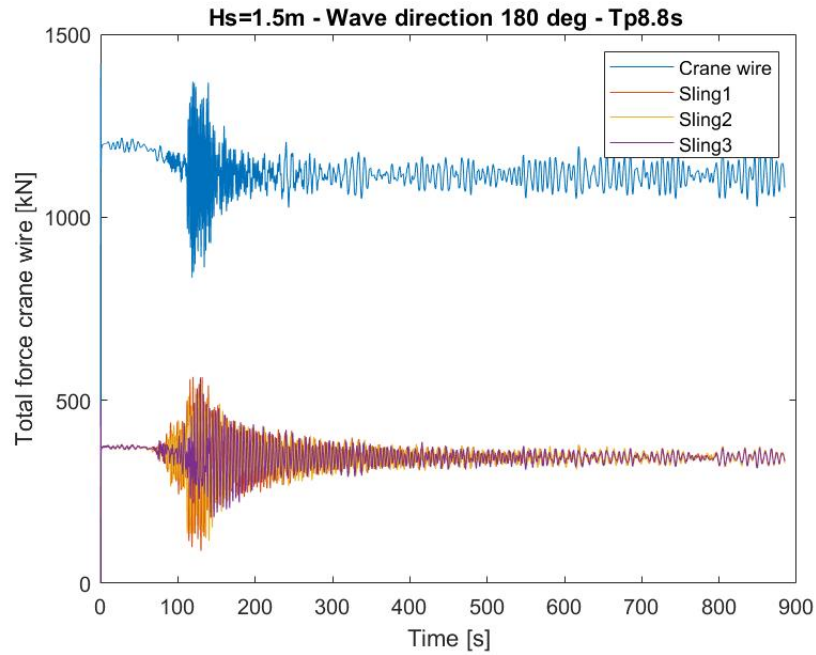


Figure 10.5: Tension in crane wire compared to tension in slings.

### 10.2.1 Tension in Crane Wire

SIMA outputs a time series showing the total crane wire tension as a function of simulation length. A large part of the simulations show that the crane wire experiences a lot of dynamics throughout the splash zone. This is a result of direct wave excitation forces and crane tip motions.

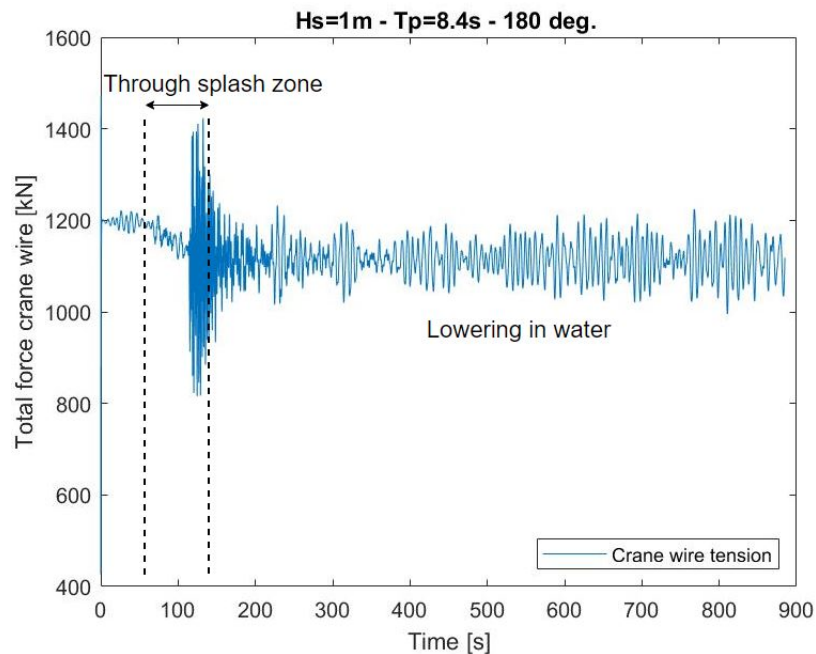
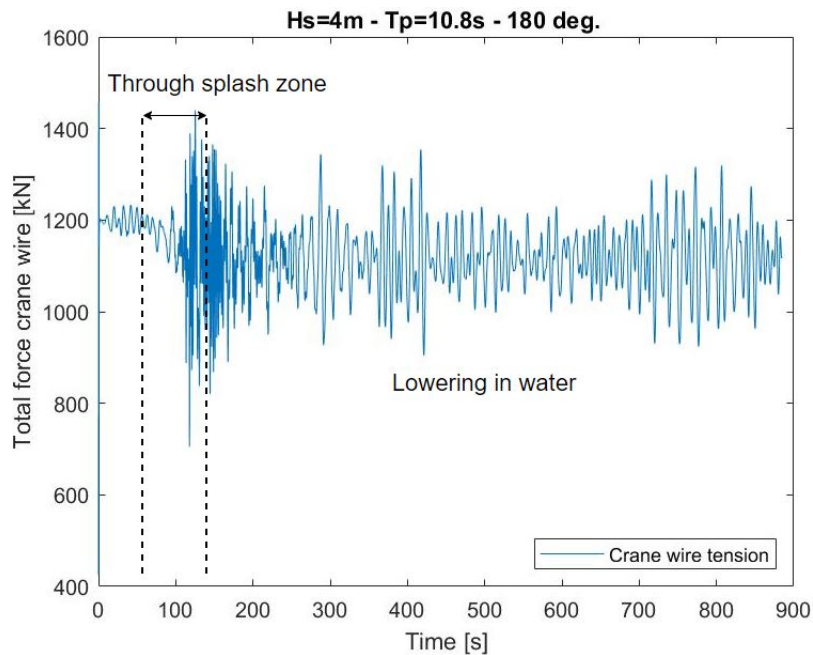


Figure 10.6: Crane wire tension through splash zone and lowering,  $H_s = 1m$ .

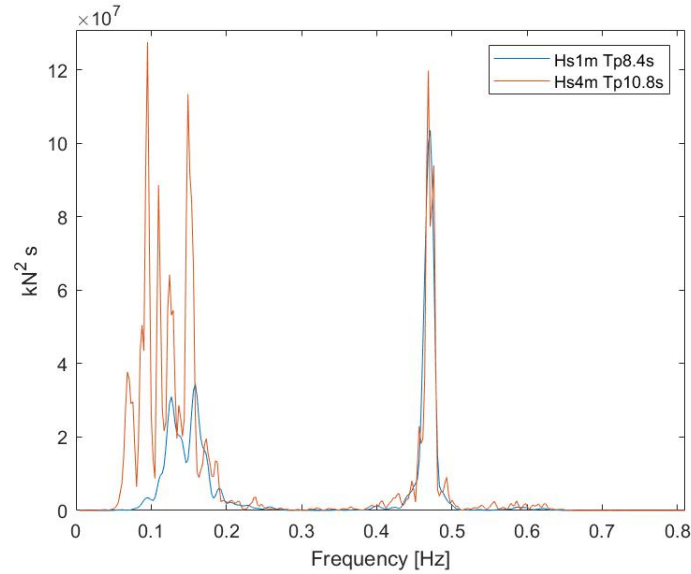
Figure 10.6 shows the time series from the suction anchor model simulated in  $H_s = 1m$ . Here, it is reasonable to believe that the peaks through the splash zone is a result of direct wave excitation forces. As seen in Figure 10.1,  $H_s$  1m does not induce large crane tip motions. The tensions due to crane tip motions become visible when the anchor is lowered beyond the range of wave energy.

Figure 10.7 shows the same scenario with increased  $H_s$  to 4m. With increased wave conditions, the tensions in the lowering phase is larger. This wave condition also has a larger wave period, which results in larger water particle acceleration deeper than compared to Figure 10.6. However, at depths up to 160 meters (800 seconds), there will be negligible water particle motions from the waves, and the Figure 10.7 still show large tension dynamics at this point. This gives reason to believe that these forces come from vertical crane tip motion.



**Figure 10.7:** Crane wire tension through splash zone and lowering,  $H_s = 4m$ .

The auto spectrum of the  $H_s = 1m$  and  $H_s = 4m$  with its respective mean periods are plotted in Figure 10.8. Here, the SA is lowered to full submergence in the splash zone, the winch is stopped, and the time series from crane wire tension is analyzed for 500 seconds. The plot shows at what frequencies the tension results from. The peaks due to the wave periods are located at the lower frequency range. Here, the energy density due to the peak periods is spread out as the waves contain some periods above and beneath the simulated peak period.



**Figure 10.8:** Wire tension spectrum for SA model in splash zone.

The energy densities shows the load differences for the two conditions. Going from  $H_s = 4m$  to  $H_s = 1m$  results in a tremendous decrease in the energy density. At 0.47Hz the peak is due to the eigen period of the system. Here, the two wave conditions are close to similar in energy density. The magnitude of the energy density from resonance in the crane wire is dependent on wave period, this can be seen in Figure 10.9. Here,  $H_s = 1m$  and two different  $T_p$  is plotted. The low period waves is much more energized. The longest  $T_p$  of 10.8s results in a significantly lower energy density.

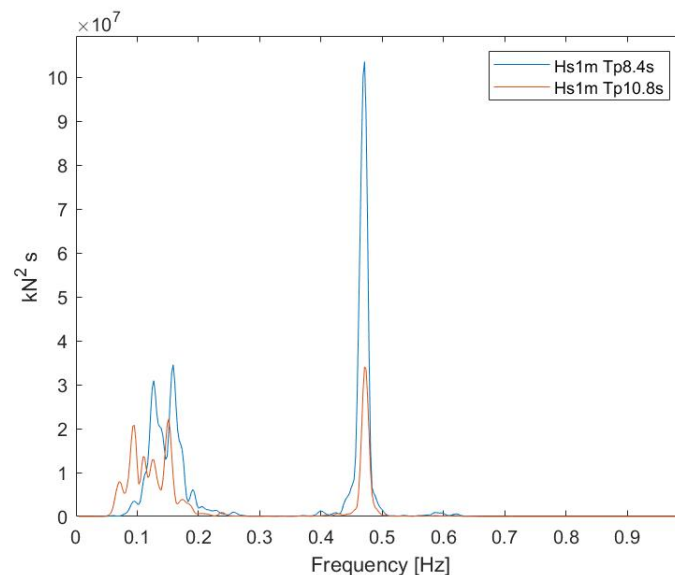


**Figure 10.9:** Tension spectrum for SA model. Same  $H_s$  with two different wave periods.



A simple way to identify the forces, is to study the time series of the total crane wire tension, and look for phenomenons that excludes some theories. A slamming impulse are likely to occur where there is a sudden increase of added mass and even more likely if the wave period is small with high energy and acceleration. A slamming impulse should in this case be a peak in the tension, that oscillates at resonance for a while. The slamming force is dependent on change in added mass and will therefore disappear when full added mass is achieved.

Figure 10.10 shows an example of a slamming impulse for the suction anchor model. The impulse occurs at 114 seconds, exactly when the top plate of the anchor is submerged and the vertical added mass i increased 80%. In accordance to Figure 8.12, full added mass i achieved when the top plate i lowered approximately 5 meters (after 140 seconds).

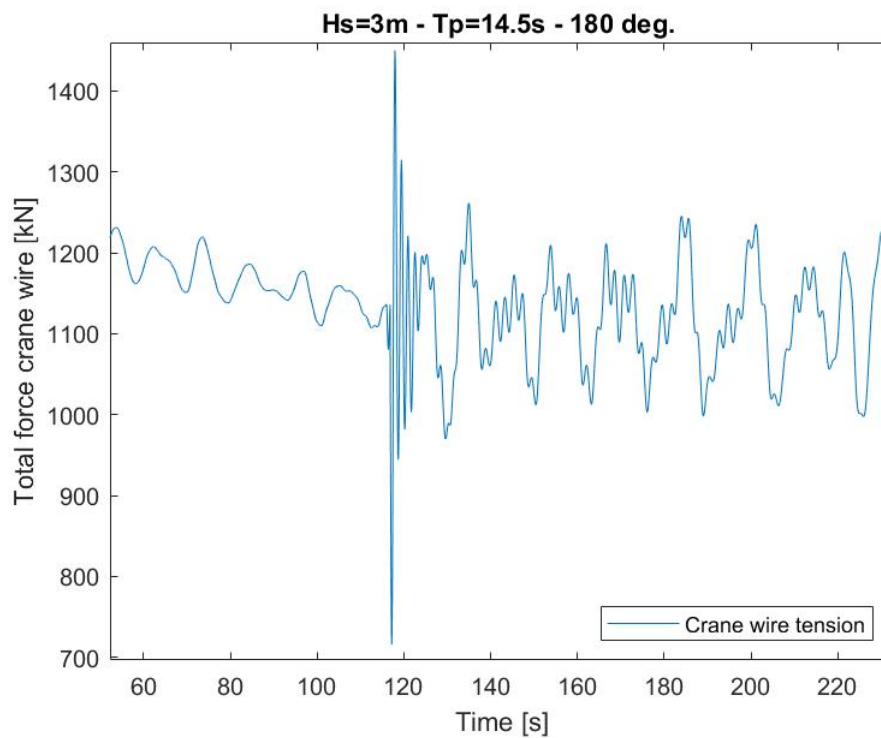


**Figure 10.10:** Total crane wire tension with  $T_p$  14.5s.

### 10.3 Deep Penetrating Anchor

The deep penetrating anchor (DPA) model is subjected to  $H_s = 4$ ,  $H_s = 5$  and  $H_s = 6m$  condition sets found in Table 9.1. Results from the DPA model show less tension dynamics through the splash compared to the suction anchor.

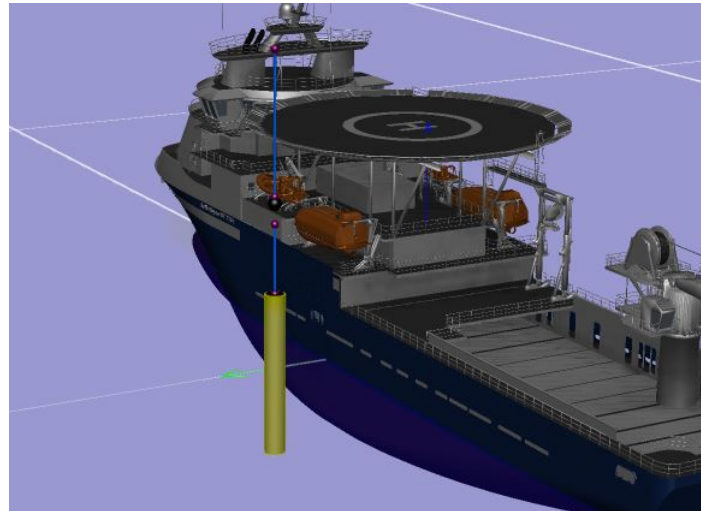


Figure 10.11: DPA model in SIMA.

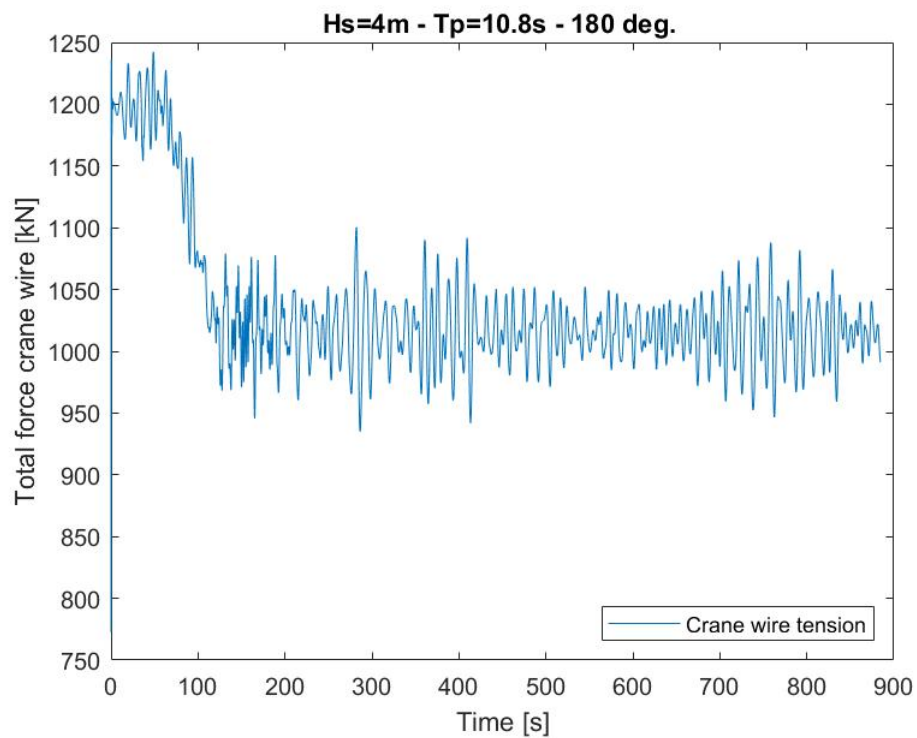
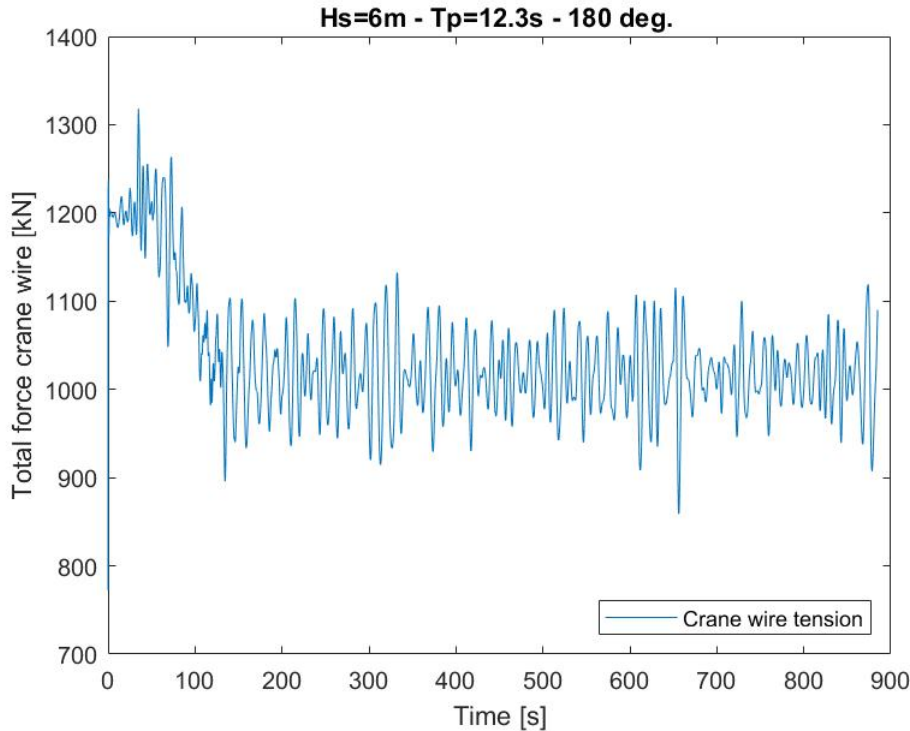


Figure 10.12:  $H_s = 4m$ ,  $T_p = 10.8s$ .



**Figure 10.13:**  $H_s = 6m$ ,  $T_p = 12.3s$ .

One reason to this is that the difference in added mass is significant. The DPA got 0.3 % of the vertical added mass compared to the suction anchor. The shape of the DPA is a solid cylinder with relatively small horizontal and vertical projected areas, this results in less direct wave excitation forces on the anchor.

Figure 10.12 and Figure 10.13 show total crane wire tension time series for different wave conditions. There is no significant tension peaks in the splash zone around 114s in any of the wave conditions. Figure 10.13 has a higher wave condition which results in larger forces compared to Figure 10.12. The differences are not as significant as for the SA time series.

The two anchor models have the same mass of 110 tons, but the results show completely different crane wire tensions for the two models.

## 10.4 Gumbel Distributions

The Gumbel distribution is studied to locate the design criterion in terms of significant wave height  $H_s$ . For each vessel heading and wave condition, the post-processor application in SIMA is used to gather the extreme values. The extreme maxima and minima are then read by MATLAB to plot the CDF's (Appendix B.2). Gumbel plots (section 6.1.3) is used to make sure that the data set fits the Gumbel distribution.

### 10.4.1 Extreme Minimum Distributions

The slack criterion was calculated to be 112.2kN and 101.5kN for the SA and DPA, respectively. Figure 10.14 - 10.16 shows the distribution of the extreme minimum's gathered from the suction anchor model. The 10% fractile for the distributions are over the slack criterion for all the different wave directions. This means that there is less than 10% chance of experiencing slack in the crane wire for the simulated wave conditions.

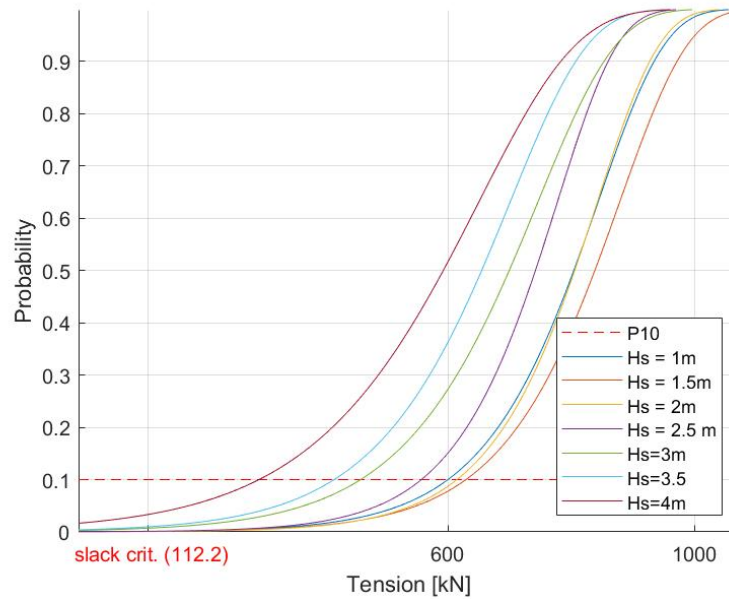


**Figure 10.14:** Suction anchor extreme minimum distribution wave direction 180°.

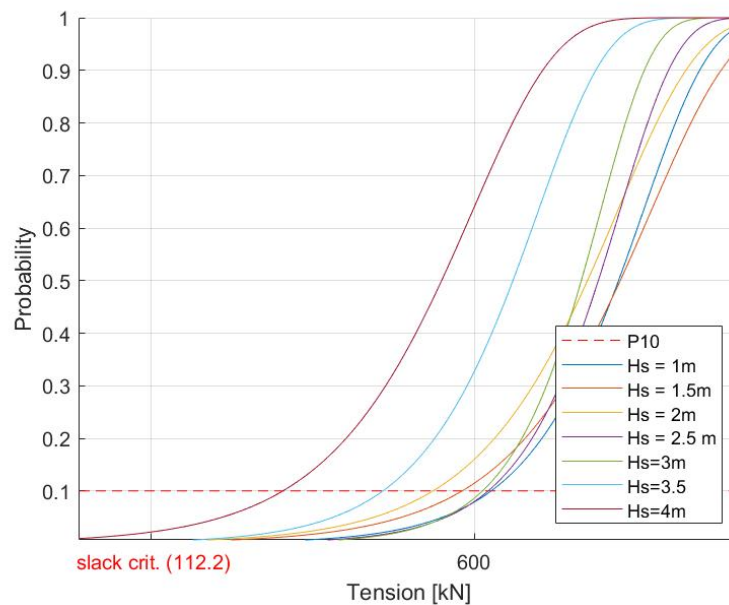


**Figure 10.15:** Suction anchor extreme minimum distribution wave direction 160°.

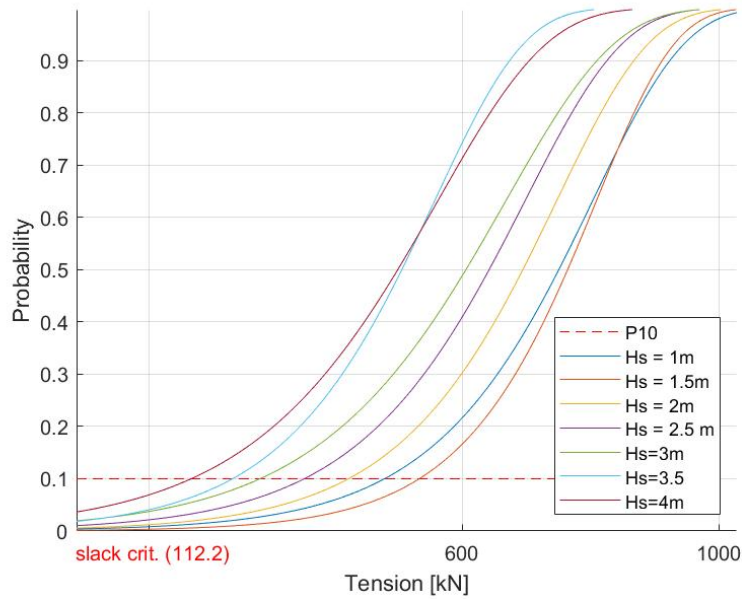


**Figure 10.16:** Suction anchor extreme minimum distribution wave direction 135°.

The extreme value distributions of the minimum shows that the 10% fractile is closing in on the slack criteria with increased wave conditions. The modeling of evacuation of the entrapped air inside the SA is complex. A source of error in the minimum assessment may be that high relative vertical motions between the SA and the waves through the splash zone, depending on the perforation ratio in the top plate, can result in large buoyancy and tilting of the anchor (Ølund Bertelsen (2014)). Here, it is assumed that there is an equal water level inside, and outside the anchor.

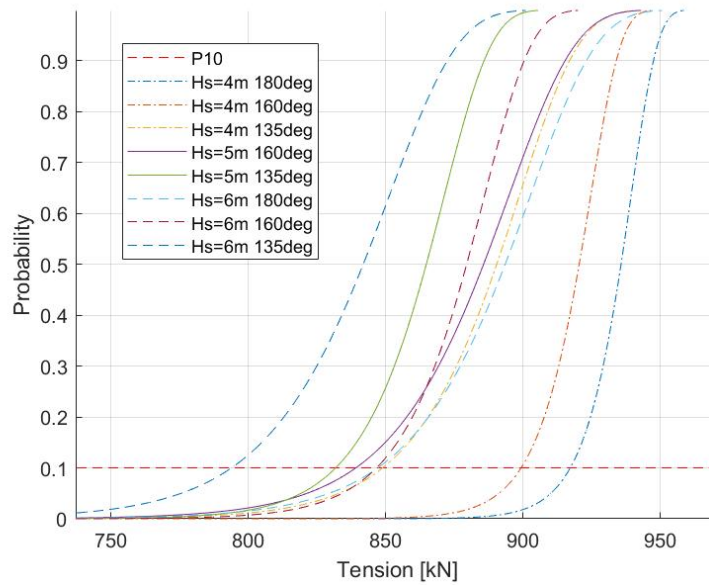


**Figure 10.17:** Deep penetrating anchor extreme minimum distribution (slack crit.=101.5kN).

The 10% quantile of the minimum distributions of the DPA model (Figure 10.17) is especially far away from violating the slack criterion of 101.5kN. The DPA solid shape, and large mass, results in a constant high tension in the crane wire which then avoids slack. The extreme minimum distributions of the SA and DPA show that the slack criterion is not violated for the simulated wave conditions.

### 10.4.2 Extreme Maximum Distributions

The extreme maximum crane wire tension from each simulation is used to create extreme value distributions to identify the 90% fractile. Figure 10.18 - 10.20 shows the results from the suction anchor model for three wave directions relative to the vessel. Here, 1940kN is highlighted because this is the design strength of the crane wire.

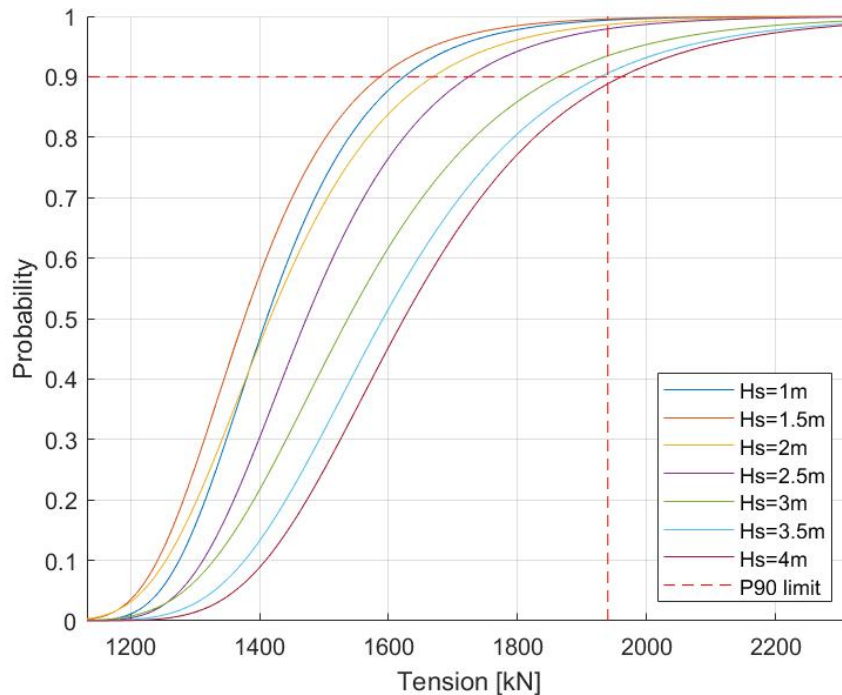


**Figure 10.18:** Suction anchor extreme maximum distribution wave direction 180°.

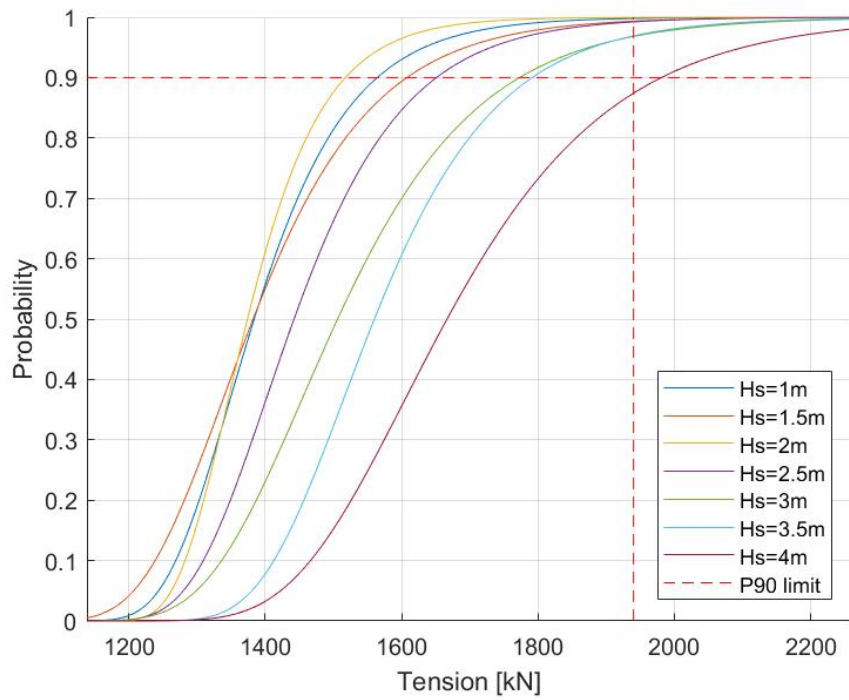


Figure 10.19: Suction anchor extreme maximum distribution wave direction 160°.

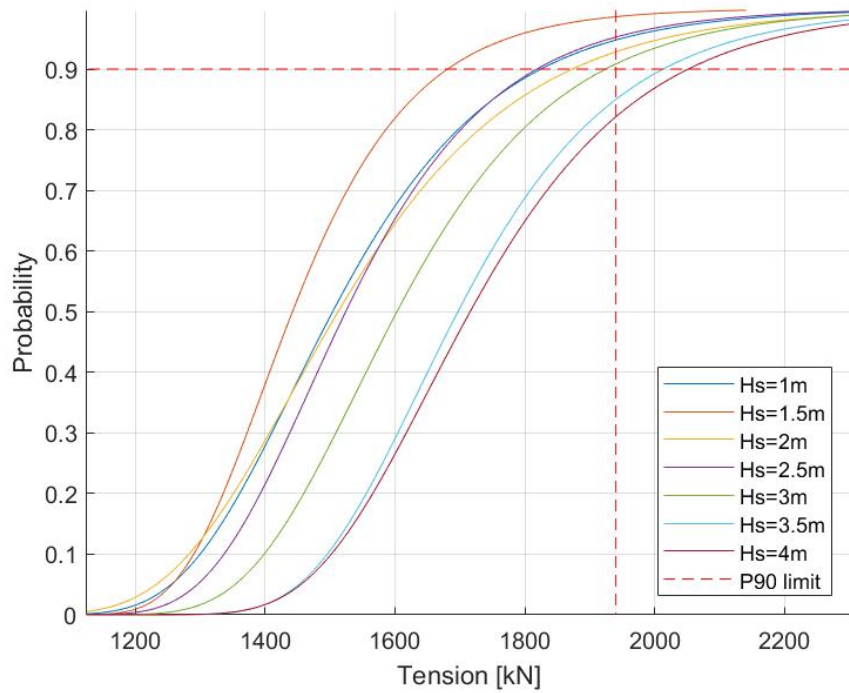
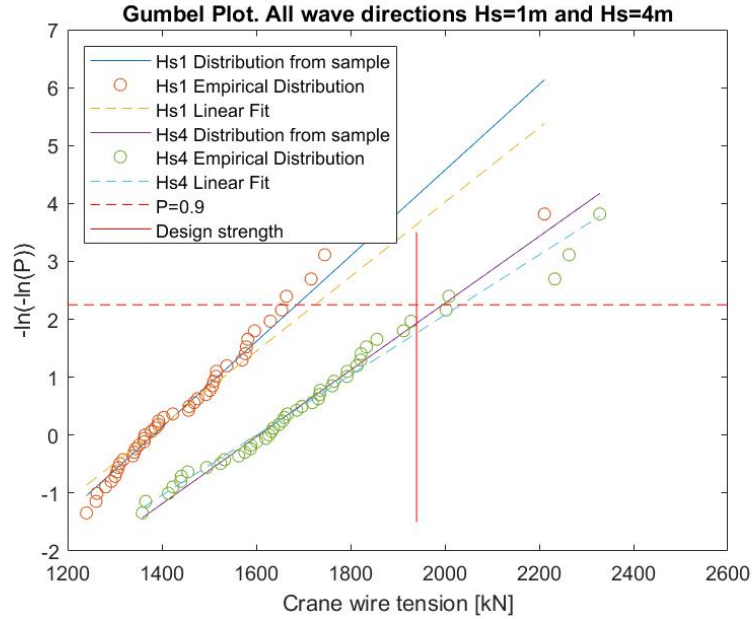


Figure 10.20: Suction anchor extreme maximum distribution wave directions 135°.



**Figure 10.21:** Gumbel plot with  $H_s=1\text{m}$  and  $H_s=4\text{m}$ . Extreme values for all three wave directions plotted.

Figure 10.21 shows the Gumbel plot for the highest and lowest  $H_s$  that is simulated for the SA model with all wave directions.  $H_s$  4m results in overall more substantial crane wire tension, and 5 data points beyond the design strength limit at 1940kN. The importance of the wave period is made visible through the one extreme value for  $H_s$  1m with tension up to 2200kN. This value is way over the 90% fractile and highly unlikely to be surpassed (approximately 2%). There is reason to believe that this value is due to low period direct wave excitation forces, as the condition set with  $H_s$  1m is not expected to induce large crane tip motions. Gumbel plots from other wave conditions and CDF plots for separate peak periods (P5, mean, and P95) are found in Appendix B.

Table 10.1 shows the most probable maxima  $\mu$  from the distributions of the extreme maxima from the simulations with the suction anchor model (Figure 10.18-10.20). The 90% fractile P90 is found in the same table and calculated from Equation 6.8.

**Table 10.1:** Most probable maxima  $\mu$  and 90% fractile P90 from extreme maxima distributions for all wave directions for suction anchor model.

Hs [m]	180°		160°		135°	
	$\mu$ [kN]	P90 [kN]	$\mu$ [kN]	P90 [kN]	$\mu$ [kN]	P90 [kN]
1	1369	1623	1348	1563	1441	1824
1.5	1335	1584	1338	1605	1395	1681
2	1366	1667	1346	1517	1442	1873
2.5	1423	1722	1401	1648	1467	1818
3	1473	1862	1453	1770	1540	1924
3.5	1526	1926	1515	1789	1635	2012
4	1558	1958	1605	1978	1650	2051



Wave direction  $135^\circ$  for the SA model results in the most significant tensions for every condition set. Between wave directions  $180^\circ$  and  $160^\circ$ , there is little difference in P90 tension. Through simulating the SA model with different wave directions, the highest  $H_{sLIM}$  is found with wave direction  $160^\circ$ . Regardless of whether the difference between the P90 seems small, this can have significance on the operability of the marine operation. This is, for example, if the vessel can establish an exact bow direction during the operation.  $H_{sLIM}$  for each wave directions is further included for comparison.

The extreme maximum distributions of the DPA model is also investigated. Same as for the slack criteria, the maximum is not close to violating the upper design strength of the crane wire.  $H_s$  6m and  $135^\circ$  wave direction are the conditions that result in the largest 90% fractile of approximately 1500kN. Hence, the design criteria for the DPA anchor cannot be estimated based on crane wire tension. To exceed the design strength of the crane wire, larger wave conditions must be simulated. Thus, the design criteria for the DPA are determined by other factors, such as safe work conditions for crew or equipment on deck. Table with MPM and P90 values for DPA are found in Appendix B.

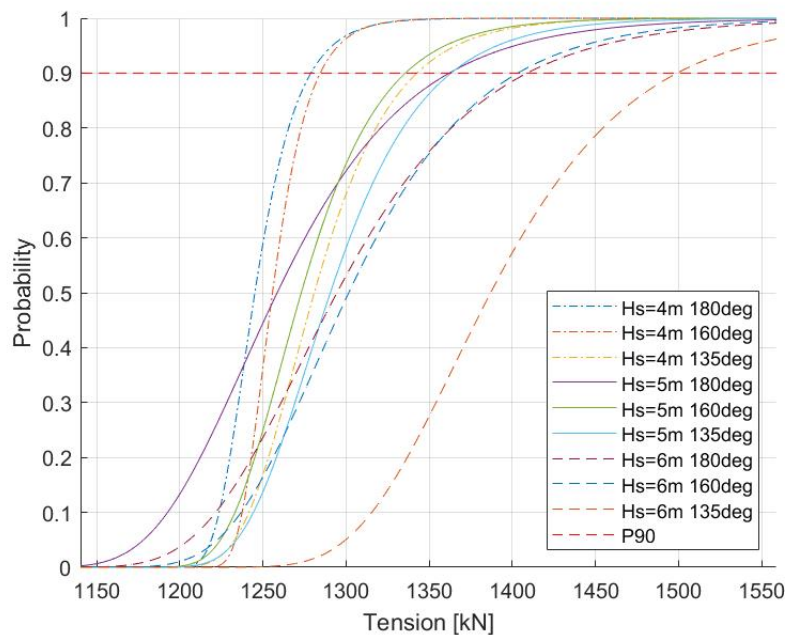


**Figure 10.22:** DPA extreme maximum distributions.

## 10.5 Design Criteria

The simulation results for the SA model show that increased wave conditions challenge the design strength of the crane wire. Table 10.2-10.4 shows all the wave periods that have been run for each significant wave height, where each table represents a wave direction. The colors show which periods exceeded the limit (red) and which remained

below (green). Periods with orange colors led to a 90 % fractile close to the 1940 kN limit.

**Table 10.2:** Wave direction 180°.

Hs [m]	1	1.5	2	2.5	3	3.5	4
P5 peak period [s]	4.8	5.2	5.6	6	6.4	6.8	7.2
Mean peak period [s]	8.4	8.8	9.2	9.6	10	10.4	10.8
P95 peak period [s]	12.9	13.3	13.7	14.1	14.5	14.9	15.3

**Table 10.3:** Wave direction 160°.

Hs [m]	1	1.5	2	2.5	3	3.5	4
P5 peak period [s]	4.8	5.2	5.6	6	6.4	6.8	7.2
Mean peak period [s]	8.4	8.8	9.2	9.6	10	10.4	10.8
P95 peak period [s]	12.9	13.3	13.7	14.1	14.5	14.9	15.3

**Table 10.4:** Wave direction 135°.

Hs [m]	1	1.5	2	2.5	3	3.5	4
P5 peak period [s]	4.8	5.2	5.6	6	6.4	6.8	7.2
Mean peak period [s]	8.4	8.8	9.2	9.6	10	10.4	10.8
P95 peak period [s]	12.9	13.3	13.7	14.1	14.5	14.9	15.3

The design criteria ( $H_{sLIM}$ ) for each wave direction is found from interpolating between the values of the 90% fractiles in Table 10.1. The highest  $H_{sLIM}$  was found from wave direction 160°.

**Table 10.5:** Suction anchor design criteria interpolated from Table 10.1.

Design Criteria	
Wave direction	$H_{sLIM}$ [m]
160°	3.8
180°	3.6
135°	3.1

The DPA design criteria can not be estimated based on the simulation results. This is because when using the same crane and vessel in the simulations for the two different anchor concepts, the contrasts are simply too large for identifying design criteria for the DPA model based on crane wire tension. The design criteria must, therefore, be based on safe working conditions for personnel during the operation. Cutting sea fastenings and attaching the crane wire are limiting factors that depend on the working conditions on the vessel deck and thus the vessel size. It is assumed that the vessel Skandi Acergy can operate safely in significant wave height up to 4.5 meters. The design criteria for the DPA model is, therefore, set to  $H_{sLIM} = 4.5m$ .

## Chapter 11

# Operability and Assessment of Waiting on Weather

The operability of a marine operation is dependent on four important factors. The planned operation period  $T_{pop}$  is estimated based on time assumptions of the duration of the operation. The alpha factor  $\alpha$  is based on the operation category, the design criteria  $H_{SLIM}$ , and  $T_{pop}$ . The contingency period  $T_C$  is set to 50% of  $T_{pop}$ . And then, finally, we have the total design period called reference period  $T_R$ .

The planned operation period is the sum of all the critical phases that make out the marine operation. As seen in Table 11.1, the critical phase is from the last cut sea fastening to the anchor lands on the sea bed. For the suction anchor installation, this is where the next safe condition occurs. The two anchor types have the same total  $T_{pop}$ , but some inequalities in phase duration.  $T_{pop}$  for the DPA operation is set to 6 hours (Shelton (2020)). It is assumed that the saved operation time due to the DPA drop is compensated by the time it takes for vessel positioning and preparations before anchor drop.

**Table 11.1:** Phases together with total  $T_{pop}$  for SA and DPA.

Phase	Suction Anchor	Deep Penetrating Anchor
Pre-survey of target box in parallel with cutting sea fastenings.	2 hours	2 hours
Lift off and through splash zone	2 hours	2 hours
Lowering	1 hour	0.5 hour
Positioning and landing	1 hour	1.5 hours
$T_{pop}$	<b>6 hours</b>	<b>6 hours</b>

Using Table 2.2 taken from *DNV-OS-H101: Marine Operations, General*, the alpha factors is found by interpolation. Since the significant wave height design criterion's (Table 10.5) are different for the wave directions for the suction anchor, the respective directions gets unique alpha factors. Finally the  $H_s$  operational criterion  $H_{SWF}$  is calculated by Equation 2.1 from multiplying  $\alpha$  with  $H_{SLIM}$ . The results can be seen in Table 11.2. The  $H_{SWF}$  for the DPA is 3.74 meters, which is 0.64m higher than the highest SA limit.

**Table 11.2:** Design criterion  $H_{SLIM}$ , alpha factor  $\alpha$  and Operational criterion  $H_{SWF}$  for the crane operations.

		$H_{SLIM}$	$T_{POP}$	$\alpha$	$H_{SWF}$
SA	135°	3.1 m	6 hours	0.816	2.53 m
	180°	3.6 m	6 hours	0.824	2.90 m
	160°	3.8 m	6 hours	0.827	3.10 m
DPA		4.5 m	6 hours	0.832	3.74 m

We recall that the operation reference period  $T_R$  is the total operational period that the operation is designed for. This period is found from Equation 2.2 where  $T_{pop}$  is given some added contingency time for considering uncertainties in the operation period. Here,  $T_{pop}$  is 6 hours, which results in a contingency time of 3 hours. The reference period is then set to 9 hours for both anchor types.

The expected duration of the operations will hence vary because of the different operational criteria  $H_{SWF}$ . The durations are found using data from Ocean4cast.com and described in the following section.

## 11.1 Ocean4cast

Ocean4cast data covers more than 60 years of meteorological data stretching from the coast of France in the south to Greenland, Svalbard, and the Barents Sea in the north. The data contain information about wind, sea waves, and swell and are measured every three hours at 50 000 locations since 1957 (4subsea (2015)).

The data is downloaded by requesting a geographical position and choosing the closest location. For the data in this thesis, the requested position is latitude: 61.44 and longitude: 2.30. The closest hindcast data location was given from latitude: 61.44 and longitude: 2.25. All information given from Ocean4cast is accessed through the supervisor as this website demand a subscription.

The hindcast data used to plot Figure 9.2 in the determination of the wave conditions comes from Ocean4cast. Ocean4cast is used to estimate the different probabilities of the duration of the four different installation scenarios.

In the operation duration analysis,  $H_{sWF}$  and  $T_R$  is inserted. The algorithm calculates the duration in days, which for a 9-hour operation is 0.38 days. For each month of the year, the algorithm calculates the mean, P10, P50, and P90 duration's for operating. If a P90 duration for March shows 5.25 days, it is 10% probability that the 9-hour operation may take over 5.25 days in March.

Figure 11.1 shows how the total duration is calculated. Every third hour in the 62-year long data set is analyzed, and the duration of the operation with the given boundaries ( $H_s$  and  $T_R$ ) is analyzed. At  $t_1$ , the waiting time will be zero, and the 9-hour operation will take 9 hours. At  $t_2$ , there will be approximately 10 hours of waiting time before the operation can be initiated, and the duration will be 19 hours. The duration results from Ocean4cast is a result of thousands of starting points from each month. With eight measurements a day for 62 years yields a total of approximately 13 800 data points.

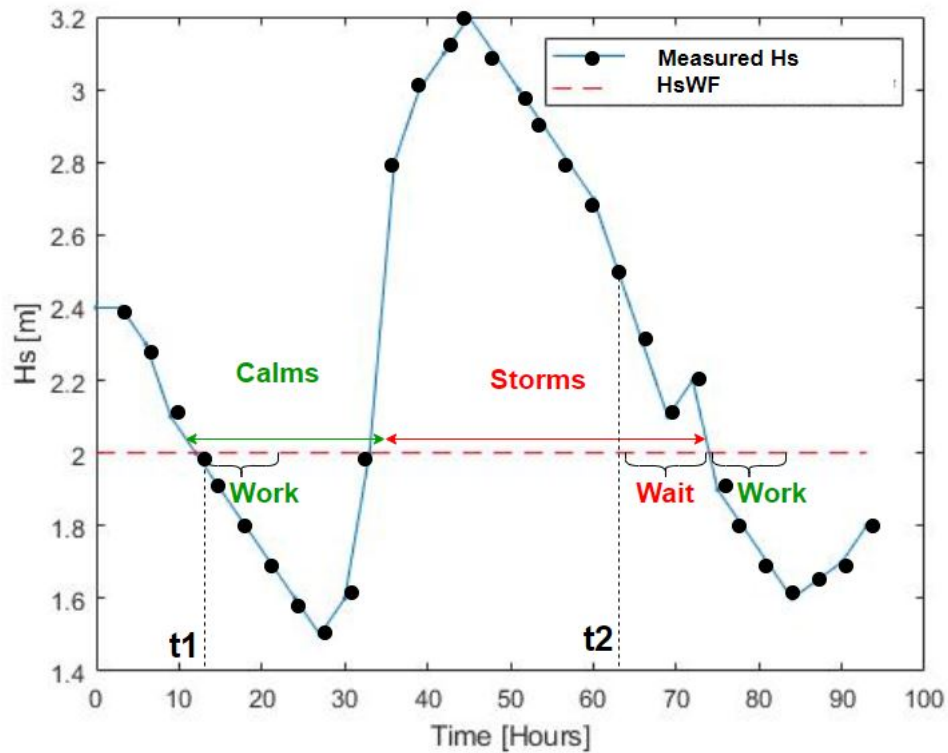


**Figure 11.1:** Estimation of operation duration. Total duration at start  $t_1$  and  $t_2$  is 9 hours and 19 hours respectively.

## 11.2 Operability investigation

In Figure 11.2, the season varying  $H_s$  is plotted from 1957 to 2019 based on the given hindcast data from Ocean4cast.com. The peaks are due to seasonal variations in the environmental conditions.

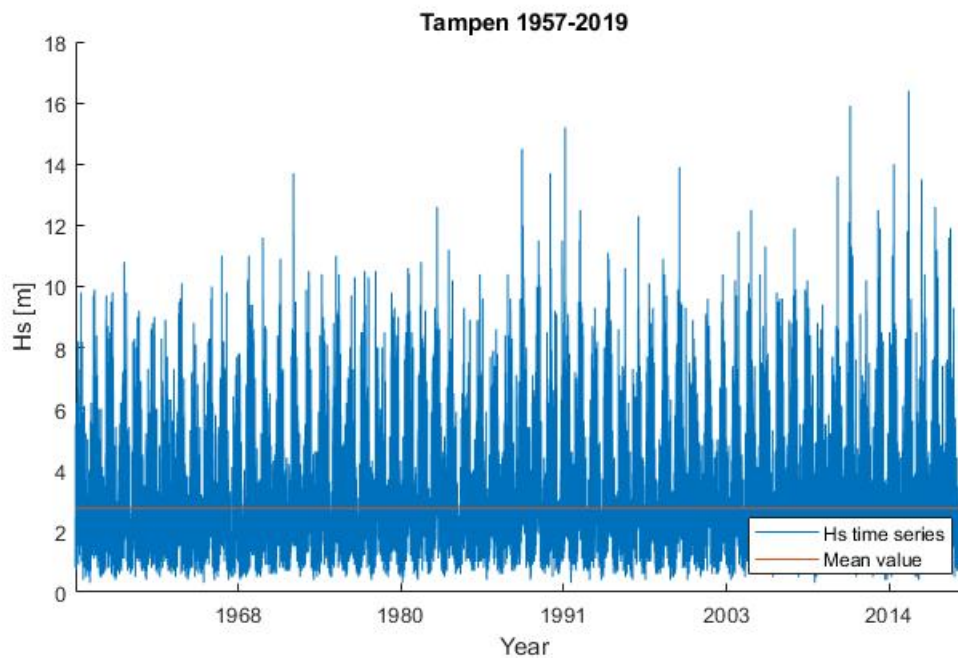


**Figure 11.2:**  $H_s$  as a function of time Tampen area 1957-2019.

From the Weibull probability paper (Figure 6.10, Section 6.3), it is assumed that the sample of measured  $H_s$  follows the Weibull distribution. Figure 11.3 shows the PDF and CDF of all measured  $H_s$  at the Tampen area in the given time interval. From this, the probability that  $H_s$  is lower than the operational criteria  $H_{SWF}$  from all measured  $H_s$  is presented in Table 11.3.

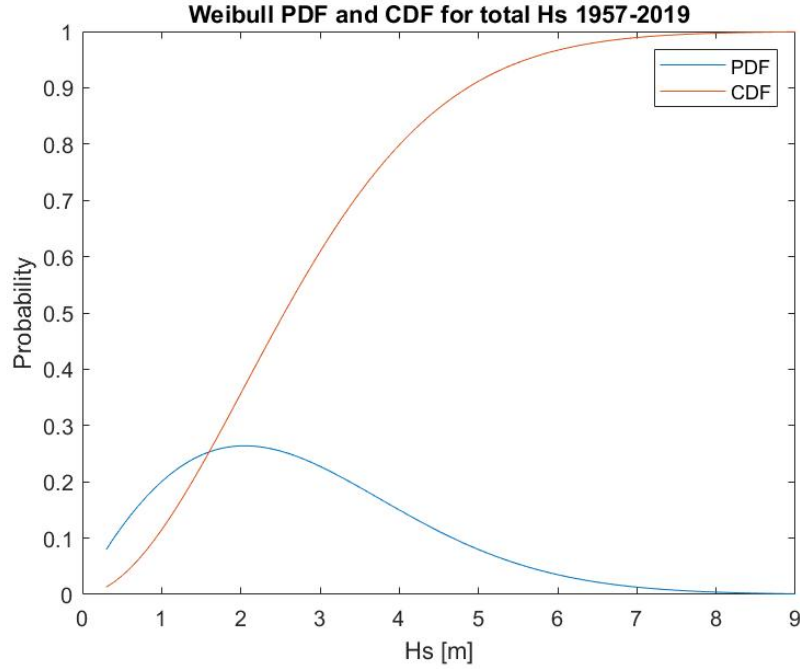


**Figure 11.3:** Weibull PDF and CDF for  $H_s$  Tampen 1957-2019.

**Table 11.3:** Probability that measured  $H_s$  is lower than the operational criteria.

		$H_{SWF}$ [m]	$H_s < H_{SWF}$
SA	135°	2.5	48%
	180°	2.9	59%
	160°	3.1	63%
DPA		3.74	75%

The data in Table 11.3 shows that the DPA installation has the potential of being performed 75% of the total measured time. By lowering the  $H_{SWF}$  to 3.1m for the 160° wave direction SA installation, the total operability is reduced with 12% to a operability of 63%. However, the total operability over the years only provides an insight to the operability for the different limits. As seen in Figure 11.3, the distribution is stretched to the right. This is because of the extreme weather conditions during the winter seasons. The seasonal variation is essential to assess because the environmental conditions usually are calmer during the summer season. The study of operation duration with seasonal variation is done in the following subsection.

### 11.2.1 Duration of Operations

To find the time during the year, the operation can be performed with the least expected duration, is useful in the planning process as this impacts costs significantly. The vast seasonal variations in the North Sea makes operations with low operational limits challenging to perform within the reference period of 9 hours during some parts of the

year.

The duration's are based on operation start the 15th day of each month. This is the basis for choosing the season and its respective months (Table 11.4).

**Table 11.4:** Seasons and respective months.

Season	Months
Winter	December - February
Spring	March - May
Summer	June - August
Autumn	September - November

Figure 11.4 to 11.7 shows the duration of the operations in hours for different months. The duration from Ocean4cast is calculated in days with two decimal points. This means that the 9 hour  $T_R$  is presented as 0.38 days instead of the more accurate 0.375 days. However, this is a conservative approach with an increase of 1.3% in  $T_R$  (7 minutes). The mean and P50 duration differ due to some operations with a long duration. This makes the distribution skewed to the right and results in inequalities between the mean and P50 duration.

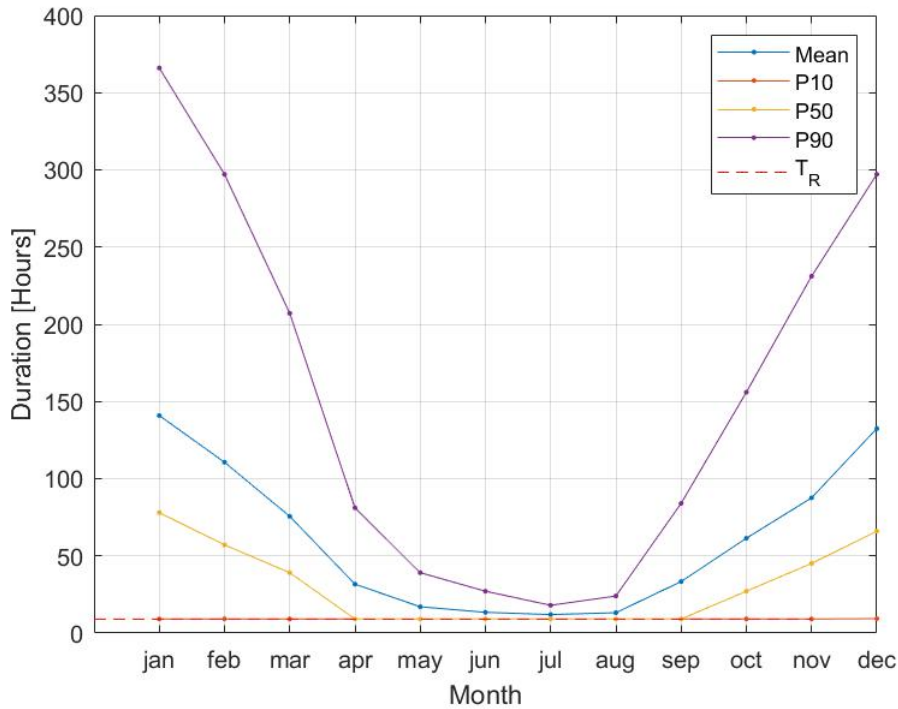


**Figure 11.4:** Monthly duration SA 135°  $T_R=9$ hours,  $H_{sWF}=2.53$ .



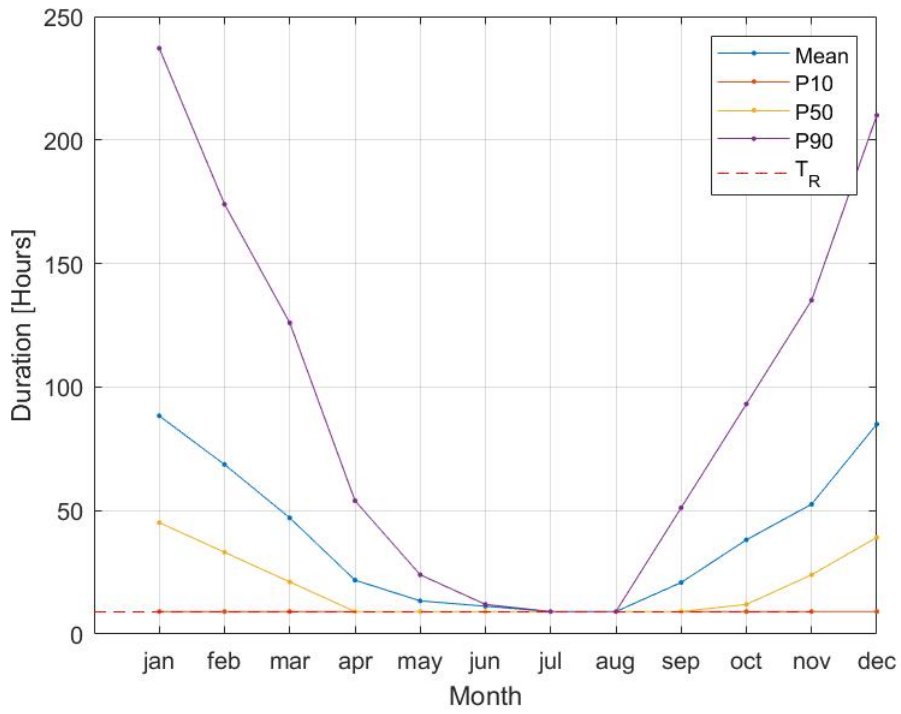


Figure 11.5: Monthly duration SA 180°  $T_R=9$ hours,  $H_{SWF}=2.90$ m.

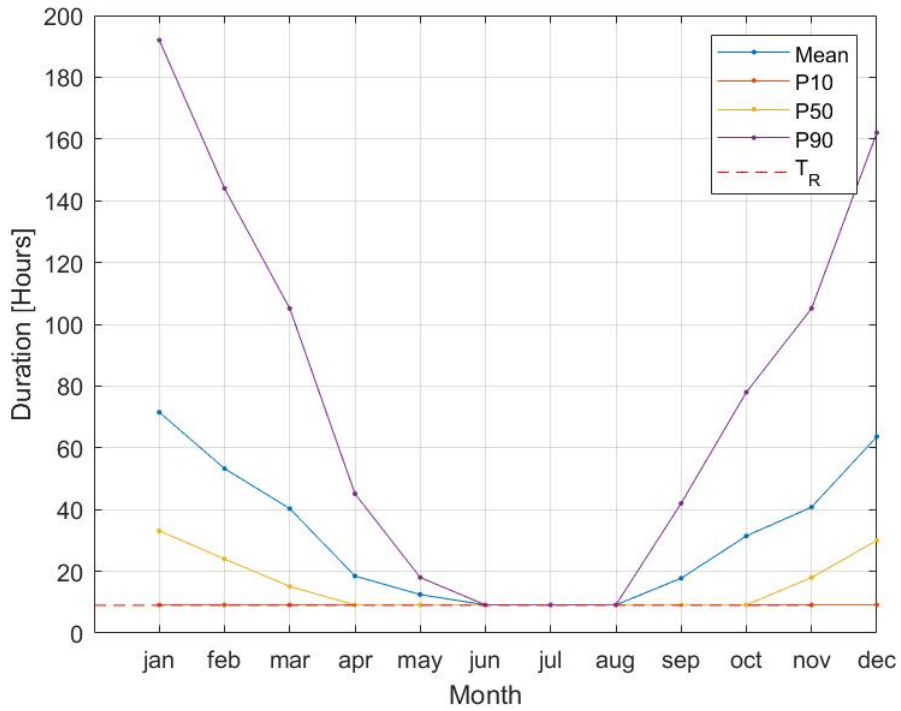
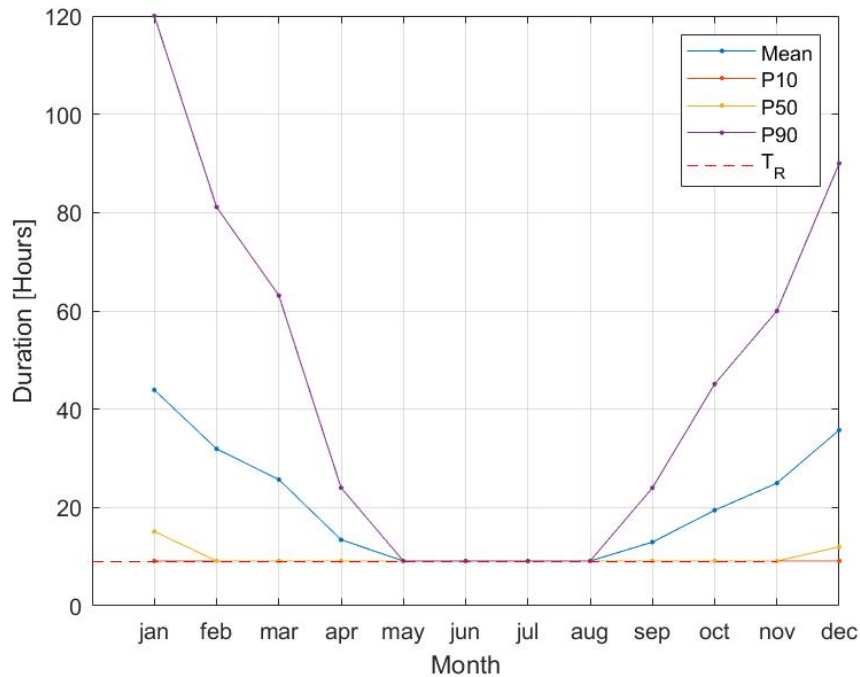


Figure 11.6: Monthly duration SA 160°  $T_R=9$ hours,  $H_{SWF}=3.10$ m.



**Figure 11.7:** Monthly duration DPA  $T_R=9$ hours,  $H_{SWF}=3.74$ m

Weather windows should be conservatively assessed based on worst-case scenarios (DNV-GL (2011a)). The summer months allow performing most of the scenarios with a 90% probability of no waiting on weather. The exception is the  $135^\circ$  SA installation. This is visualized where the P90 curves converge towards  $T_R$  from June to August. The DPA operation (Figure 11.7) has a 50% probability of being performed without waiting on weather (WoW) from February to November. The highest  $H_{SWF}$  for the SA can, with the same probability, be performed from April to October (Figure 11.6).

The curves show a significant decrease in the P90 duration from January to April and towards the summer. From August to September, the P90 duration is increased significantly. The P10 probability shows that for all the scenarios, there is a 10% probability of operating without WoW in any month, not the greatest of odds. The DPA can be installed with a 90% probability of no WoW from May to August.

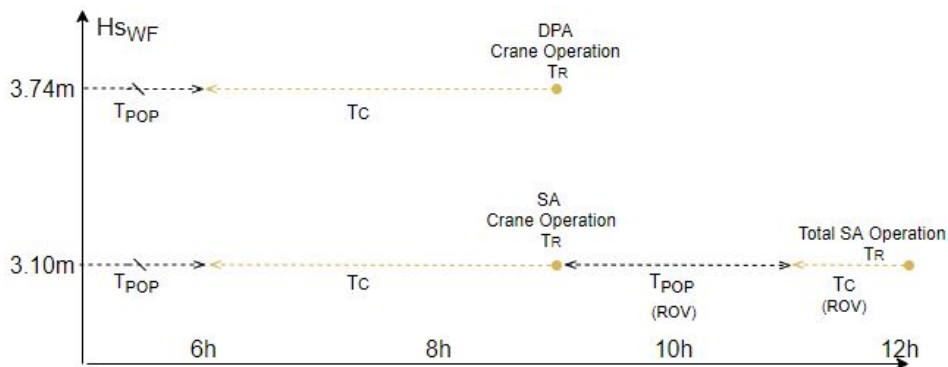
In Table 11.5, the average duration from the months representing a season is calculated. The results from the operability assessment shows that if the vessel can maintain a wave direction of  $160^\circ$  or  $180^\circ$  and perform the lift during the summer months, the difference in duration is not significant compared to the DPA. The  $160^\circ$  SA and the DPA crane operation have a 20% difference in  $H_{SWF}$  but can be performed with identical duration during the summer months.

**Table 11.5:** Duration of operation at Tampen. All duration's given in hours.  $T_R = 9$  hours.

Case	Probability	Winter	Spring	Summer	Autumn
SA Wave direction 135° $H_{SWF} = 2.53m$	Mean	128	42	13	61
	P10	9	9	9	9
	P50	67	19	9	27
	P90	319	109	23	157
SA Wave direction 180° $H_{SWF} = 2.90m$	Mean	80	27	9	37
	P10	9	9	9	9
	P50	39	13	9	15
	P90	207	68	10	93
SA Wave direction 160° $H_{SWF} = 3.10m$	Mean	62	24	9	30
	P10	9	9	9	9
	P50	29	11	9	12
	P90	166	56	9	75
DPA $H_{SWF} = 3.74m$	Mean	37	17	9	19
	P10	9	9	9	9
	P50	12	9	9	9
	P90	96	32	9	43

It is noted that there is a difference between the crane operation and the installation of the anchors. For the DPA, the crane operation itself is a large part of the entire installation process. However, for the SA, the operation is not finished when the SA is placed on the sea bed. The SA needs to be penetrated into the seabed by pumping out entrapped seawater with an ROV. This phase has the advantage of slacking in the crane wire, so the  $H_{SWF}$  is not decided by crane wire tension but by the working conditions for the ROV. It is assumed that the operation regarding launching and retrieval of the ROV holds the same  $H_{SWF}$  as the 160° crane operation ( $H_{SWF} = 3.1m$ ).

An analysis of the total SA installation with  $T_R$  equal to 12 hours is therefore performed. It is assumed that the operation must be done continuously without stopping with an ROV  $T_{POP}$  equal to 2 hours (Figure 11.8).

**Figure 11.8:**  $T_R$  for total SA installation compared to DPA.

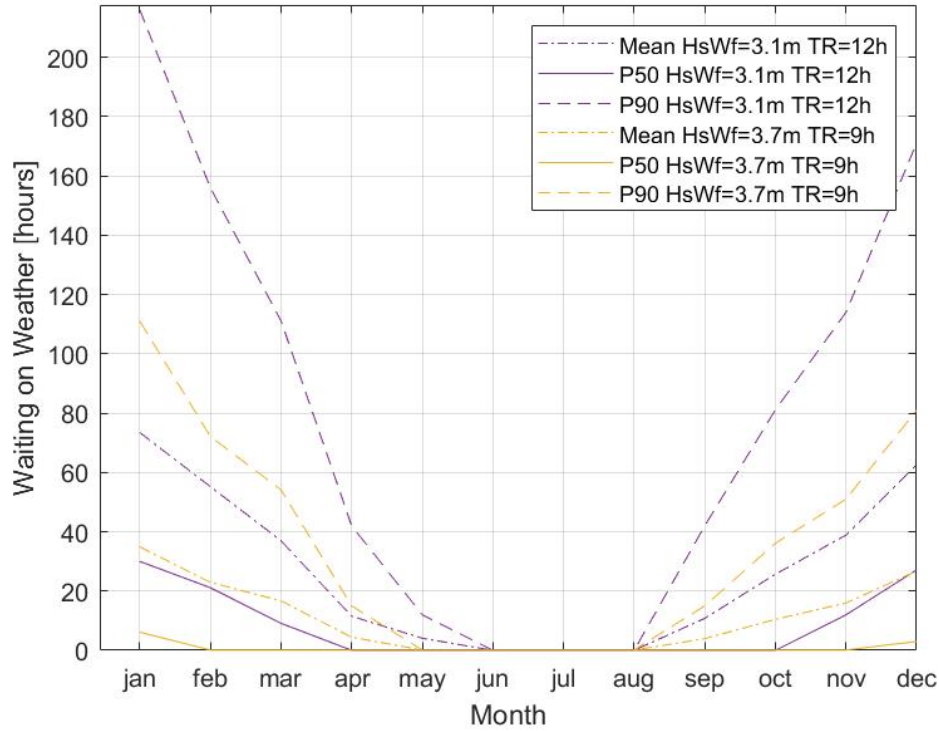


**Figure 11.9:** Monthly probabilities of WoW for Total SA (purple) and DPA (yellow) installation.

WoW is plotted on the y-axis for comparison of the different  $H_{sWF}$  and  $T_R$  (Figure 11.9). The DPA P50 WoW reaches 0 in February, which lasts to November. The SA installation can, with the same probability, be performed without WoW from April to October. The differences in the P90 is significant, especially in the winter months. Both the mean and P90 probability reach zero WoW in May for the DPA. The same probabilities reach zero a month later for the SA. The differences in the mean probability yields the differences in the spread of the distribution. The SA has a higher mean in the winter, spring, and autumn months than the DPA, which is a result of some operations with considerable duration. A large upswing in WoW is expected in the transition between August and September. The spring months (Mar, Apr, and May) offers less probability of WoW compared to the autumn months (Sep, Oct, and Nov).

Based on the study of an operational limit from crane wire tension, the DPA holds the critical advantage of being installed at a higher  $H_{sWF}$ . The difference between the DPA and SA installation becomes even greater by considering differences in  $T_R$ . It is noted that the DPA duration in this thesis is estimated from a lift over-the-side for comparison of the crane operation. The DPA can also be installed over the stern by a winch, which by further investigation, may contain a higher  $H_{sWF}$  and lower  $T_R$ . Thus the differences in WoW could be even more significant.

# Chapter 12

## Conclusion

Two possible anchor concepts for the mooring of floating wind turbines is the suction anchor (SA) and the deep penetrating anchor (DPA). A comparison of the crane operation for installing a SA and a DPA was performed to establish operational limits in terms of significant wave height ( $H_s$ ). This was done to assess the operability of the two different installations for comparison.

In the construction of the simulation models, the depth-dependent coefficient was necessary for the crane operation, as the lifted objects go from an environment in the air to water. This was done with slender element for the anchor models. Both anchors were given a mass of 110 tons and a length of 12m. Diameter of the SA and DPA was 5m and 1.3m respectively.

It was found that with increased wave condition, one must expect more significant vertical crane tip motion, and this will result in more enormous tensions in the crane wire. Although increased  $H_s$  increases the vertical movement, so will the direct wave excitation forces. When the anchor is lowered beneath the wave energy area, the crane tip motions are the only force contribution for the crane wire. Low wave periods induce negligible vessel motions and significant direct wave excitation forces.

The results from the SA model show a lot of tension dynamics through the splash zone. This may be because of large inertia forces from direct wave excitation, and large added mass. When the anchor top was fully submerged (after 114s), significant slamming impulses were detected for the SA model, where full vertical added mass of 277 000 kg was activated. The shape of the DPA results in less crane wire tension dynamics.

The operational criterion  $H_{SWF}$  was investigated based on extreme values from crane wire tension. The maximum and minimum tension was set to the hoisting wire design strength and DNV-GL's slack criterion, respectively. The wave condition where the 90% fractile of the Gumbel distribution of the extreme crane wire maximums surpassed the

design strength of the crane wire, was set as the design criterion  $H_{sLIM}$ . This was because, for both anchors, the slack criterion was never violated for any of the wave conditions.

Vessel heading  $160^\circ$  proved to contain the highest  $H_{sLIM}$  for the SA model at 3.8m. For the DPA, the  $H_{sLIM}$  could not be based on crane wire tension, as the P90 extreme was far away from surpassing the upper and lower criteria. The  $H_{sLIM}$  for the DPA was set to 4.5m based on safe working conditions on deck.

The operation reference period was estimated at  $T_R = 9h$  for both crane operations. The operability assessment for the SA was done with an increase in  $T_R$  to 12 hours due to the ROV pumping operation. With the respective alpha factors, this resulted in a  $H_{sWF}$  of 3.1m for the SA and 3.74m for the DPA.

An assessment of operation duration and waiting on weather (WoW) were performed based on the probability of duration for different months. The results shows that the operability is season-dependent. The P90 probability of the SA shows that the operation can be performed in June - August with no WoW. During November-Mars, the 9-hour operation had a P90 probability of a 100-190 hour duration. The P90 probability of the DPA showed no WoW from May-August, and overall lesser WoW throughout the year. Baed on the assessment of operability in this thesis, the results suggest that the DPA can be installed more cost-efficiently than the SA.

## 12.1 Source of Errors

- A model simulating physical phenomenons will always contain errors. The assumptions in this thesis is based on e-mail correspondence with professionals and intended to make consistent results.
- The entrapped air of the suction anchor can create large buoyancy if the relative vertical motion between SA and the waves is high. Depending on the perforation, if the air is not evacuated fast enough and the SA is suddenly submerged, slack in the crane wire might occur. In this thesis, It is assumed that there is an equal water level inside and outside the anchor.
- The vertical linear damping of the SA is found from experimental results. The vertical damping used in this thesis is found from a SA that is 2 meters longer but with the same diameter.
- The simulated wave conditions are found in the Tampen area. The peak periods in the simulation is set to the P5, mean, and P95 probabilities from each  $H_s$ . This might result in an unfair description of the wave periods. As each peak period is run with the same seed, and the mean period is more likely to occur.
- The number of seeds for the simulations is in this thesis set to 5 for each  $T_p$ . More accurate results may be achieved by increased seed number. This results in

---

increased computational time for results.

- The DPA may be installed more efficiently with a winch over the stern. The operational criterion for such a marine operation is not investigated.
- Wind and current loads are not included in this thesis. Current forces should be assessed for the total installation as currents might be present at deep water. Object with large projected areas might be exposed to wind forces before going through the splash zone.
- The rigging slings consist of the same characteristics as the hoisting wire. The slings should generally be given its own comprehensive set of safety factors (DNV-GL (2011b)).

## 12.2 Recommendations for Further Work

According to Ølund Bertelsen (2014), small perforation ratios in the SA top plate, will induce large buoyancy force when lowered through the splash zone, which may lead to tilting of the anchor and slack in the hoisting wire. This is regarding the evacuation of the entrapped air inside the SA. This phenomenon is not considered in the thesis model. This is an important source of error that should be further investigated when studying the slack criterion. Studies of modeling this phenomenon should be performed.

The results from the simulations with the DPA show that wave conditions up to  $H_s$  6m did not violate the design strength of the crane wire. The highest P90 probability of the extreme maximums was 1500kN. The DPA may not need as expensive installation vessels as the suction anchor, with several hundred tons in crane capacity. This could be further investigated in regards to costs.





# Bibliography

- 4subsea, 2015. *4Subsea Introduction to Ocean4Cast*. [https://www.youtube.com/watch?v=e1T\\_3p--Xi8](https://www.youtube.com/watch?v=e1T_3p--Xi8). Obtained: 25.05.2020.
- ABC-Moorings, 2019. *Moorings Systems*. Available at: <https://abc-moorings.weebly.com/moorings-systems.html>. Obtained: 10.02.2020.
- Aubeny, C., 2016. *Performance of Anchors for Floating Offshore Windfarms* .
- AXTech, 2020. *420t Special Handling System*. <http://www.axtech.no/system-solutions/420t-special-handling-system/>. Obtained: 25.02.2020.
- Bai, Y., Jin, W.L., 2016. Chapter 10 - offshore soil geotechnics, in: Bai, Y., Jin, W.L. (Eds.), *Marine Structural Design (Second Edition)*. Butterworth-Heinemann, Oxford, pp. 181 – 195.
- Ølund Bertelsen, T., 2014. Ntnu master thesis - *Installation of large subsea structures*.
- Bourbon Offshore, 2020. *The moonpool; a safety asset*. <https://www.bourbonoffshore.com/en/offshore/moonpool-safety-asset>. Obtained: 12.02.2020.
- Bridon-Bekaert, 2020. Bridon-bekaert the ropes group. <https://www.bridon-bekaert.com/en-gb>. Obtained: 15.03.2020.
- Chakrabarti, S.K., 2005. *Handbook of Offshore Engineering*. Oxford: Elsevier Science & Technology.
- Deepsea anchors, 2019. *Principles of Concept - Deep Penetrating Anchor*. <http://www.deepseaanchors.no/principles-of-concept/>. Obtained: 11.02.2020.
- Delmar, 2020. Gravity installed anchor *The OMNI-max*. Obtained: 19.02.2020.
- DNV-GL, 2011a. DNV-OS-H101 *Marine Operations, General*.
- DNV-GL, 2011b. DNV-RP-H103 *Modelling and Analysis of Marine Operations*.
- DNV-GL, 2014. DNV-OS-H205 *Lifting operations*.
- DNV-GL, 2016a. DNVGL-ST-N001 *Marine Operations and Marine Warranty*.

- 
- DNV-GL, 2016b. DNVGL-ST-N001 *Standard for offshore and platform lifting appliances*.
- DOF, 2013. *Skandi Acergy*. <http://www.dof.no/en-GB/DOF-Fleet/CSV/Skandi-Aceryg>. Obtained: 14.04.2020.
- DOF, 2019. Drawing: *Hywind Tampen EPCI WP-1 Marine Operations, Skandi Skansen Anchor installation*. Obtained: 1.11.2019.
- Equinor, 2018. *Hywind Tampen - Forslag til utredningsprogram for konsekvensutredning*. Obtained: 14.04.2020.
- Equinor, 2019. *Hywind Tampen*. <https://www.equinor.com/no/how-and-why/impact-assessments/hywind-tampen.html>. Obtained: 11.02.2020.
- Faltinsen, O.M., 1990. *Sea Loads on Ships and Offshore Structures*. Cambridge: Cambridge University Press.
- Greco, M., (2019). TMR 4215: Sea Loads. Lecture Notes. *TMR 4215 Sea Loads*. Available at: <https://ntnu.blackboard.com>. (Accessed: 20. January 2020).
- Halse, K.H., 2019. Anchor Handling - Planing and performing. *TMR4225 Marine Operations NTNU*. <https://ntnu.blackboard.com>.
- Hansen, O.H., 2013. *Skandi Skolten m/sugeanker Hammerfest 2013*. <http://www.oddharry.com/412434068?i=97747957>. Obtained: 1.03.2020.
- Hove, F., 2001. *Deep Penetrating Anchor vs Suction Anchor - Installation Methodology with Cost and Schedule Estimates*.
- Jørdre, G., 2020. E-mail correspondence with Geir Jørdre (DOF).
- Larsen, K., 2019a. Crane Operations and Subsea Lifting. *TMR4225 Marine Operations NTNU*. <https://ntnu.blackboard.com>.
- Larsen, K., 2019b. Introduction and Planning of Marine Operations. *TMR4225 Marine Operations NTNU*. <https://ntnu.blackboard.com>.
- Larsen, K., 2019c. Operability and Weather Windows. *TMR4225 Marine Operations NTNU*. <https://ntnu.blackboard.com>.
- Larsen, K., 2019d. Station Keeping and Mooring. *TMR4225 Marine Operations NTNU*. <https://ntnu.blackboard.com>.
- Larsen, K., 2020. Personal communication with Adjunct Professor Kjell Larsen.
- Leira, B., 2019. Probabilistic models for stochastic physical variables. *TMR4235 Stochastic variables of sealoading NTNU*. <https://ntnu.blackboard.com>.
- Lieng, J.T., 2020. E-mail correspondence with Jon Tore Lieng.

- 
- Ma, K.T., Luo, Y., Kwan, T., Wu, Y., 2019. Chapter 11 - installation, in: Ma, K.T., Luo, Y., Kwan, T., Wu, Y. (Eds.), *Mooring System Engineering for Offshore Structures*. Gulf Professional Publishing, pp. 215 – 232.
- MathWorks, 2020. *Weibull Distribution*. <https://se.mathworks.com/help/stats/weibull-distribution.html>. Obtained: 25.03.2020.
- NRK, 2020. *Jubel og kritikk for milliardatsing på havvind - Julianne Bråten Mossing*. <https://www.nrk.no/vestland/utbygging-av-hywind-tampen-er-godkjent-1.14977920>. Obtained: 08.04.2020.
- Rausand, M., 2014. *Reliability of Safety-Critical Systems: Theory and Applications*. Wiley.
- Sandvik, P.C., Solaas, F., 2017. *Hydrodynamic coefficients for suction anchors during installation operations*. Obtained: 1.10.2019.
- Shelton, J., 2020. E-mail correspondence with John Shelton (Delmar Systems, Inc).
- SINTEF Ocean, 2019a. *SIMO 4.16.2 Theory Manual*. Obtained: 02.01.2020.
- SINTEF Ocean, 2019b. *SIMO 4.16.2 User Guide*. Obtained: 02.01.2020.
- Skipsrevyen, 2018. *M/S "Skandi Acergy"*. <https://www.skipsrevyen.no/batomtaler/m-s-skandi-acergy/>. Obtained: 15.04.2020.
- Solaas, F., 2020. *Numerical modelling of a suction anchor*. Obtained: 3.11.2020.
- Offshore Magazine*, 2007. World's largest suction anchors installed offshore boston. <https://www.offshore-mag.com/production/article/16760849/worlds-largest-suction-anchors-installed-offshore-boston>. Obtained: 31.10.2019.
- T.Næss, Havn, J., Solaas, F., 2014. *On the importance of slamming during installation of structures with large suction anchors*. Obtained: 1.10.2019.
- Vryhof, 2010. *Vertical Load Anchor*. [http://www.vryhof.com/pdf\\_2010/VRYHOF-STYLE201020Brochure20Stevmanta20lowres.pdf](http://www.vryhof.com/pdf_2010/VRYHOF-STYLE201020Brochure20Stevmanta20lowres.pdf). Obtained: 10.02.2020.
- Weebly, 2019. *Anchoring Systems*. <https://floatingwindfarm.weebly.com/anchoring-systems.html>. Obtained: 10.02.2020.
- WikiWaves, 2012. *Ocean-Wave Spectra*. [https://wikiwaves.org/Ocean-Wave\\_Spectra](https://wikiwaves.org/Ocean-Wave_Spectra). Obtained: 27.02.2020.



## Appendix A

# Vessel First Order Motion Transfer Functions

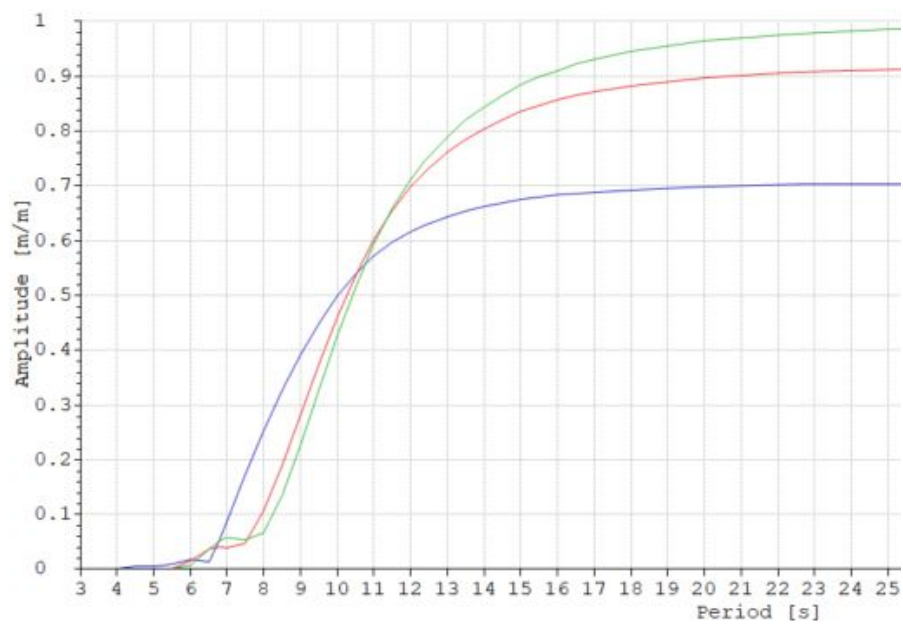
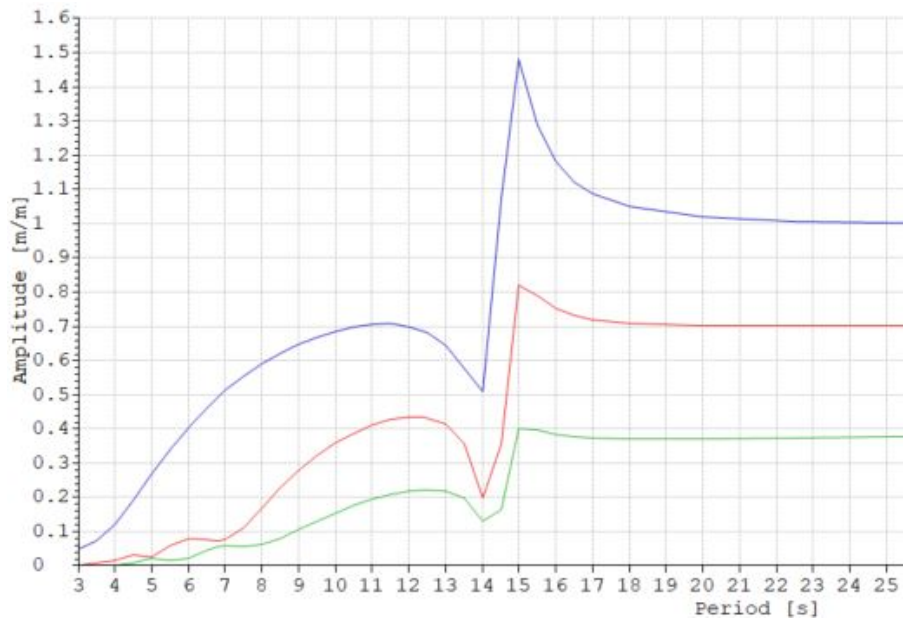
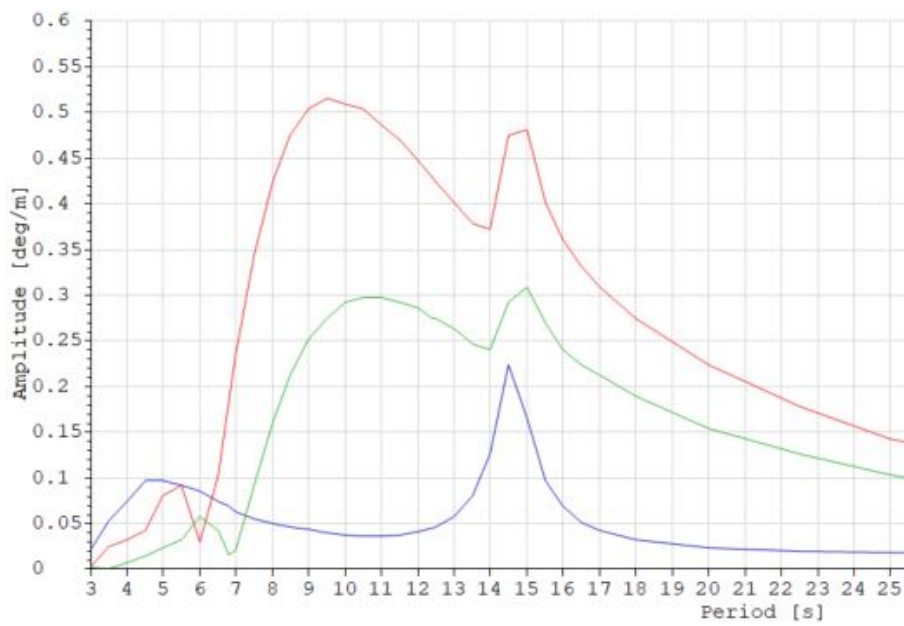


Figure A.1: Vessel Surge RAO. Green=180°, red=158°, blue=135°.



**Figure A.2:** Vessel Sway RAO. Green=158°, red=135°, blue=90°.



**Figure A.3:** Vessel Yaw RAO. Green=158°, red=135°, blue=90°.

# Appendix B

## Statistics

Figure B.1-B.3 shows Gumbel plots for SA crane operation with all wave directions for each  $H_s$ .

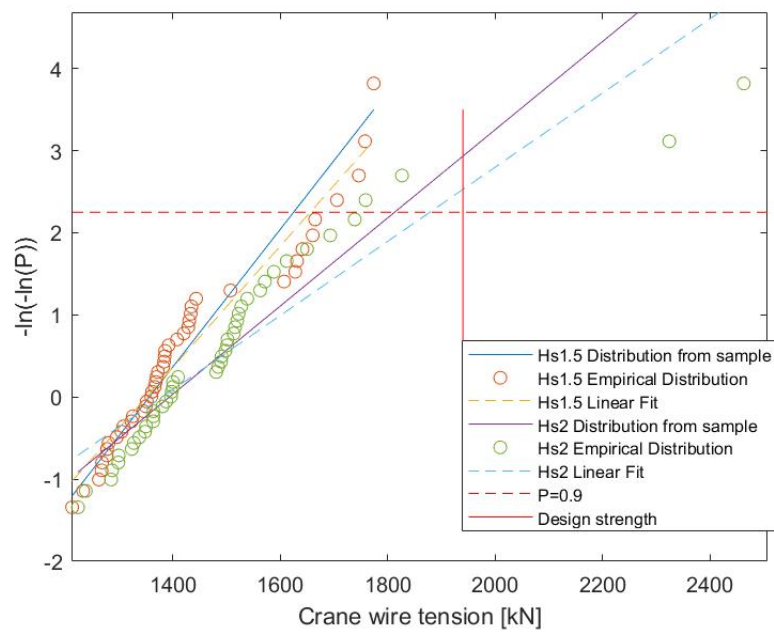
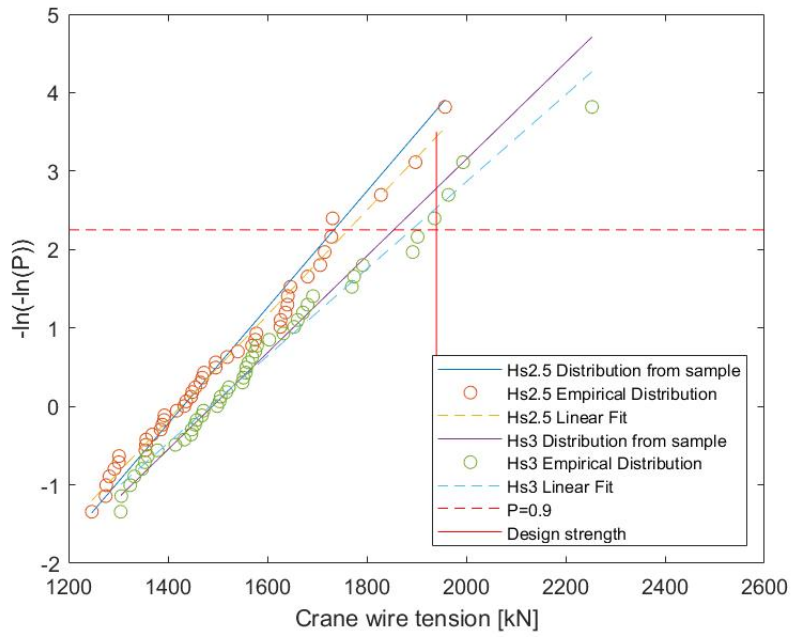
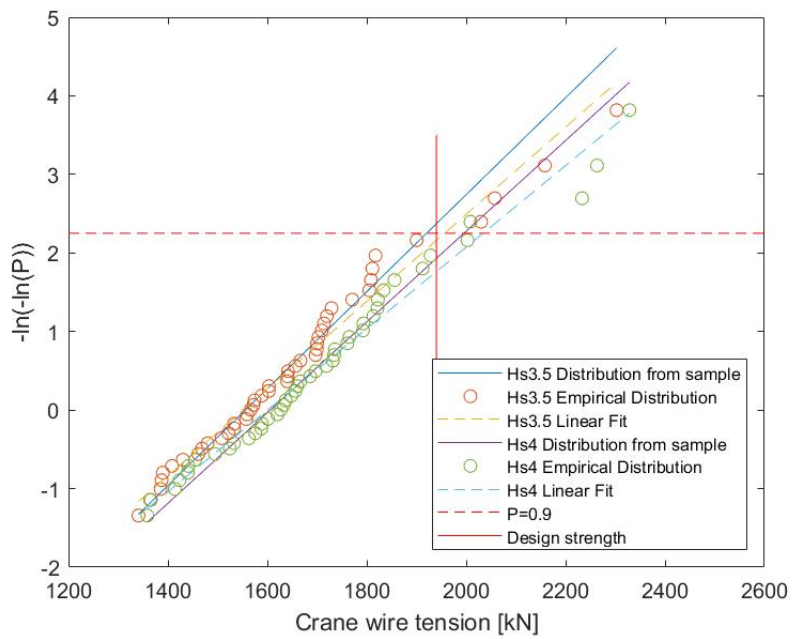


Figure B.1: Gumbel plot for all wave directions.



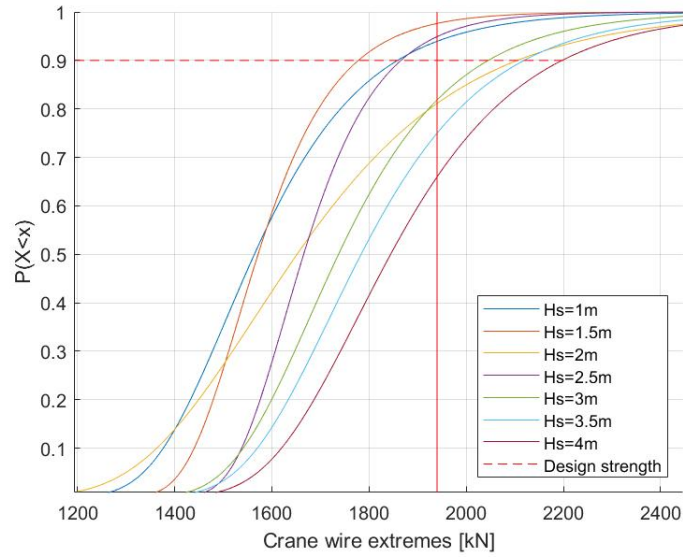
**Figure B.2:** Gumbel plot for all wave directions.



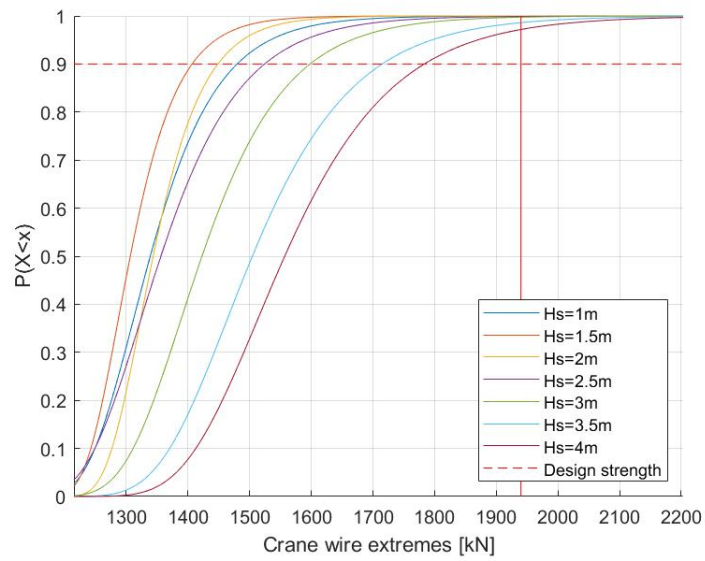
**Figure B.3:** Gumbel plot for all wave directions.

Figure B.4 to B.6 shows CDF for each category of peak periods. All wave directions plotted together.





**Figure B.4:** CDF for all  $H_s$  and wave directions with P5 peak periods.



**Figure B.5:** CDF for all  $H_s$  and wave directions with P95 peak periods.

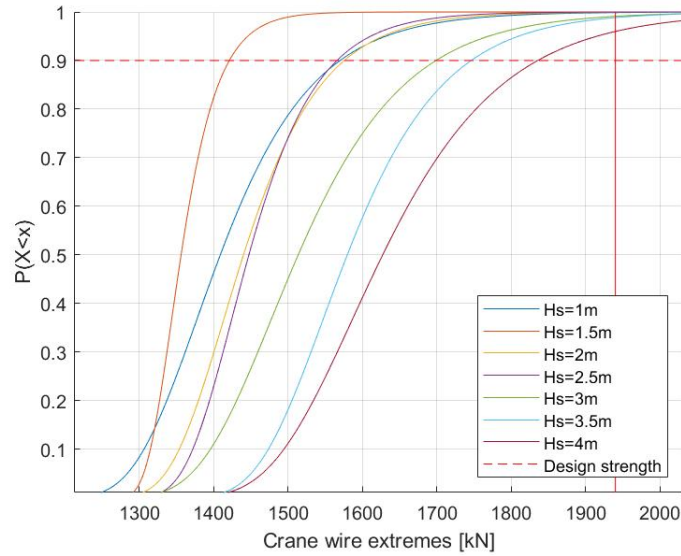


**Figure B.6:** CDF for all  $H_s$  and wave directions with mean peak periods.

## B.1 DPA Characteristic values

**Table B.1:** Most probable maxima and 90% fractile P90 from extreme maxima distributions for all wave directions for crane wire tension DPA model.

$H_s$ [m]	180°		160°		135°	
	$\mu$ [kN]	P90 [kN]	$\mu$ [kN]	P90 [kN]	$\mu$ [kN]	P90 [kN]
4	1238	1278	1250	1284	1269	1342
5	1239	1362	1261	1335	1276	1362
6	1272	1408	1282	1403	1365	1499

## B.2 MATLAB plot

```

% Gumbel distribution calculations

% OK Computer:

x = fopen('CraneWire_Extreme_sample.txt');
x =sort(x);
fclose(values)

E_max_CW = mean(x);
sigma = std(x) ;
% ----- MAXIMA -----
%--- Gumbel Parameters ---
beta = sigma *sqrt(6)/pi %----- Scale parameter
mu = E_max_CW -0.57722*beta % -- Location parameter
z = (x-mu1)/beta;

```

```

% ----- CDF Plotter -----
cdf_gumbel = exp(-exp(-(z)));
plot(x,cdf_gumbel, '-.')
hold on

% ----- PDF Plotter -----
pdf_gumbel = (1/beta)*exp(-(z+exp(-z)));
plot(x, pdf_gumbel, '-')
hold on

% ----- Gumbel Plot for maximum
z = (x-mu)/beta;
n = length(x);
k = [1:n];
plot(x, z, '-')
E = (k) / (n+1);
Empirical_dist = -log(-log(E));
y = real(Empirical_dist).';
plot(x, y, 'o')
hold on
p = polyfit(x,y,1)
f = polyval(p,x) ;
plot(x,f,'--')
hold on

% ---- MINIMA ----
beta = sigma *sqrt(6)/pi ; %----- Scale parameter
mu = E_max_CW + 0.57722*beta % -- Location parameter
z = (x-mu)/beta;
% ----- CDF Plotter -----
cdf_gumbel = 1-exp(-exp((z)));
plot(x,cdf_gumbel, '-')
pdf_gumbel = (1/beta)*exp((z-exp(z)));

```

```

% Plotting hindcast data 1957-2019

values = fopen('Forecast_data.txt');
x = textscan(values,'%f %f %f' , 'headerlines', 0)
fclose(values)

x= x{1}; % Hs values
y = x{2}; % Tp values

[p,S, mu] = polyfit(x,y,1);
[y_fit,delta] = polyval(p,x,S, mu);

plot(x,y, '.')
grid on

```

---

```
hold on
plot(x,y_fit,'-')
plot(x,y_fit+2*delta,'-',x,(y_fit+(1-2*delta)),'-')

legend('Location','southeast','Data','Mean fit','P95 ','P5')
xlim([0 12])
ylim([3 23])

title('Hs and Tp (Tampen 1957-2019)')
xlabel('Hs [m]')
ylabel('Tp [s]')
```

